Universidade Federal do Rio Grande do Sul

Gustavo Zottis Girotto

Improving the photodegradation of dyes with $SrTiO_3$-modified nanoparticles

Porto Alegre, RS, Brazil

2021

Gustavo Zottis Girotto

Aprimoramento da fotodegradação de corantes com nanopartículas de $SrTiO_3$ modificadas

Dissertação realizada sob a orientação do Prof. Dr. Fabiano Bernardi e apresentada para o Programa de Pós-Graduação em Física da Universidade Federal do Rio Grande do Sul, em cumprimento parcial dos requisitos para a obtenção do título de Mestre em Física.

Universidade Federal do Rio Grande do Sul - UFRGS

Instituto de Física

Porto Alegre, RS, Brasil

2021

Agradecimentos

Ao meu estimado orientador, Professor Fabiano, por todo o conhecimento que me transferiu e oportunidades que me proporcionou.

À minha amiga e querida Julia, por acompanhar de perto todo o processo e me fornecer um suporte incondicional.

À minha família, principalmente minha mãe, por me dar a oportunidade de chegar até esse ponto e me fornecer motivação para continuar.

Aos amigos que conheci no IF, aos colegas do Laboratório de Física de Nanoestruturas.

À Professora Fernanda pela concessão do laboratório e auxílio na realização dos experimentos.

Ao CNANO, pela disponibilização do equipamento para realização das medidas de SAXS e XRD. Ao Laboratório de Implantação Iônica pelo tempo de feixe. Ao CMM pelas medidas de microscopia.

Esta pesquisa utilizou instalações do Laboratório Nacional de Luz Síncrotron (LNLS), do Centro Nacional de Pesquisa em Energia e Materiais (CNPEM), uma Organização Social supervisionada pelo Ministério da Ciência, Tecnologia e Inovações (MCTI). As equipes das linha de luz XAFS2, DXAS e SXS são reconhecidas pela assistência durante os experimentos.

Esta pesquisa foi desenvolvida com o apoio do Centro Nacional de Supercomputação (CESUP), Universidade Federal do Rio Grande do Sul (UFRGS).

Ao CNPq, pelo fornecimento da minha bolsa de mestrado com número de processo 139717/2019-6 que permitiu realizar esta pesquisa. Sobretudo, a cada pesquisador brasileiro que batalha e resiste contra os cortes realizados à produção científica no nosso país.

Resumo para público leigo

Corantes são substâncias usadas pela indústria têxtil para o tingimento de produtos e, muitas vezes, chegam aos mananciais, causando diversos problemas ambientais. Bangladesh e China, dois países entre os maiores utilizadores de corantes, continuamente sofrem pelo despejo indevido dessas substâncias. Buscar formas de evitar a presença destes poluentes no meio ambiente é importante para prevenir a contaminação de toda a cadeia alimentar. Uma das formas de reduzir um poluente é degradando-o, ou seja, quebrando-o em partes menores, menos perigosas, com auxílio de materiais específicos que chamamos de catalisadores. Entender o que torna um catalisador mais eficiente é peça-chave para propor processos de degradação de poluentes que sejam economicamente viáveis e ecologicamente mais amigáveis. Um corante bastante preocupante para o meio ambiente é o azul de metileno, por ser muito empregado na indústria. Neste trabalho de pesquisa de mestrado, foi proposto compreender o que torna um catalisador específico mais eficiente no processo de degradação de azul de metileno. O catalisador utilizado faz parte de uma classe especial de materiais denominada nanopartículas, cujo tamanho é muito menor que aquele de materiais convencionais. Em termos de comparação, o tamanho de uma nanopartícula está para o tamanho de uma bola de futebol assim como o tamanho de uma bola de futebol está para o planeta Terra. Foram utilizadas nanopartículas de um mineral conhecido como titanato de estrôncio, barato do ponto de vista comercial e promissor para essa reação. Essas nanopartículas, ao absorverem a luz do sol, tornam-se capazes de degradar o azul de metileno. Essa reação de degradação do azul de metileno catalisada pelas nanopartículas expostas à luz pode ser observada na figura abaixo.

Exemplo de reação de fotodegradação do azul de metileno.

As nanopartículas sofreram dois tipos de tratamento que permitiram investigar suas propriedades: primeiramente, foram incorporadas a elas nanopartículas de níquel, outro material barato, as quais foram previamente aquecidas em diferentes temperaturas. As nanopartícu-

las de titanato de estrôncio combinadas com as nanopartículas de níquel previamente aquecidas degradaram eficientemente o azul de metileno. O aquecimento mudou a composição das nanopartículas de níquel que foram fundamentais para causar a degradação do corante. Quando as nanopartículas de níquel estão oxidadas na forma de óxido de níquel, existe uma doação de elétrons das nanopartículas de níquel para as nanopartículas de titanato de estrôncio, que viabiliza a degradação do azul de metileno. Por outro lado, quando as nanopartículas de níquel estão no estado metálico, induzem uma modificação na estrutura da superfície das nanopartículas de titanato de estrôncio, que também contribui para a degradação do azul de metileno. Em uma segunda abordagem, dessa vez com nanopartículas de titanato de estrôncio sem adição de níquel, foram criados defeitos atômicos através do bombardeamento de íons de ouro. Os defeitos atômicos são mudanças nas posições dos átomos existentes nas nanopartículas de titanato de estrôncio e íons de ouro energéticos permitem uma enorme criação de defeitos no titanato de estrôncio. Esse tratamento resultou em uma degradação do azul de metileno ainda mais eficiente que aquela causada pelas nanopartículas tratadas conforme a abordagem anterior. Isso provoca uma maior interação do azul de metileno com as nanopartículas de titanato de estrôncio, melhorando a eficiência de degradação. Dessa forma, o presente trabalho apresentou formas alternativas para a melhora da eficiência de materias utilizados na degradação do azul de metileno, contribuindo para a diminuição de efeitos indesejados no meio ambiente.

Abstract

Nowadays, thousands of tons of dyes are produced worldwide annually by the industry, and almost one-third of these substances is thrown into effluents. Methylene blue is a widely used dye. Thus, there is a strong need to efficiently remove this pollutant from the aquatic environment. Also, the degradation of this molecule can be used as a model system to understand the degradation of even more complex and toxic molecules. An interesting idea is the use of the Sun's energy which arrives at Earth's surface to induce the photodegradation of methylene blue by using photocatalysts. This work aims to propose alternatives for the improvement of the photodegradation of methylene blue and to elucidate the atomic mechanisms existing in these reactions. For that, two different systems based on the modification of commercial $SrTiO_3$ nanoparticles were used. In the first part of the work, $SrTiO_3$ and Ni nanoparticles (synthesized from $NiCl_2.6H_2O$ precursor) were characterized by X-Ray Diffraction (XRD), Small-Angle X-Ray Scattering (SAXS) and Transmission Electron Microscopy (TEM), obtaining a mean size of 35 nm ($SrTiO_3$), and 3 nm (Ni). Then the Ni nanoparticles were exposed to a thermal treatment in ambient atmosphere at 100 ºC, 300 ºC and 500 ºC. In situ time-resolved X-Ray Absorption Near-Edge Structure (XANES) and in situ Extended X-Ray Absorption Fine Structure (EXAFS) techniques were measured at the Ni K edge during the heating treatments. The analysis shows that the thermal treatment allows tuning the chemical components of Ni nanoparticles (Ni^0 and NiO amount). Afterward, 5 wt.$\%$ of the Ni nanoparticles were supported on $SrTiO_3$ nanoparticles and used in the photodegradation reaction of methylene blue. Samples heated at 300 ºC and 500 ºC showed an improved activity compared to the sample without thermal treatment. X-Ray Photoelectron Spectroscopy (XPS) measurements at the Ni $2p_{3/2}$ region show the major component at the surface is $Ni(OH)_2$ for samples heated up to 300 ºC but NiO appears as the main chemical component for the sample heated at 500 ºC. The XPS measurements at the Ti $2p_{3/2}$, Sr 3d and O 1s electronic regions enabled detecting new surface components after the reaction, which are indicative of surface reconstruction of $SrTiO_3$ into TiO_x and SrO_x terminated surfaces. Density Functional Theory (DFT) results also indicate that the inclusion of Ni induces a change on the electronic density at the p orbitals of Sr and O, which is in agreement with the XPS results. The reason for the improvement in the photodegradation due to the inclusion of Ni nanoparticles treated at 300 ºC is related to the optimization of the metallic Ni amount. Nonetheless, the Ni nanoparticles treated at 500 ºC present a high amount of NiO, possibly forming a $NiO/SrTiO_3$ heterostructure that prevents the electron-hole pair recombination. In the second part of the work,

the $SrTiO_3$ nanoparticles were submitted to different fluences of Au^{7+} ion irradiation in order to create atomic vacancies. The irradiation was carried out in three different fluences: 1×10^{13} ions/cm^2, 5×10^{13} ions/cm^2 and 1×10^{14} ions/cm^2. All three samples show improved efficiency on the degradation of methylene blue, even if compared to the best Ni/$SrTiO_3$ system. XRD and UV-Vis measurements show that the $SrTiO_3$ nanoparticles do not suffer noticeable structural and electronic changes upon irradiation and before the photoreaction. XPS measurements at the Sr 3d and Ti $2p_{3/2}$ electronic regions were able to detect new surface components after the photoreaction, which may appear due to the vacancy diffusion to the surface region. The improvement in the photodegradation results is related to these extra adsorption sites at the surface.

Keywords: in situ time-resolved XANES, in situ XAS, XPS, methylene blue, photocatalysis, DFT

Resumo

Anualmente, milhares de toneladas de corantes são produzidas pela indústria e aproximadamente um terço dessas substâncias são descartadas nos efluentes. O azul de metileno é um corante amplamente utilizado e, portanto, há uma grande necessidade de removê-lo do meio aquático. Além disso, o estudo da degradação dessa molécula serve como um sistema modelo para entender a degradação de moléculas tóxicas mais complexas. Uma ideia interessante consiste em utilizar a energia solar irradiada sobre a supefície terreste para induzir a degração do azul de metileno por meio de fotocatalisadores. Este trabalho tem como objetivo propor alternativas para o aperfeiçoamento da fotodegradação do azul de metileno e elucidar os mecanismos atômicos da reação. Para isso, foram empregados dois sistemas distintos baseados na modificação de nanopartículas de $SrTiO_3$ comercial. Na primeira parte do projeto, nanopartículas de $SrTiO_3$ e Ni (sintetizadas a partir de um precursor de $NiCl_2.6H_2O$) foram caracterizadas por Difração de Raios X (XRD), Espalhamento de Raios X a Baixos Ângulos (SAXS) e Microscopia Eletrônica de Transmissão (TEM), que permitiram obter tamanhos de aproximadamente 35 nm ($SrTiO_3$) e 3 nm (Ni). As nanopartículas de Ni foram expostas a um tratamento térmico em atmosfera ambiente a 100 ºC, 300 ºC e 500 ºC. Medidas de Estrutura de Absorção de Raios X Próxima à Borda (XANES) *in situ* resolvida no tempo e de Estrutura Fina Estendida de Absorção de Raios X (EXAFS) *in situ* foram realizadas na borda K do Ni durante o tratamento térmico. A análise mostra que o tratamento térmico permite regular as componentes químicas das nanopartículas de Ni^0 para NiO. Posteriormente, 5 % em massa de Ni foi suportado sobre o $SrTiO_3$ e utilizado na reação de fotodegradação do azul de metileno. As amostras aquecidas a 300 ºC e 500 ºC apresentaram uma melhora na atividade comparadas com a amostra sem tratamento térmico. Medidas de Espectroscopia de Fotoelétrons Excitados por Raios X (XPS) na região do Ni $2p_{3/2}$ exibiram uma fase majoritária de $Ni(OH)_2$ para as amostras tratadas até 300 ºC, enquanto que na amostra tratada a 500 ºC a fase majoritária é de NiO. As medidas de XPS nas regiões O 1s, Ti $2p_{3/2}$ e Sr 3d permitiram a detecção de novas componentes depois da reação que indicam uma reconstrução da superfície de $SrTiO_3$ em TiO_{2-x} e SrO_x. Cálculos da Teoria do Funcional da Densidade (DFT) indicam que a inclusão de Ni na superfície do $SrTiO_3$ modificam a densidade de cargas nos orbitais p do O e Sr, e essa mudança pode estar relacionada com uma componente identificada no XPS. A razão do aumento da eficiência de fotodegradação para as nanopartículas de Ni tratadas a 300 ºC está relacionada a otimização da fração de Ni metálico, enquanto que para as nanopartículas de Ni tratadas a 500 ºC está relacionada possivelmente à formação de

uma heterojunção NiO/$SrTiO_3$. Na segunda parte do trabalho, as nanopartículas de $SrTiO_3$ foram submetidas a diferentes fluências de íons Au^{7+}, 1×10^{13} ions/cm^2, 5×10^{13} ions/cm^2 e 1×10^{14} íons/cm^2, a fim de gerar vacâncias de O. As três amostras apresentaram um aumento na eficiência da degradação do azul de metileno, até mesmo se comparadas à melhor amostra de Ni/$SrTiO_3$. Medidas de XRD e espectroscopia UV-Visível permitiram observar que a estrutura do $SrTiO_3$ não sofre nenhuma mudança estrutural ou eletrônica aparente após a irradiação e antes da fotorreação. No entanto, medidas de XPS nas regiões eletrônicas do Sr 3d e Ti $2p_{3/2}$ detectaram novas componentes na superfície após a reação, provavelmente devido à difusão de vacâncias para a superfície do $SrTiO_3$. O aumento da eficiência da fotodegradação, nesse caso, está relacionado ao aumento dos sítios na superfície do $SrTiO_3$ que permitem a adsorção das moléculas na solução.

Palavras-chave: XANES in situ resolvido no tempo, XAS in situ, XPS, azul de metileno, fotocatálise, DFT

List of Figures

List of Tables

List of abbreviations and acronyms

AOPs	Advanced Oxidation Processes
LUMO	Lowest unoccupied molecular orbital
HOMO	Highest occuppied molecular orbital
CBE	Conduction-Band Edge
VBE	Valence-Band Edge
NHE	Normal Hydrogen Electrode
XRD	X-ray Diffraction
SAXS	Small-Angle X-ray Scattering
TEM	Transmission Electron Microscopy
UV-Vis	Ultraviolet-Visible Spectroscopy
BET	Brunauer-Emmett-Teller Theory
XAS	X-ray Absorption Spectroscopy
EXAFS	Extend X-ray Absorption Fine Structure
XANES	X-ray Absorption Near-Edge Strucuture
LCA	Linear Combination Analysis
XPS	X-ray Photoelectron Spectroscopy
DFT	Density Functional Theory
LDA	Local Density Approximation
GGA	Gradient Density Approximation
DOS	Density of States
SRIM	Stopping and Range of Ions in Matter

List of symbols

k	rate of reaction
k_0	reaction's pre-exponential factor
E_a	activation energy of reaction
T	temperature
τ	average residence time of adsorption
τ_0	period of vibration of the surface at the vibration site
ΔH	heat of reaction
R	gas constant
E_{VB}	valence band energy level
E_{CB}	conduction band energy level
λ	X-ray wavelength
$\mathbf{S}$	Poyinting vector
$\mathbf{E}$	Electric field vector
$\mathbf{B}$	Magnetic induction field vector
$\mathbf{A}$	Magnetic vector potential
ϕ	Electric potential
μ_0	vacuum permeability
c	speed of light in vacuum
e	elementary electric charge
t_r	retarded time
t	time

$\mathbf{r}$	position vector
γ	Lorentz factor
P	total power
$\Delta\theta$	angle interval
d	distance between lattice planes
$\mathbf{k}$	reciprocal space vector
B	full-width at half maximum
R_{exp}	expected profile agreement factor
R_{wp}	weighted profile agreement factor
χ^2	chi-squared factor
q	scattering vector
λ_e	de Broglie wavelength
m_e	electron mass
E_0	energy of accelerated electrons
I	transmitted light intensity
I_0	incident light intensity
$\mu(E)$	absorption coefficient
x	optical path
A	absorbance
R_∞	reflectance
ν	frequency of light
E_g	band-gap energy value
$\hat{H}$	Hamiltonian operator

$\hat{\mathbf{p}}$	linear momentum operator
E_f	final state energy
E_i	initial state energy
M_{fi}	transition operator between initial and final state
W_{fi}	transition rate between initial and final state
$\hbar$	reduced Planck's constant
σ_{nl}	differential cross section of the nl atomic level
I_{nl}	total intensity of emission from the nl atomic level
K	kinetic energy of free electron
E_b	binding energy of the electron with respect to the Fermi level
φ_w	sample work-function
φ_a	analyzer work-function
Γ	lifetime broadening parameter
σ_a	absorption cross-section
ω	angular frequency of light
$\hat{V}_{int}$	interstitial potential
$\hat{V}$	electron scattering perturbation
$\hat{G}$	scattering propagator
$\hat{G}^0$	free-electron propagator
E_f	energy of the Fermi level
E_b	binding energy of the electron in the ground state of the system
N_j	coordination number of the j-th atomic shell
σ_j	Debye-Waller factor of the j-th atomic shell

$S(E)$	stopping power of ionic collision
Z_A	atomic number of A-th nuclei
M_i	atomic mass of i-th nuclei
$\rho(\mathbf{r})$	electron density
T	kinetic energy functional
$E_{e,e}$	electron-electron energy functional
$E_{e,N}$	electron-nuclei energy functional
V_{ext}	external atomic potential
E_{xc}	enchange-correlation energy functional
U	Hubbard parameter

Contents

Introduction

Currently, water pollution is a major issue induced by humankind's progress, and an efficient method to remove the aquatic pollutants is needed. At the beginning of the last decade, Vörösmarty et al [1] investigated water pollution and estimated that $80\ \%$ of the global population is exposed to high levels of a threat factor. About 7×10^8 kg of synthetic dyes are annually produced in the textile industry, in which 15% [2] of these are lost to the effluent during the industrial processes. Dyes can have a serious effect on the aquatic biota due to their potential to produce toxic intermediates and, by absorbing light from the Sun, to decrease the photosynthesis efficiency of underwater plants. Methylene blue ($C_{16}H_{18}N_3SCl$) is a multi-purpose synthetic dye. It is a green powder that, when dissolved in water, turns into a blue solution due to its oxidation. Even with its application in tissue staining and medical fields such as methemoglobinemia treatment or urinary tract infections, several studies on the literature have shown that high doses of methylene blue cause multiple side effects, ranging from hemolysis to serotonin syndrome [3, 4]. It especially represents high toxicity to neonates, possibly inducing life-threatening conditions [5].

Many methods can be encountered nowadays in the literature aiming to treat the effluent of the industries. A photodegradation reaction that occurs through the use of catalysts can be designed. Thus, methylene blue breaks down into less toxic or completely mineralized products. A photocatalyst, which is a substance that promotes the reaction, receives the activation energy for the reaction from a light source. For this goal, the solar energy that reaches Earth's surface can be harnessed. As shown in Figure 1, Brazil receives around 200 W/m^2 from the Sun over the year, implying a great prospect in using this type of green energy. However, multiple obstacles to the discovery of excellent photocatalysts exist. The catalysts are usually semiconductors that do not allow the absorption of visible light. Since the UV part of the solar spectrum at Earth's surface (illustrated in Figure 2) is only about $5\ \%$ of the total intensity, the high band-gap value results in a huge waste of energy as the catalyst cannot absorb the major part of the spectrum. Photocatalysts depend as well on other characteristics such as favorable conduction band and valence band edge positions, photo-corrosion resistivity and a suitable structure for charge transfer [6]. Moreover, because catalysis is an interface phenomenon, bulk photo-generated electrons must travel to the surface of the catalyst, and electron-hole charge recombination may decrease the efficiency of

the reaction.

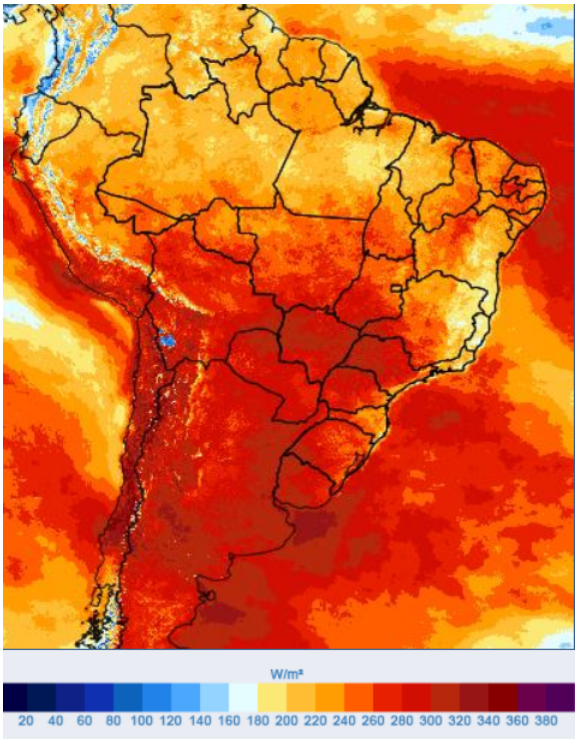

Figure 1 – Average global solar irradiance in November 2020 in Brazil. Image taken from Instituto Nacional de Pesquisas Espaciais [7].

Advanced catalysts are typically composed of nanoparticles since they have a characteristic high surface area per mass, which can be exploited for surface reactions. The support of one nanoparticle on a metal oxide is an effective method to avoid sintering effects (that decrease the high surface area of the system). One of the most employed strategies used to improve the efficiency of the photocatalytic process is the band-gap engineering of the nanoparticles. Doping the material structure with certain atomic species creates an impurity level between valence and conduction bands, resulting in narrowing the optical gap. The research is also focused on the reduction in charge recombination. Therefore, promoting a higher charge density at the catalyst surface and increasing the reaction efficiency [6]. Some researchers explore the generation of O vacancies that act as the photoinduced charge traps and adsorption sites for the organic molecules and influence the creation of defect-defect interactions, which promote intermediate states inside the gap similarly to impurity levels [8, 9]. Aside from the intrinsic need for efficient catalysts, the study of the atomic events during dye degradation reaction is essential for designing future improved photocatalysts.

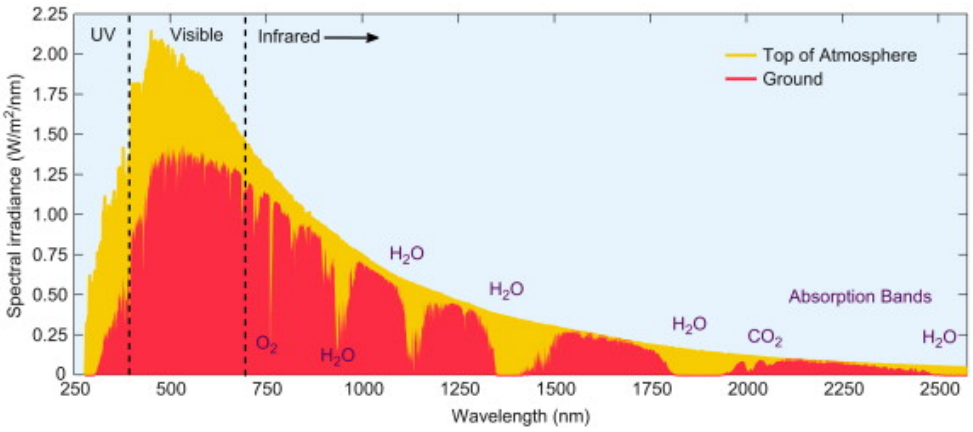

Figure 2 – Illustration of the solar spectrum at sea level after absorption and scattering of light by different molecules. The absorption and scattering spectral regions by molecules such as H_2O and CO_2 are indicated. Adapted from [10].

This work presents the study of $SrTiO_3$-based photocatalysts in the degradation of methylene blue, under the goal of finding efficient ways of photodegradating dyes, besides shedding light on the reaction mechanisms involved. These results will open new perspectives for the future projection of smart photocatalysts for water treatment. The first chapter elaborates on the fundamentals of catalysis and a literature review. The second chapter expands on the principles of the physical methods and techniques used throughout the research. These methods include X-Ray Diffraction, Small-Angle X-Ray Scattering, Transmission Electron Microscopy, X-Ray Photoelectron Spectroscopy, X-Ray Absorption Spectroscopy, Ion Irradiation and Density Functional Theory. The third chapter focus on the experimental procedures and methodology. The fourth and fifth chapters finish with a discussion and conclusions of the results obtained, respectively.

1 Advanced photocatalysis strategies applied to dye degradation reactions

An introduction to the use of nanoparticles in catalytic processes is presented in this chapter. Also, the reader is guided into a brief literature review in order to comprehend the basics and some state-of-the-art studies involving the use of photocatalysts for the degradation of dyes.

1.1 Nanoparticles for heterogeneous catalysis

Catalysis can be defined as a chemical reaction that includes a material or substance which induces an alternative reactional energetic path with smaller activation energy, thus increasing the speed of the chemical process or even enabling a process to occur in milder conditions [11, 12]. Additionally, the catalyst must be recovered after the reaction, it is not consumed along with the reagents. There are three main classes of catalysts: homogeneous catalysts, heterogeneous catalysts and biocatalysts (enzymes, for instance). Heterogeneous catalysis is the process that occurs with different physical phases of catalyst and reagents, where the most common is a solid-liquid or solid-gas reaction. The main advantage of heterogeneous catalysis, in comparison to the homogeneous one, is the ease of separating the catalyst and products (since there are different phases) at the end of the reaction. In the case of solid catalysts, the material surface dictates the reaction mechanisms, providing sites for the elementary reaction steps [13].

The choice of a catalyst for practical applications must be defined by different factors [12]. The reaction rate plays a major role in catalysis and can be usually described by Arrhenius's equation in the atomic-scale representation:

$$k = k_0 e^{-E_a/k_B T} \tag{1.1}$$

where k is the reaction rate, k_0 is a prefactor that can be approximated, for example, through Transition State Theory [12], E_a is the activation energy, T is the temperature and k_B is the Boltzmann's constant. Selectivity defines the rate at which a catalyst supports the formation of one product over others. For example, the H_2 and CO_2 reactants can form multiple different products such as CO, hydrocarbons, CH_4 or alcohols [12]. The cost-effectiveness must be considered,

since nowadays the search for environmentally friendly sources is of pivotal importance, as well the lower prices for industrial application and the abundance of the specific elements composing the catalyst.

Considering solid catalysts in heterogeneous catalysis, the first step of a catalytic reaction is the adsorption of the reagents molecules at the catalyst surface [13]. Adsorption can be defined in two major categories: physisorption, where the molecules interact with the surface of the catalyst due to the van der Waals forces between electrical molecular multipoles, or by chemisorption, in which a chemical ionic or covalent bond is formed between both substances [13]. After adsorption, many different elementary reaction steps may take place, such as surface diffusion of the molecules in adjacent sites due to thermal effects, chemical structure rearrangement by the dissociation and formation of new chemical bonds, recombination, and finally the desorption of the newly formed products from the surface. The average time that a molecule stays adsorbed in the surface, τ, can be estimated by [13]:

$$\tau = \tau_0 e^{\frac{-|\Delta H|}{RT}} \tag{1.2}$$

The parameter τ_0 is correlated to the vibrational frequency of the catalyst surface atoms. ΔH represents the exothermic adsorption enthalpy, also called the adsorption strength. R is the ideal gas constant.

Nanoparticles are diversely applied as heterogeneous catalysts and they have been used by humankind for centuries, even before the scientific community discovered the potential of these materials. Au nanoparticles were used millennia ago for art and even medicinal situations in China and Egypt [14]. The nanoparticles have a size in the order of nanometers (10^{-9} m). Aside from nanoparticles, multiple nanometric structures exist as well, such as nanorods, nanoribbons, thin films, quantum dots and many others. Heterogeneous catalysts may be composed of organic structures, organometallics, metal oxides, sulfides and nitrides, metallic, bimetallic, trimetallic and high entropy alloys. This huge diversity of substances allows for the selection of optimal catalysts for each type of reaction.

Nanoparticles present quantum confinement effects for sizes around the de Broglie wavelength of the electrons [15]. For example, titania nanoparticles of less than 10 nm display a considerable enhancement in the catalytic activity for hydrogen evolution and the hydrogenation of alkenes reactions [16]. The confinement affects the mobility of charge carriers, leading to the enhancement of the performance relative to microsized TiO_2. Colloidal nanocrystal

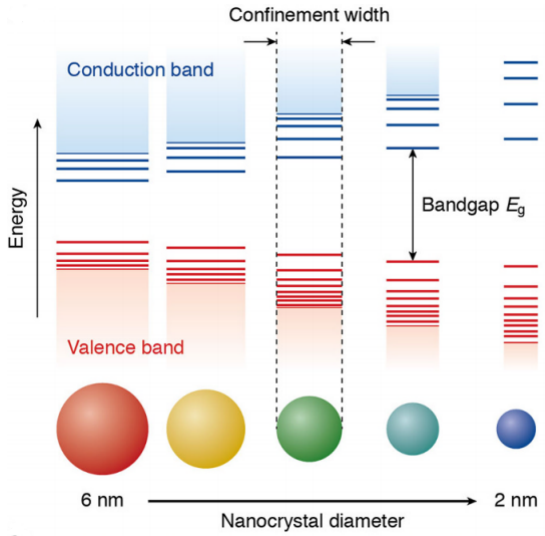

Figure 3 – Representation of different colloidal nanocrystal sizes and their respective energy levels. The color of the nanoparticles is related to their band gap, where a narrow band gap allows the particles to be excited by higher wavelengths of light. Adapted from [15].

semiconductors are well known for presenting quantum confinement effects in which the color is directly related to the nanoparticle size [15]. This is represented in Figure 3, where the confinement induces a discretization of the energy levels relative to bulk materials.

A catalyst can be constituted by a nanoparticle supported on the surface of a bigger size material (support). A support grants several advantages. Its surface allows adsorption sites for the molecules, besides stabilizing the supported particles and avoiding agglomeration effects. Some supports can even take part in electron transfer mechanisms, such as redox reactions.

1.2 Photocatalysis and dye degradation mechanisms

Nowadays, effluent treatment represents one of the most explored research topics. Usually, the wastewater discharged from textile, cosmetic and paper factories presents a mixture of dyes, metals and multiple trace pollutants [17]. The wastewater characteristics are usually evaluated by the pH of the effluent, the total carbon content, the chemical and biochemical oxygen demand, salts, ammonia, phenol, chlorides, sulfides and metals content. Brazil's textile industry is one of the major sectors in the national economy, where approximately 26 thousand tons of dyes are consumed annually [18]. Effluent treatment methods like adsorption and coagulation [19] are largely used, although they only transform from the liquid to the solid phase, then producing secondary pollution. Dyes can be categorized into cationic or anionic types. Methylene blue, for

example, is a cationic dye, also called a basic dye. Activated carbon, one of the most employed materials for effluent treatment, presents limited adsorption of cationic dyes due to its surface presenting a positive character.

It is possible to use catalysts for dye degradation reactions, and there are different methods applied to achieve the activation energy of these processes. Most industrial applications typically obtain the activation energy by reaching a thermodynamic state, i.e., temperature and pressure values that are adequate for the reaction. Alternatively, a photocatalyst can obtain its activation energy by the absorption of photons. Thus, the reaction conditions are milder than traditional catalytic reactions (high pressure and temperature). Since Fujishima and Honda published about the possibility of using TiO_2 as a photocatalyst in 1972 for the water-splitting reaction [20], the number of publications in the field has grown exponentially. The cleanest energy source that humanity can potentially harvest is the solar light. Around 4×10^{24} J of solar energy reaches the Earth annually, but only 5×10^{22} J are used [21]. Nowadays, the use of photovoltaic or solar thermal technologies is a cutting edge topic in renewable energy.

The use of photocatalysis in dye degradation processes is part of the greater field of Advanced Oxidation Processes (AOPs), which is one of the best-known methods for effluent treatment [22]. Photocatalytic reactions have an advantage over simple photolysis because the organic pollutants are completely mineralized to non-toxic substances such as CO_2 and H_2O, without the generation of toxic intermediate products. Some other examples of AOPs are wastewater treatment with O_3, H_2O_2, electron beams and Fenton's reaction [22]. The photocatalysts can be supported over multiple substrates for industrial applications such as glasses, fibers, stainless steel and activated carbon. The main issue of using single photocatalysts is the lack of selectivity towards the desirable products. The discovery of selective heterogeneous photocatalysts for fine chemicals is currently pursued by green chemistry studies [23].

Semiconductors are widely used in photocatalysis due to their possibility of absorbing light in selected frequencies, promoting the excitation of charge carriers that participate in catalytic reactions. Figure 4 represents an electronic energy level diagram for a semiconductor. A semiconductor in the ground state has the highest occupied energy level at the top of the valence band (E_{VB}) while the lowest unoccupied energy level is at the bottom of the conduction band (E_{CB}). These two electronic levels are separated by the energy band gap. The Fermi level is located (E_F) inside the energy band gap. The vacuum level determines the zero energy level for the electrons, where they are not bound anymore to the material. The electrochemical

potential gives the electron binding energy. The electrostatic potential is defined as the energy needed to move an electron from a reference point (infinity, for example) to the surface of the semiconductor. The work function is defined as the difference between the binding energy and the electrostatic potential, thus representing the work needed to remove an electron from the solid. Additionally, the electron affinity is the difference between the electrostatic potential and E_{CB}, and it is used for determining the band bending at the interface of two different materials [24]. Due to the band gap in the electronic structure, a photon can excite electrons from the valence band of the semiconductor to its conduction band, leaving a hole in the former. Usually, the band gap of the semiconductors presents values between 1 eV and 5 eV, allowing absorption of light from UV to the visible region of the electromagnetic spectrum, although the majority of catalytic materials does not absorb in the visible region. The electron-hole pair can travel through the material and participate in the redox reactions at the surface. Usually, the lifetime of a charge-carrier pair is of the order of nanoseconds, which is enough for the electron-hole pair to reach the material's surface.

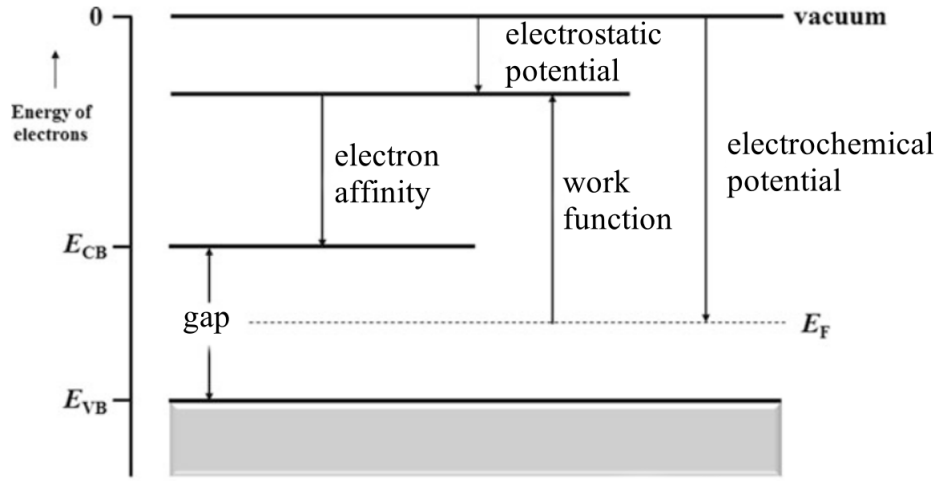

Figure 4 – Representation of a semiconductor energy levels in a chemical solution. Adapted from [24].

An efficient semiconductor needs proper energy levels to participate in the photocatalytic reaction. The bottom of the conduction band determines the reducing potential of photoelectrons while the top of the valence band determines the oxidation potential of the holes. Figure 5 represents the valence and conduction band positions for different materials that are used in photocatalysis, relative to the Normal Hydrogen Electrode (NHE). The NHE is the potential of a Pt electrode immersed into a 1 M strong acid solution with hydrogen gas at 1 atm pressure. The hydrogen electrode considers the respective half cell reaction of $2\mathrm{H}^+(\mathrm{aq}) + 2e^- \rightarrow \mathrm{H}_2(\mathrm{g})$.

Water-splitting reactions for H_2 production can be executed with a catalyst that has its valence band below the redox potential of the oxygen evolution reaction (O_2/H_2O) and a conduction band above the redox potential of the hydrogen evolution reaction (H_2O/H_2). Similarly, dye degradation reactions need proper band edge alignments as well.

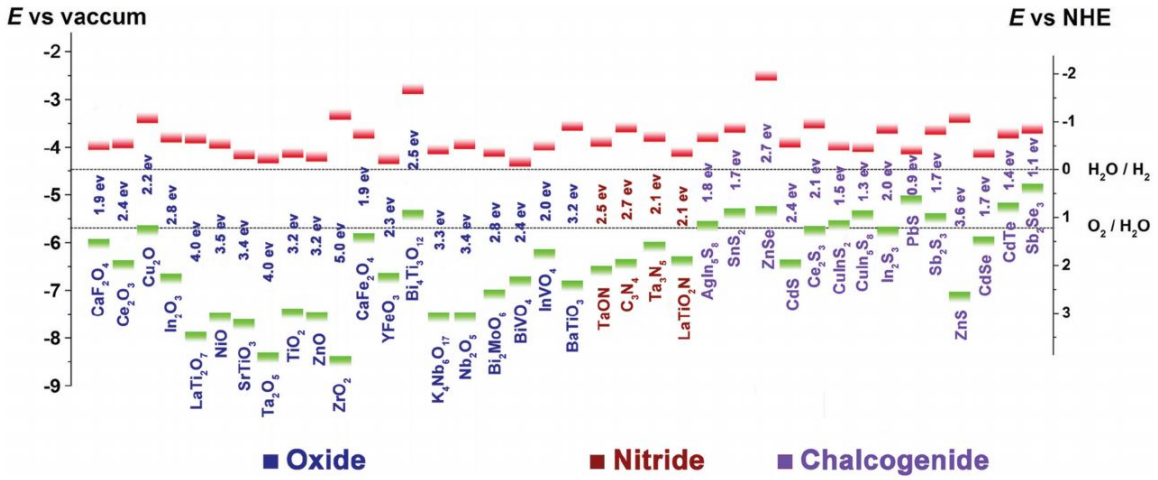

Figure 5 – Band edge positions for different semiconductors concerning the vacuum level and NHE. The horizontal red and green lines represent E_{CB} and E_{VB}, respectively. The two dashed lines indicate the water redox reaction potentials. Adapted from [25].

Figure 6 illustrates a simplistic energy level scheme of a dye degradation process. Density Function Theory calculations of methylene blue [26] have shown that the highest occupied molecular orbital (HOMO) and the lowest unoccupied molecular orbital (LUMO) energy levels are separated by 2.43 eV. The UV-Vis spectrum of methylene blue presents the main light absorption band at around 664 nm. It is used to evaluate the amount of photodegradation by the change of the area of the absorption band. In a first approximation, the photocatalyst would need to have its valence band edge with a potential higher than the HOMO of methylene blue and a conduction band edge with a potential lower than the LUMO for a total reduction and oxidation direct pathway of methylene blue through the transfer of electrons or holes to the photocatalyst. In fact, methylene blue degradation frequently relies on an indirect mechanism [23]. After light absorption, the holes in the catalyst can promote the ionization of water [27]: $H_2O(ads) + h^+ \rightarrow OH\cdot + H^+$. The scavenging of the photogenerated electrons by dissolved O_2 in the water-dye solution creates reactive radicals. For example, the $O_2^-\cdot$ anion can be formed by the reduction of O_2 from the photoexcited electrons. From $O_2^-\cdot$ and H^+, H_2O_2 can be produced. The H_2O_2 can be further transformed into more $OH\cdot$. Therefore, these types of substances can react with the dye due to their elevated redox potentials. In order to understand which mechanism occurs in the reaction of a specific catalyst, certain scavengers (sacrificial agents) can be further added

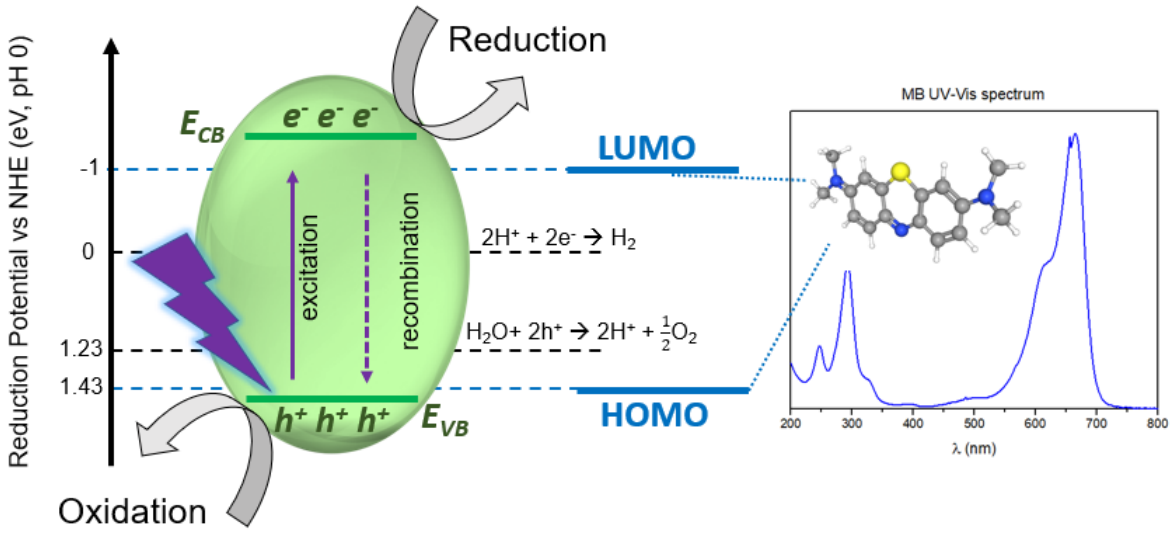

Figure 6 – Reduction potentials against NHE. Band edges of the semiconductor are represented with the electron-hole pairs generated after photon absorption. Common water-splitting half cell reactions and HOMO-LUMO levels of methylene blue calculated by DFT [26] are identified. On the right, the UV-Visible absorption spectrum of methylene blue molecule is shown.

to the solution, where their inclusion results in the decrease of the reaction efficiency whether related to a major pathway of the reaction. A typically used electron scavenger is $AgNO_3$, while methanol can participate as a hole scavenger. Benzoquinone and 2-propanol can act as scavengers for $\cdot O_2^-$ and $\cdot OH$, respectively [28]. Another indirect mechanism is the photosensitization of dye molecules, providing the photocatalyst with additional electrons that are able to generate radicals like $\cdot O_2^-$. Photosensitization process can be used for those semiconductors with a band gap that does not allow the absorption in the region where the dye absorbs light. The incidence of photons excites the organic molecules, which can therefore transfer electrons to the catalyst or the solution. However, the direct photoexcitation of dyes may induce a colorless transition state, where the molecule is photobleached. For instance, methylene blue can turn into the leuco form in an anaerobic medium, but when O_2 is introduced to the solution, it reverts to the oxidized state which corresponds to the blue color [29].

The pH value of the solution strongly affects the photodegradation reaction of methylene blue. When a semiconductor material dissolves into the electrolyte, it absorbs ions or molecules forming an electrical double layer at the surface [30]. The first layer creates a surface charge while the second layer screens the electric field of the first one. Because the surface of the photocatalyst is charged, it creates an electrostatic field that affects the dye molecules in a solution. The second layer loosely bonded to the photocatalyst is also composed of dye molecules that diffuse

through the solution under the influence of electrostatic attraction. This induces a band bending within the semiconductor material which affects the charge carrier migration direction. Thus, changing the flow of electrons and holes through the semiconductor. For basic pH solutions, high adsorption capacity of cationic dyes can be found at the photocatalyst surface, while for acid pH the adsorption of anionic dyes is favored. This type of amphoteric characteristic by the photocatalyst is observed in most metal oxides. The point of zero charge is defined as the pH where the surface's net charge is null. For pH values higher than the point of zero charge of the photocatalyst, its surface becomes negatively charged [31]. The opposite happens if the pH value is lower than the point of zero charge. For the anatase phase of TiO_2, for example, it was observed that an increase in the pH of the solution leads to a higher degradation rate of methylene blue [32]. Other factors influencing the reaction efficiency are the temperature, light intensity and initial dye concentration. For low temperatures, although the adsorption of the dye is more favorable, it is harder to reach the activation energy for its degradation, whereas for high temperatures the adsorption is less probable. For high dye concentration, the absorption of photons decreases, because dyes form multiple adsorption layers in the catalyst surface that absorb or scatter light. Light source intensity usually increases the reaction efficiency, although the maximum generation of electron-hole pairs can limit the optimal amount of photons absorbed.

To tune the absorption band and to extend the absorbing range of light into the visible region, doping of anions or cations in the semiconductors is a common method [30]. The anions, typically nitrogen, carbon or halogens, create electron donor levels near the valence band, while cations are usually transition metal ions that introduce electron accepting levels near the conduction band. However, dopants typically become electron-hole recombination centers, which reduces the reaction efficiency. Considering this, there are alternative methods of narrowing the band gap of semiconductors. In a previous work of the group, it was possible to shift the band gap from UV to the visible region of CeO_2 nanoparticles by synthesizing highly disordered nanoparticles [33].

The inclusion of metallic cocatalysts in the system can create interesting electronic processes at the cocatalyst-semiconductor interface. Typical cocatalysts are metals, such as Pt, Pd, Rh, Au, Ag, Cu and Ni or even another semiconductor. Noble metals like Pt present one of the highest efficiencies in multiple catalytic reactions, but its price and scarcity make large industrial applications difficult. For this reason, more common metals are usually studied aiming to increase their efficiency. The usual energy level alignment of metal nanoparticles

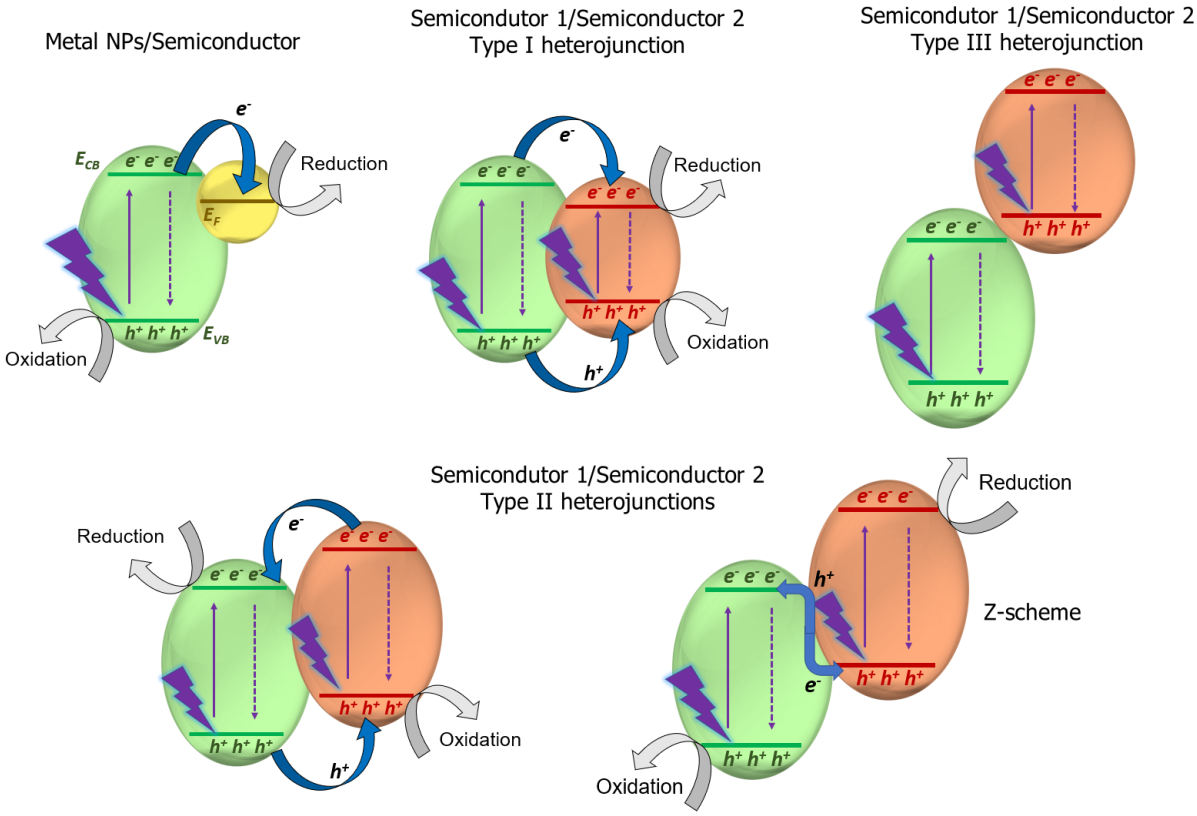

Figure 7 – Different types of cocatalysts energy arrangement. The semiconductors 1 (S1) and 2 (S2) are represented in the green and red ellipses, respectively, and the yellow one represents the metallic phase.

supported over semiconductors can be visualized in Figure 7. The Schottky barrier can appear at the metal–semiconductor interface due to the difference in Fermi levels, generating a built-in electric field that drives the charge flow until the system reaches the equilibrium state [34, 35]. Considering the photoexcitation of the semiconductor and the subsequent creation of electron-hole pairs, the driving force generated by the difference in potential between the conduction band of the semiconductor and the Fermi level of the metal results in a charge transfer to the nanoparticles, decreasing the electron-hole pair recombination. Thus, the holes in the semiconductor can oxidize substances while the metallic nanoparticle can act as a reducing agent.

The use of heterojunctions in photocatalysis is considered one of the most promising approaches to improve the performance of semiconductors due to its effectiveness for the spatial separation of electron–hole pairs [36]. The heterojunction is defined as the interface formed between two semiconductors with unequal band structures, where the band alignment produces synergistic effects. While single component catalysts, such as TiO_2, $SrTiO_3$, ZnO, CeO_2, Fe_2O_3, ZnS, SnO_2, NiO, ZrO_2, CdS, Ta_2O_5 and many others, are extensively studied, the efficiency is

limited to either fast electron-hole pair recombination or UV light absorption.

As represented in Figure 7, there are mainly three types of heterojunctions with semiconductors that can be used in photocatalysis, considering the specific alignment between their energy levels [36, 37]. In a Type I heterojunction, also called a "Straddling gap", the semiconductor 1 (S1) has a higher conduction band edge (CBE) than the semiconductor 2 (S2), which allows the electron transfer from the former to the later. Similarly, because of the lower valence band edge (VBE) of S1, its photogenerated holes can be transferred to S2. This configuration allows the valence band of S2 to act as an oxidation agent while its conduction band acts as a reduction agent. In a typical Type II heterojunction, named "Staggered gap", the electrons from S2 CBE transfer to S1 CBE while the holes from S1 VBE transfer to S2 VBE. Differently, a Z-scheme heterojunction aims for the direct charge transfer from S1 CBE to S2 VBE. Finally, the mismatch of the band alignments in Type III "Broken gap" hinders the charge transfer.

Titania is the most studied semiconductor in photocatalysis due to its highly stable structure, biocompatibility, physical, optical and electrical properties [38]. The anatase phase especially presents good hole transport, which can be combined with different n-type semiconductors that present good electron mobility. Furthermore, a surface heterojunction can be created between different crystalline facets of anatase [39]. Since the surface of each plane termination of the crystal presents a different band structure, the interface between them creates properties similar to heterostructures. Zinc oxide is a composite that shows properties similar to titania, and therefore it is widely applied in wastewater treatment [31]. However, it presents detrimental photocorrosive effects. Iron oxide, even presenting a narrower band gap than titania, is typically not stable in acid aqueous solutions [40]. Cerium oxide is another non-toxic semiconductor non-toxic, with high thermal stability, and can be employed for heterojunctions [41]. Graphene, graphene oxide and reduced graphene oxide are materials used as substrates for supporting semiconductors [42]. Among heterojunctions, various structures have shown excellent activity for methylene blue degradation, for example, $AgBr/BiPO_4$ [43], WO_3/g-C_3N_4 [44], WO_3/ZnO [45], ZnS/CdS [46], $Bi_2O_3/BaTiO_3$ [47] and Co_3O_4/Bi_2WO_6 [48].

The most interesting case is the synergistic effect between two different types of semiconductors. If a p-type semiconductor and a n-type semiconductor are chosen, a p-n junction can potentially be created at the interface. Before contact, their Fermi levels are unaligned, but after contact, their Fermi levels will shift until the equilibrium is reached [49]. Thus, their energy levels will shift accordingly. For the case that the VBE of S1 is lower than that of S2, an internal

electric field is established, leading to an additional charge diffusion at the interface of both materials and the creation of a depletion layer. This phenomenon is schematically illustrated in Figure 8. The decrease in the electron-hole pair recombination leads to a similar effect of Type I or Type II heterojunctions.

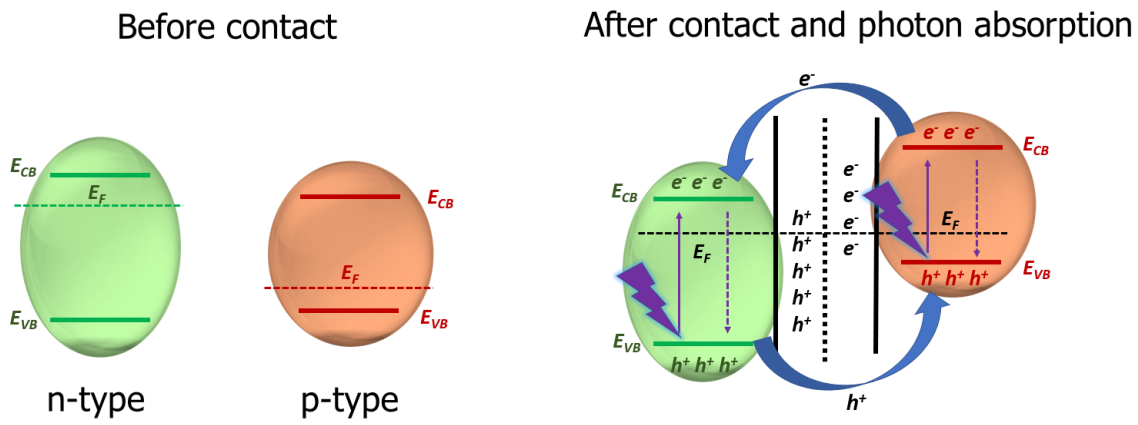

Figure 8 – Schematic representation of a p-n junction energy levels before and after contact.

1.3 $SrTiO_3$-based photocatalysts

The semiconductor $SrTiO_3$ is widely applied in photovoltaic cells [50]. Several studies on the literature have demonstrated its ability in photocatalysis, showing great potential for dye degradation, water-splitting, antibiotic degradation, NO degradation in air and CO_2 reduction reaction. Overall, $SrTiO_3$ can be applied for hydrogen storage, gas sensors, anode for Li-ion batteries and as a substrate for thin film growth [51]. At normal temperature and pressure (NTP), it has a simple cubic perovskite crystal structure with a 3.905 Å lattice parameter, a reported 3.25 eV indirect band gap and a direct band gap as high as 3.75 eV [52, 53]. The perovskite structure was named in 1839 after the discovery of the $CaTiO_3$ perovskite mineral. It is a class of composites that consists of ternary oxides of structure ABO_3, where A is mostly a group I or II element, whereas B is mostly a transition metal [54]. The perovskite exhibits lattice distortion at various extents, which affects the electronic band structure. The melting point of $SrTiO_3$ reaches a high temperature of 2080 K, making it very stable for industrial processes. $SrTiO_3$ nanocrystals present a conduction band edge located at around -0.6 eV (0.2 eV below titania, thus a higher reduction potential) while the valence band edge can be found in 2.6 eV against the NHE. By doping the structure, the Sr^{+2} ions can easily accept electrons (turning into Sr^{+}) and eventually

reduce other adsorbed molecules on the surface of $SrTiO_3$ [51]. The band gap of $SrTiO_3$ has been observed to decrease linearly as a function of the temperature after 500 K [55], and it occurs due to the creation of intra-gap states related to oxygen vacancies. Commercially, the molten salt solid state reaction is an applicable synthesis method, can be scaled up to grams, made in the presence of NaCl and surfactants such as nonylphenyl ether, where the reaction $SrC_2O_4 \rightarrow SrO + CO + CO_2$ produces SrO, reacting with TiO_2: SrO + $TiO_2 \rightarrow SrTiO_3$ to form nanopowder [56].

Piskunov *et al.* [57] have shown by Density Functional Theory (DFT) calculations with the B3LYP functional in a bulk structure that the indirect band gap follows the R-Γ transition while the direct one follows the Γ-Γ transition. Benthem *et al.* [58] showed that, for bulk $SrTiO_3$, the upper valence band contains 18 electrons mainly in O 2p states hybridized with Ti and Sr states. The excitation from this band to Ti 3d and Sr 4d states in the conduction band gives rise to electronic transitions spanning from the indirect band gap energy of 3.25 eV up to 15 eV. Eglitis and Vanderbilt [59] studied the electronic structure of the (001) and (011) $SrTiO_3$ surfaces by DFT. It was found that the surface energies on both SrO and TiO_2 terminations are similar in the (001) surface. Although for the (011) surface the different terminations gave very different surface energies, where the SrO termination has the highest surface energy. The (111) surface was also studied by Sivadas *et al.* [60] by a slab model. Interestingly, it was found that the Fermi level crosses the valence band of the structure in the Ti-SrO_3 terminated surface, giving rise to a metallic-like state. This termination can be stabilized only in a specific thermodynamic condition.

Because of the mixing between the catalyst and the aqueous dye solution, it is necessary to understand the interaction between its different surface configurations and H_2O molecules. Wang *et al.* [61] showed with temperature-programed desorption that H_2O molecules tend to nondissociatively adsorb to the stoichiometric TiO_2 terminated (001) surface of $SrTiO_3$. Nonetheless, the dissociative adsorption has been reported to be possible from other DFT calculations [62, 63], where OH radicals chemisorb at the surface. Steps present on the $SrTiO_3(100)$ surface that connects TiO_2 and SrO terraces facilitate the dissociation of H_2O [64], which should be highly present in nanoparticles. Moreover, the $SrTiO_3(110)$ surface appears to only dissociate H_2O if it presents O vacancies [65].

The structural control of $SrTiO_3$ nanoparticles for methylene blue photodegradation is well documented. Silva *et al.* [28] observed that nanoparticles with a size around 29 nm show

better photocatalytic activity than nanoparticles with smaller sizes and higher surface areas due to the best harnessing of the generated electron-hole pairs. Also, the reaction's mechanism was attributed to a direct valence band hole filling rather than the radicals acting on the dye molecules. Hsieh *et al.* [66] studied how the control of $SrTiO_3$ morphology altered the methylene blue photodegradation. The exposure of (110) facets in dodecahedra-shaped nanoparticles with a mean size of 160 nm increased the reactivity due to a band bending effect created between the different facets. In comparison, cube nanoparticles with only (100) facets present a smaller efficiency [66]. These results are interesting if compared to water dissociation and subsequent creation of radicals. As the $SrTiO_3$(110) surface appears to be more inert towards water dissociation [65], the hole filling observed by Silva *et al.* [28] could be more probable to occur on this facet rather than the formation of radicals. Whereas, the highly irregular (100) surface of $SrTiO_3$ nanoparticles should facilitate the formation of radicals. Results found in the literature for the application of $SrTiO_3$ in methylene blue degradation are summarized in Table 1.

Table 1 – Comparison between methylene blue degradation values from $SrTiO_3$-based photocatalysts.

Reference	Photocatalyst	Light source	Power (W)	MB concentration (ppm)	Reaction time (h)	Estimated degradation
Silva *et al.* [28]	$SrTiO_3$	UV	90	10	6	50%
Chen *et al.* [67]	Zr-$SrTiO_3$	UV	20	10	4	93%
Ghaffari *et al.* [68]	$SrTiO_3$ SrTiFeO	UV	8	3	24	30% 95%
Li *et al.* [69]	$SrTiO_3$ Ni-$SrTiO_3$	Visible	100	20	12	10% 57%
Jia *et al.* [70]	Ni,La-$SrTiO_3$	Visible	100	20	10	60%
Olagunju *et al.* [71]	Pd/$SrTiO_3$	UV	450	10	1	70%
Ferreira *et al.* [72]	$SrTiO_3$/g-C_3N_4	Visible	Not reported	10	7	60%
Bantawal *et al.* [73]	V-$SrTiO_3$	UV	250	10	2	80%
Yanagida *et al.* [74]	$SrTiO_3$-TiO_2	UV	10	3.2	1	90%

Since the band gap of $SrTiO_3$ only allows the absorption of the UV part of the solar spectrum, many works aimed to expand the spectral response by means of doping with metals [67, 68, 69, 70, 73]. For instance, when Ni is applied as a dopant [69, 70], the band gap of $SrTiO_3$

nanoparticles could be reduced to 1.8 eV, allowing the absorption of visible light. Moreover, the electron-hole recombination rate of $SrTiO_3$ impairs its photocatalytic efficiency, and to date, it is still a challenge to find a facile method for avoiding recombination. The combination of $SrTiO_3$ with other semiconductors is a less explored topic in dye degradation processes, although its use in photocatalytic water-splitting reaction shows good results [49, 72, 74, 75]. Additionally, the creation of O vacancies in $SrTiO_3$ can create surface adsorption sites of organic molecules, besides preventing the recombination of photogenerated electron-hole pairs by transferring the charges to the adsorbate [8]. Although the formation of $NiO/SrTiO_3$ heterostructures and O vacancies in $SrTiO_3$ matrix are widely studied in the water-splitting reaction, their applications in dye degradation were not explored yet. These systems are the focus of the present work.

1.3.1 The $NiO/SrTiO_3$ heterojunction

As explained previously, the combination of two semiconductors to create a p-n heterojunction can effectively decrease the electron-hole pair recombination, thus increasing the catalytic efficiency of methylene blue photodegradation. This subsection is devoted to reviewing the history of the $NiO/SrTiO_3$ heterojunction in photocatalysis, exploring its potential use in photodegradation reactions.

Domen *et al.* [75] initially showed the utilization of the $NiO/SrTiO_3$ structure for photocatalytic water-splitting reaction with UV light. This catalyst was prepared by the impregnation of $Ni(NO_3)_2$ (5 wt$\%$) on $SrTiO_3$ powder via an aqueous solution and then calcinated at 400 ºC. They observed that the material was composed of supported NiO nanoparticles on $SrTiO_3$ micrometric particles. After this, the powder was reduced at 500 ºC (turning the Ni nanoparticles into a metallic phase) and then reoxidized at 200 ºC or 500 ºC in order to activate the composite. The nanoparticles oxidized at 500 ºC presented the NiO phase, while those oxidized at 200 ºC were constituted by a metallic core with a NiO shell, showing optimal efficiency for water-splitting [75]. Furthermore, after photoreaction in water, the NiO layer partially turned into $Ni(OH)_2$ due to the instability of NiO in humidity. While the $SrTiO_3$ holes were expected to promote the oxidation of OH radicals into O_2, the authors proposed two different mechanisms for H^+ reduction: either the ions would adsorb on NiO surface, while the metallic Ni should transport the electrons from the $SrTiO_3$ conduction band to the NiO one, or the electrons excited to the conduction band of NiO from light absorption would be the ones to reduce the protons.

Gerhold *et al.* [76] studied the interaction of water with a $SrTiO_3(110)$-(4×1) surface

reconstruction and the effect of NiO heterojunction on this interaction. The surface reconstruction on the pristine $SrTiO_3$ structure compensates the polarity of the (110) crystal plane by varying the Sr/Ti stoichiometry in the near-surface region, making a very inert surface towards the H_2O adsorption. Moreover, they observed that the NiO deposition created sites for H_2O adsorption and shifted the valence band position (although the conduction band was negligibly altered), producing a band-bending effect that increases with the thickness of the NiO layer. The photo-generated excitons dissociate leading to a trapping of electrons and holes in the bulk and surface region, respectively, where the later contributes to the water-splitting reaction. The band gap was altered from 3.2 eV to 1.7 eV after NiO deposition and the TiO_4 tetrahedra of $SrTiO_3$ near NiO distorts.

Townsend *et al.* [52] produced 3 wt$\%$ NiO/$SrTiO_3$ nanoparticles and oxidized them at 130 ºC. They found that NiO/$SrTiO_3$ nanoparticles smaller than 30 nm are less efficient for the water-splitting reaction due to the increase of the overpotential for H_2O oxidation at smaller sizes. Then, they hypothesized that it was NiO that participated in H_2O oxidation instead of $SrTiO_3$, in direct contrast to Domen *et al.*. Later [77], Townsend *et al.* also showed that these nanoparticles are actually composed of three different catalytic centers, Ni-NiO_x-$SrTiO_3$. The $SrTiO_3$ absorbs UV light, metallic Ni layers promote H_2O reduction while NiO_x promotes H_2O oxidation. The photoelectrons were observed to be predominantly located at the $SrTiO_3$ and Ni sites while the holes are located in the NiO_x layer.

Wang *et al.* [49] observed the formation of a p-n junction between n-type $SrTiO_3$ nanocubes and p-type supported NiO nanoparticles, which were synthesized with the $Ni(NO_3)_2$ impregnation and calcination method. The supporting of NiO nanoparticles did not change the band gap of 3.4 eV. By using a $AgNO_3$ sacrificial agent, the O_2 production from water-splitting was 1.7 times higher than a single pristine $SrTiO_3$. Although H_2 production was not detected from the experiment, this could be explained by the absence of metallic Ni in the composite. Figure 9 shows the energy levels alignment of the two materials after contact. Before contact, the valence band edge and the Fermi level of NiO are lower than that of $SrTiO_3$, but, with the contact, the Fermi level of the composite reaches the equilibrium, leading to a shift of the valence band edges. This new difference in potential creates an internal electric field from $SrTiO_3$ to NiO, which helps to transfer the photogenerated holes of $SrTiO_3$ into the valence band of NiO, while the electrons remain in the conduction band of the former, then decreasing the electron-hole pair recombination rate. With the employment of the sacrificial agent, the localized electrons

of $SrTiO_3$ conduction band reduce Ag^+ to Ag^0, leading to a further increased lifetime of the excited state. The formation of a heterojunction between NiO and $SrTiO_3$ was also observed for thin films NiO over $SrTiO_3$ [78] and the charge redistribution observed agrees with the study of Wang *et al.* [49].

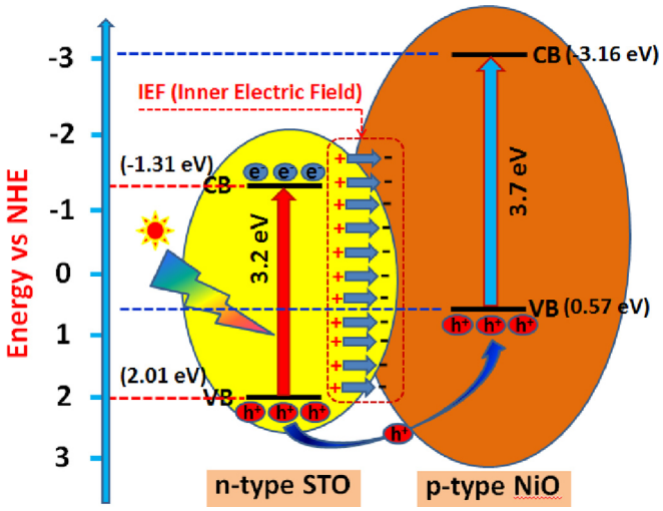

Figure 9 – Formation of a p-n heteterojunction between NiO and $SrTiO_3$ and the energy levels of the two materials. Adapted from [49].

Recently, Wang *et al.* published two DFT studies for $SrTiO_3$ (100) surface with Ni and NiO clusters, and for $SrTiO_3$ and NiO (100) [79, 80]. They observed that in a SrO terminated surface, the increase of metallic Ni up to four atoms in the cluster stabilized the adsorption energy, resulting in an aggregation of Ni atoms. The increase in the number of Ni atoms shifted the Fermi level closer to the conduction band of $SrTiO_3$. Oppositely, in a TiO_2 terminated surface, Ni atoms tend to relax far away from each other, and closer to surface Ti atoms. The Fermi level, in this case, lied inside the conduction band. For the NiO clusters, the most stable structure was Ni_4O_4 at the SrO surface, where the cluster relaxes as a ring structure and its states mix with the valence band of $SrTiO_3$. For the TiO_2 termination, the most stable structure is the NiO cluster with only two atoms. The mixed structure with an interface between $SrTiO_3$ and NiO resulted in the formation of a staggered Type-II heterojunction. Furthermore, it was noted that a covalent type of interaction exists between the NiO and $SrTiO_3$ at the interface, where the SrO terminated surface showed a stronger binding energy. The effective masses of electrons and holes decreased with the heterostructure. It could benefit the separation of photogenerated electrons and holes, then, decrease pair recombination.

From the evolution of these works, the importance of both metallic Ni and NiO for the water-splitting reaction is somewhat understood. However, even if the radicals that are created in

water-splitting are present in dye degradation mechanisms, they are only intermediate states, and a simple extrapolation is not possible. Also, the optimal oxidation state of the Ni components for the photodegradation of dyes remains unclear. It must be elucidated the optimal Ni^0/NiO ratio for photodegradation of methylene blue and the mechanisms behind the reaction.

1.3.2 Creation of O vacancies

In comparison to heterostructures, O vacancies can potentially fix two issues at once: surface and bulk defects. Surface defects contribute to decreased charge recombination by providing adsorption sites in which the carriers can be separated from the material [8]. Bulk defects can decrease the bandgap, allowing visible light absorption in SrTiO3. However, bulk defects can act as recombination centers [8, 33], which decreases the reaction efficiency.

O vacancies in $SrTiO_3$ structure are able to self-doping the material with electron carriers, which causes the insulator-to-metal transition, superconductivity at low temperatures and visible light emitting properties [81]. Although single site vacancies can occur, clustering and ordering of vacancies are often observed in O deficient $SrTiO_3$. Lee *et al.* [81] showed that O divacancies linearly ordered around the Ti atom produce an electronic level inside the gap completely occupied. When four O vacancies were created linearly along the [001] direction in the TiO_2 plane, it was found to be the most stable configuration, producing electronic states inside gap states as well.

The electronic structure of $SrTiO_3$ modified by O vacancies has been explored by Mitra *et al.* [82] with DFT calculations using a hybrid HSE pseudopotential. Other hybrid functionals such as B3LYP have been found to increase the equilibrium volume of $SrTiO_3$ compared to the experimental value, which leads to inaccurate energy values. It was observed that by creating an O vacancy, two Ti atoms move closer to each other. When the vacancy is not ionized, there is an electronic level inside the gap 0.7 eV below the conduction band edge. For single or double ionized O vacancies, these states are pushed closer to the conduction band edge. Moreover, the double ionized state is found to be the most stable configuration, representing an electron donation characteristic.

Tan *et al.* [8] studied a solid grinding reaction between $SrTiO_3$ and $NaBH_4$ to create surface O vacancies by applying the obtained material for the photocatalytic water-splitting reaction with methanol as the sacrificial agent. They observed that a pre-heating treatment of the material at 325 ºC for 60 min is able to double the hydrogen production compared to the

pristine $SrTiO_3$ without O vacancies. Since the O vacancies act as electron donors, the charge transport in $SrTiO_3$ was improved. Additionally, as the Fermi level shifts towards the conduction band, it helps to improve the charge separation. However, there is an optimal O vacancy amount for a water-splitting reaction. Whether the O vacancy amount is above a threshold value, the vacancies act as charge recombination centers, lowering the free carrier mobility and decreasing the hydrogen production rate.

Kumar *et al.* [83] studied the application of ball milling process in order to decrease particle size and to create O vacancies in $SrTiO_3$. With the increase of the ball milling time up to 20 h, the particles size decreased from 38 nm to 28 nm, and the lattice strain increased. The increase in the O vacancies amounts induced an increase at 412 nm wavelength emission in the photoluminescence spectrum. The body-centered Ti ion motions caused by the O vacancies in the octahedral structure induced a phonon frequency observed in Raman spectra. Although the band gap was negligibly altered, methylene blue photodegradation with UV light presented an increase in degradation rate from 0.013 min^{-1} (without vacancies) to 0.019 min^{-1}, probably due to the decrease in charge recombination rate.

Sun and Lu [84] applied nitrogen ion bombardment (1.5 keV) on $SrTiO_3(100)$ crystal while heating the sample with an electron-beam heater at 1000 K and applied it in the photodegradation of methylene blue. The ion caused a lattice strain over 7 nm distance from the surface. The band gap was narrowed to 2.1 eV, then extending the light absorption to the visible regime. The implantation caused surface defects that acted as extra adsorption sites, thus facilitating the photocatalytic reaction. When irradiating the samples with UV light, the sample that received the bombardment was able to degrade a 0.01 mmol/L methylene blue solution in 4 hours while the sample that did not receive the bombardment required over 8 hours to degrade the same amount.

The creation of O vacancies in $SrTiO_3$ for photocatalytic reactions is promising. However, there is still a small number of possibilities studied to create these types of defects in the structure, and there is a need to deeply understand the reaction mechanisms the vacancies promote. For example, it must be answered whether the mechanism of reaction remains the same and the band gap and electron-hole recombination rates are altered or the mechanism of methylene blue photodegradation changes in the presence of surface vacancies.

2 Physical phenomena and theoretical background of the methods of analysis

In this chapter, a major review will be made about the physical phenomena of the experimental techniques and theoretical methods used throughout the present work.

2.1 X-ray generation

The use of electromagnetic radiation in the 21st century is one of the pillars that maintain humankind in the path to progress. In special, materials science depends strongly on X-rays based methods of analysis, where incident X-rays can be transmitted, scattered or absorbed by the material structure. In this section, two possibilities for X-ray generation will be discussed: the conventional X-ray tubes and synchrotron accelerators.

2.1.1 X-ray tubes

The fundamental generation of X-rays lies in the manipulation of charged particles. When a charged particle such as an electron is decelerated, electromagnetic radiation is emitted [85]. X-rays are emitted by this particle when it has a large enough kinetic energy. This type of emission by a sudden deceleration is commonly called *bremsstrahlung*. The X-rays are emitted continuously in a given wavelength range, as shown in Figure 10. It is possible to observe also the presence of characteristic radiation, which overlaps with the *bremsstrahlung* radiation detected.

An X-ray tube consists primarily of one electron source and two metal electrodes, as shown in Figure 11. When the electron source is heated up to high temperatures, electrons are emitted from the material. By applying a difference of electric potential at the two metal electrodes, the electrons can then be accelerated to high speeds in a vacuum towards the anode target material (commonly Cu or Mo). Besides the *bremsstrahlung* radiation, there is also the emission of characteristic radiation by exciting the target.

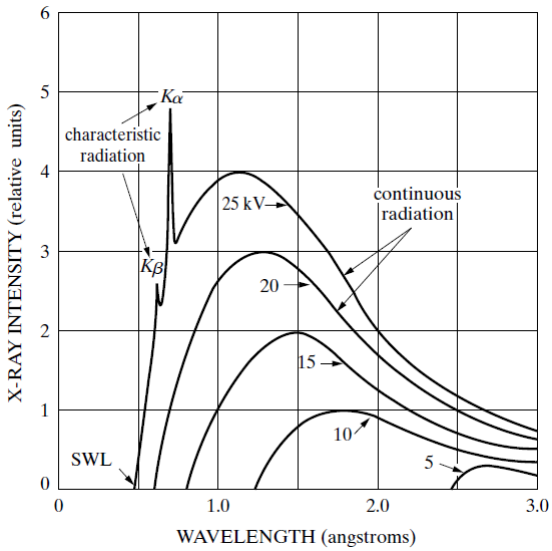

Figure 10 – X-ray emission spectrum of a Mo target due to the incidence of an electron beam as a function of applied voltage. Aside from the *bremsstrahlung*, the characteristic radiation from the excitation of the material is present in the higher applied voltage. Adapted from [85].

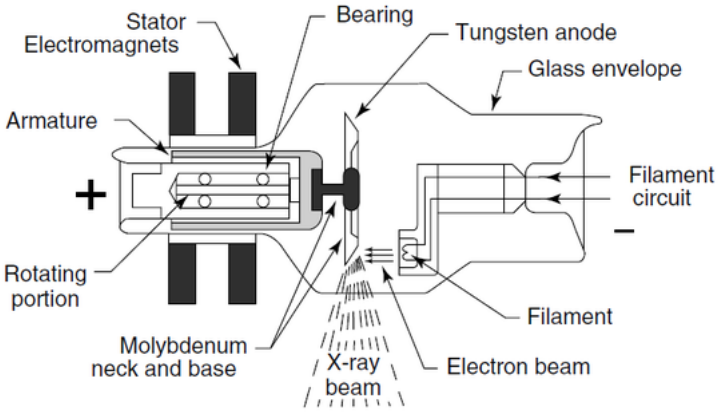

Figure 11 – Schematic representation of a rotating-anode X-ray tube. Adapted from [86].

Different types of X-rays tubes were created over the decades, such as gas tubes, filament tubes, rotating-anode tubes, microfocus tubes and flash tubes. Eventually, the intensity of the X-rays may be low enough for the study with state-of-the-art techniques, and the accelerator technology must be used.

2.1.2 Synchrotron radiation

Synchrotron radiation is defined as the light emission when relativistic charged particles are deflected by a magnetic field [87, 88]. The advantages of synchrotron radiation include high brilliance (photon flux normalized over the solid angle of emission), the possibility of tuning the X-rays energy in a wide spectral range, the adjustable polarization of X-rays from an

elliptical base, the short temporal pulses that can be used in time resolved experiments and the highly collimated light beam, which is used for space resolved experiments. The electromagnetic radiation emitted by the deflection of subrelativistic charged particles is symmetric, as shown in Figure 12. However, for charged particles with speeds getting closer to the speed of light, the radiation is emitted in a tangential direction to the particle path and in a cone-shaped form with a small divergence. In a synchrotron source, the emission of electromagnetic radiation can be visualized by the Compton effect, in which electrons in the vacuum interact with an external magnetic field (acting as virtual photons) exchanging energy and losing momentum, and then, after this intermediate state, the electron emits a photon to reach its final ground state.

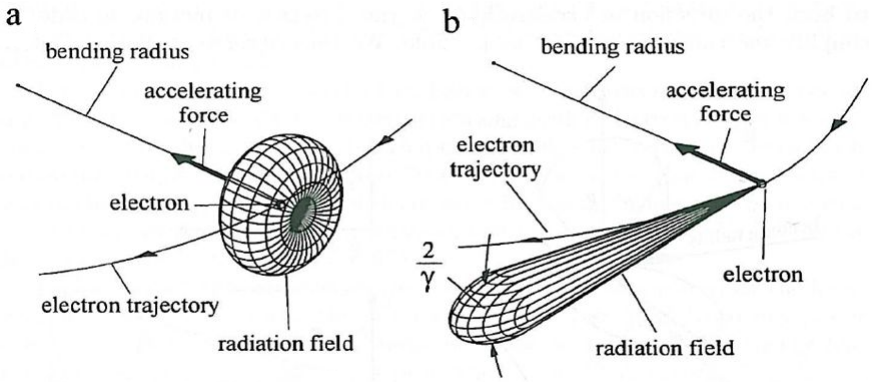

Figure 12 – Representation of an angular distribution of radiation emitted by (a) a sub-relativistic particle and (b) a relativistic particle. Adapted from [89].

Electromagnetic radiation may exist as long as the Poynting vector $\mathbf{S} = 1/\mu_0 \mathbf{E} \times \mathbf{B}$ is non-zero. The Liénard-Wiechert potentials express the fields of a moving charge as a function of the retarded time $t_r = t - \frac{1}{c}|\mathbf{r} - \mathbf{r}'|$:

$$\varphi(\mathbf{r}, t) = \frac{1}{4\pi\epsilon_0} \left(\frac{q}{(1 - \hat{\mathbf{R}} \cdot \boldsymbol{\beta}) R} \right)_{t_r} \tag{2.1}$$

$$\mathbf{A}(\mathbf{r}, t) = \frac{\mu_0 c}{4\pi} \left(\frac{q\boldsymbol{\beta}}{(1 - \hat{\mathbf{R}} \cdot \boldsymbol{\beta}) R} \right)_{t_r} = \frac{\boldsymbol{\beta}(t_r)}{c} \varphi(\mathbf{r}, t) \tag{2.2}$$

$$\boldsymbol{\beta}(t) = \frac{\mathbf{v}_0(t)}{c}, \quad \hat{\mathbf{R}} = \frac{\mathbf{R}}{R}, \quad \mathbf{R} = \mathbf{r} - \mathbf{r}_0 \tag{2.3}$$

where $\mathbf{r}_0$ is the position of the source of charge and $\mathbf{v}_0$ its speed. By using the Lorentz factor γ, the electric field of this charged particle reads as:

$$\mathbf{E} = \frac{e}{4\pi\epsilon_0} \left[R \frac{\hat{\mathbf{R}} + \boldsymbol{\beta}}{\gamma^2 r^3} + \frac{R^2}{cr^3} \left[\hat{\mathbf{R}} \times \left(\left(\hat{\mathbf{R}} + \boldsymbol{\beta} \right) \times \frac{d\boldsymbol{\beta}}{dt_r} \right) \right] \right]_{t_r} \tag{2.4}$$

The first term of this equation represents the Coulomb regime, related to the intrinsic electric field the particle generates. It is mainly responsible for the transport of electromagnetic energy along transmission lines. The second term represents the radiation regime, related to the distortions in the electric field created by the acceleration of the particle. Therefore, it is responsible for the emission of synchrotron radiation. For an observer at rest relative to the moving particle, the total power in the laboratory frame system reads as:

$$P = \frac{e^2}{6\pi\epsilon_0 c}\gamma^6 \left[\dot{\boldsymbol{\beta}}^2 - \left(\boldsymbol{\beta} \times \dot{\boldsymbol{\beta}}\right)^2\right] \tag{2.5}$$

The radiation from relativistic particles observed at the laboratory reference frame is seen collimated due to the relativistic Doppler effect, and the angle of emission can be approximated by $\Delta\theta \approx \pm 1/\gamma$.

In a synchrotron laboratory, the electrons (or positrons) are usually previously accelerated by a linear accelerator (LINAC) up to hundreds of MeV, and then inserted in a secondary ring named booster. Inside the booster, the charged particles are again accelerated to the final energy (few GeV) and transferred to the storage ring. Inside the storage ring, the electrons travel as equidistant bunches of particles in a polygonal (almost circular) path, being deflected by a magnetic field perpendicular to the electron trajectory, then releasing electromagnetic radiation composed of multiple types of light wave harmonics. The harmonic frequencies are related to the particle revolution frequency in the ring and can be expressed by a combination of modified Bessel functions. The magnetic field can be created with bending magnets and insertion devices, where the later consists of the wavelength shifter, undulator or wiggler magnets. A bending magnet emits a broad continuous spectrum, and the power of radiation emitted is given by:

$$P_\gamma = C_B B^2 E^2, \quad C_B \approx 6.0779 \times 10^{-8}\ \text{W/T}^2\text{GeV}^2 \tag{2.6}$$

where the magnetic field B can be expressed in terms of the bending radius. Also, special components named accelerating structures or resonant cavities supply energy for the maintenance of the relativistic speed of the electrons, since the electron beam loses energy by colliding with the residual molecules present in the storage ring, even when maintained in an ultra-high vacuum. An overall schematic representation of a synchrotron ring is shown in Figure 13.

At each node, where the radiation is emitted by the use of magnets, an experimental beamline collects the incoming photons. Each beamline has a number of different equipments installed, depending on the purpose of the beamline. Windows allow the radiation to pass through

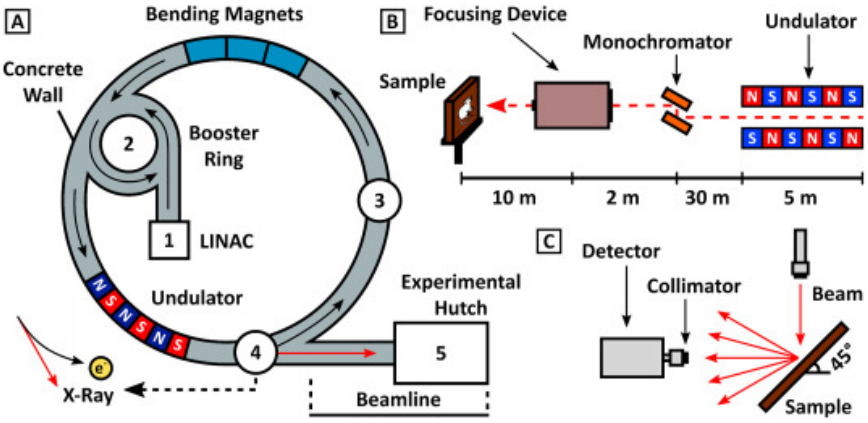

Figure 13 – Schematic representation inside a synchrotron facility. Adapted from [90].

and reach the beamline besides maintaining the ultra-high vacuum in the storage ring. Slits control the size of the radiation beam. Mirrors collimate and reflect the incoming light to the sample position. A monochromator narrows the wavelength distribution of the incident spectrum, ideally selecting a single wavelength. Finally, the collimated and monochromatic light reaches the workstation, enabling the use of multiple advanced and state-of-the-art techniques to characterize the sample.

2.2 X-Ray Diffraction

X-Ray Diffraction (XRD) is one of the most routinely applied experimental techniques that assist in the determination of the structural configuration of a crystalline sample. In this technique, a monochromatic X-ray beam is focused on the sample and scattered. The scattered light is collected and analyzed as a function of the scattering angle of the X-rays. Crystallite grain size, phase composition and overall structural information can be obtained.

The diffraction of light is fundamentally a scattering phenomenon. The scattering of electromagnetic waves is divided into two major processes: elastic and inelastic scattering. Elastic scattering can be viewed as the conservation of the wavelength between the incident and scattered wave. Defining the wavenumber as $|\mathbf{k}| = 2\pi/\lambda$, this quantity must be conserved in elastic scattering: $|\mathbf{k}'| = |\mathbf{k}|$. It can be observed in different mechanisms, such as Thompson, Rayleigh or Mie scattering. Inelastic scattering is most commonly observed through the Compton effect, in which a photon is scattered by an electron. The incident photon loses energy in the process so that the wavelength of the scattered photon increases. Another important difference between these events is that elastic scattering is coherent, where a stationary interference pattern can be originated, while inelastic scattering is incoherent. The scattering source of X-rays in

materials are the electrons and each electron contributes to the total observed XRD pattern. Figure 14 illustrates the X-ray scattering by the atomic planes.

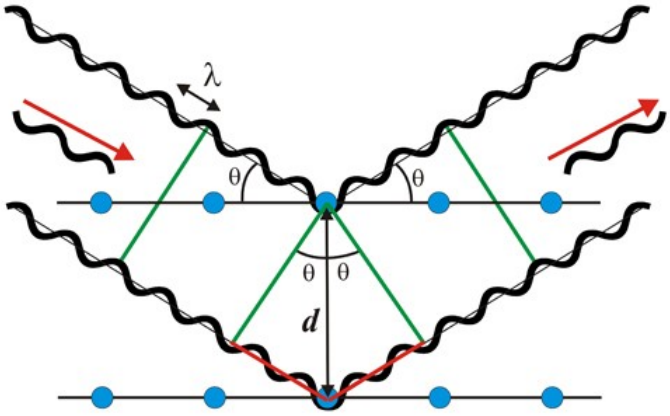

Figure 14 – Representation of X-ray scattering in the atomic planes.

Inspired by P.P. Ewald's dissertation about the scattering of electromagnetic radiation, the German physicist Max von Laue in 1912 proposed that crystals could be used to diffract X-rays, latter receiving the Nobel prize for it [85]. The father W. H. Bragg and son W. L. Bragg had a stimulus from the initial experiments of diffraction and devised a simple mathematical condition so that the X-rays diffracted in the crystalline planes of the materials show constructive interference, nowadays famously known as Bragg's law [85]:

$$2d \sin\theta = n\lambda \tag{2.7}$$

The term d represents the distance between consecutive planes, θ represents the angle between the X-ray beam incidence and a family of parallel planes, λ is the X-ray wavelength and n is an integer known as the order of diffraction. The equation considers the difference in path traveled by two wavefronts, such that there is a constructive interference between them. It can be perceived that constructive interference of the X-rays by an atomic plane can only be observed in specific angles θ. Indeed, the diffraction patterns of different materials are composed of Bragg reflections at different angles that represent the constructive interference generated by the different atomic planes. A typical X-ray diffractogram is shown in Figure 15.

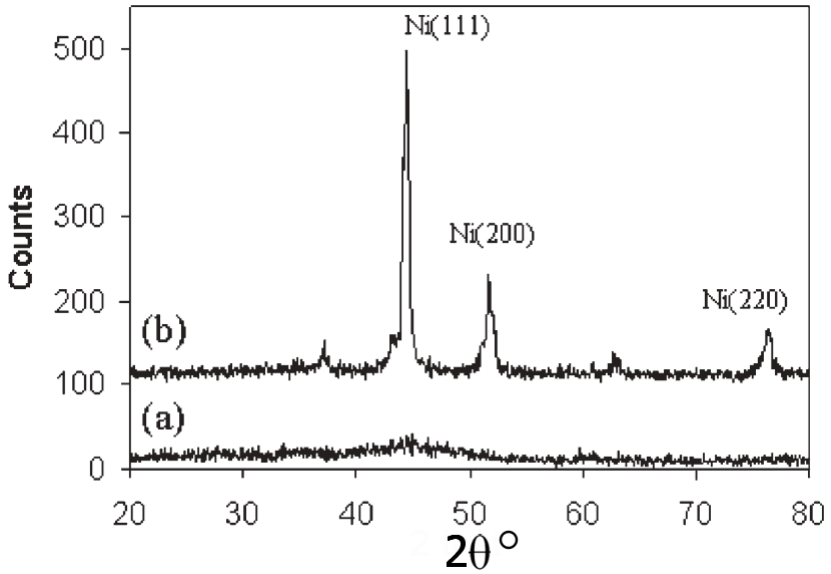

Figure 15 – Typical diffractogram of (a) an amorphous and (b) crystalline Ni catalyst generated by Cu-Kα radiation. Adapted from [91].

The X-rays are scattered in every direction by the electrons. But the intensity of the scattered X-rays varies with the angle of scattering. The intensity I_P of the scattered X-rays at a point P due to an electron is given by the Thompson equation:

$$I_p = I_0 \frac{K}{r^2} \left(\frac{1 + \cos^2 2\theta}{2} \right) \tag{2.8}$$

where I_0 is the intensity of the incident beam, r the distance between the sample and the point P P, K a constant and the expression inside the parenthesis is known as the polarization factor. This factor is a correction due to an unpolarized incident beam, meaning that the electromagnetic field of light points in a random direction but, on average, the tangential and normal components are equal.

The scattering of the X-rays by an atom depends on the form factor, f_i. This factor is defined as the ratio between the scattering amplitude by the atom to the scattering amplitude by the electron. Similarly, the structure factor F_{hkl} takes into account the scattering amplitude by the unit cell in comparison to that of a single atom and it is given by

$$F_{hkl} = \sum_i f_i e^{-i\mathbf{q}\cdot\mathbf{r}_i}, \quad \mathbf{q} = h\mathbf{b}_1 + k\mathbf{b}_2 + l\mathbf{b}_3 \tag{2.9}$$

where the scattering amplitude of the crystal unit cell F_{hkl} for the specific Miller index is summed over all the atomic positions $\mathbf{r}_i$ in a Fourier transform. The intensity detected in the XRD technique depends on the $|F_{hkl}|^2$. Another addition to the intensity measured in XRD

refers to the multiplicity factor, Π, for a family of planes. For example, the $\{100\}$ represents the Miller planes (100), (010), (001), $(\bar{1}00)$, $(0\bar{1}0)$ and $(00\bar{1})$ that contribute to the same Bragg reflection, then the multiplicity factor in this case is 6. The incident beam divergence and partial beam monochromatization are taken into account by the Lorentz factor that, together with the polarization factor of equation 2.8, gives the Lorentz polarization factor making the intensity proportional to $(1 + \cos^2(2\theta))/(8\sin^2(\theta)\cos(\theta))$.

Two other corrections should be made as well: the absorption factor and the temperature factor. The absorption factor $A(\theta)$ multiplies the total scattered intensity and it is proportional to the integration of a function $e^{-\mu p(\theta)}$ over the cross sectional area, where μ is the absorption coefficient of the sample and p is the path traveled by the X-rays waves inside the sample, that depends on the angle of incidence. The temperature factor correlates the atomic vibration to the atomic position. The greater the vibrational disorder, the lower the intensity of the Bragg reflection. This term is given by the expression e^{-2M}, where $M > 0$ and it increases with the scattering angle, decreasing the value of the exponential. For a cubic structure material, the Debye formula for the i'th-atom reads as:

$$M_i = \frac{6h^2T}{m_i k\Theta^2}\left[\phi\left(\frac{\Theta}{T}\right) + \frac{\Theta}{4T}\right]\left(\frac{\sin\theta}{\lambda}\right)^2 \tag{2.10}$$

where h is the Planck's constant, T the temperature, m_i the atomic mass, k the Boltzmann's constant, Θ the Debye characteristic temperature of the material and ϕ is a tabulated function. Then, the total XRD intensity is given by

$$I_p = |F_{hkl}|^2 \Pi A(\theta) e^{-\mu p(\theta)}\left(\frac{1+\cos^2 2\theta}{8\sin^2\theta\cos\theta}\right) \tag{2.11}$$

There are three traditional methods for measuring the XRD pattern: Laue's method, the rotating-crystal and the powder diffraction method. In Laue's method, a polychromatic X-ray beam is focused on the sample and the X-ray intensity is measured at a fixed angle θ. The rotating-crystal method uses a monochromatic X-rays beam focused on a single crystal that rotates around one of its crystallographic directions. The crystal is rotated and when Bragg's condition is satisfied for a certain set of planes, a high X-ray intensity is measured. The most used method is the powder method, where large crystals are pulverized to a fine powder. The microscopic grains of the powder are randomly oriented relative to the incident X-rays beam. Then a monochromatic X-ray beam is focused on the sample and the Bragg's condition is met for a given angle depending on the atomic plane orientation.

The conventional XRD setup uses monochromatic X-rays, usually Cu Kα or Mo Kα from X-rays tubes, and the diffraction pattern is obtained through the variation of the diffraction angle 2θ. A filter that absorbs Kβ radiation of the X-rays tube and a monochromator that selects the Kα line radiation apart from the continuous background, using Bragg's law, enables obtaining the monochromatic beam. Scintillation counters coupled with a photomultiplier tube are traditionally used as detectors. A usual experimental setup is called Bragg-Brentano geometry (represented in Figure 16), where two precise goniometers define the angle between the incident X-rays (tube) and the sample and between the sample and the detector. Additionally, they can be $\theta - \theta$ type, where the tube and the detector move with the same angle variation with a fixed sample, or a $\theta - 2\theta$ type, where the tube is fixed, the sample is rotated at an angle θ and the detector must be moved at an angle 2θ to compensate the variation.

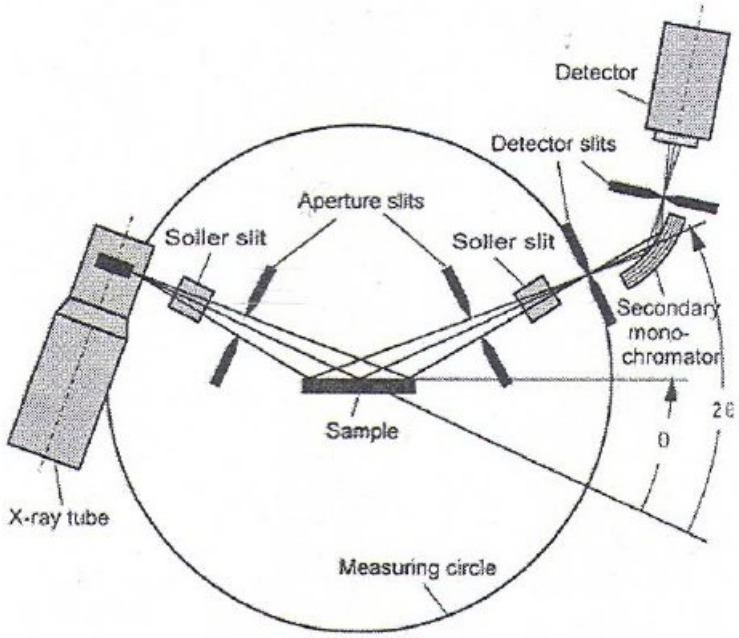

Figure 16 – Illustration of a Bragg-Brentano XRD geometry used in most modern equipments. Adapted from [85].

2.2.1 Size determination and the Rietveld Refinement

An initial approximation for the obtainment of the mean crystallite size is through Scherrer's equation [92]:

$$D_{hkl} = 0.9\lambda \frac{\sqrt{B_0^2(2\theta) - B_{std}^2(2\theta)}}{\cos\theta} \tag{2.12}$$

where D_{hkl} is the crystallite size obtained from (hkl) Bragg reflection, the constant 0.9 corresponds to a spherical morphology, B_0 is the full width at half maximum (FWHM) of the (hkl)

Bragg reflection and B_{std} the FWHM of a standard sample used to take into account the system resolution. Effects of strain inside the grains, i.e., dislocations of the crystalline planes induced by disorder, can shift the Bragg reflection if the strain is uniform (macrostrains) or broaden it if the strain is non-uniform (microstrains). Debye-Scherrer's equation is a simple procedure that provides relatively good results. Nevertheless, because of multiple effects such as the strain or unit cell expansion and contraction of a polycrystalline sample, a more robust approach can be employed.

The Rietveld method can fit an entire XRD pattern, provided that the crystallographic composition of the sample is known. Then, atomic positions, occupation numbers, lattice parameters and space groups, which are cataloged in large databases such as the Inorganic Crystal Structure Database (ICSD) or optimized through an *ab initio* computational method, are used as input in the Rietveld refinement method. The Rietveld method uses a least-squares optimization procedure to adapt the calculated values to the experimental ones, through the minimization of the χ^2 statistical parameter:

$$\chi^2 = \sum_i w_i [I_i(data) - I_i(calculated)]^2 \tag{2.13}$$

Furthermore, instrumental profile and shape parameters must be fitted as well. The Rietveld refinement method allows obtaining, besides the mean crystallite size, the strain, lattice parameter and fraction of the crystal phases existing in the sample. An amorphous fraction can be deduced as well by analyzing the background of the XRD pattern.

The peak shape of the diffraction pattern is usually described by a Pseudo-Voigt function, which is a weighted sum of a Lorentzian and a Gaussian function. Additionally, to correct axial divergence that leads to peak asymmetry, a modified Pseudo-Voigt function known as the Thompson-Cox-Hastings correction can be applied [93].

The background is usually subtracted by an algorithm of selection of points and linear or spline interpolations. After the background subtraction, agreement factors such as the weighted profile R_{wp} index or the expected profile R_{exp} defined below may be observed throughout the fitting process, and both help to provide an indicator along with the χ^2 value:

$$R_{wp} = 100 \, \frac{\sum_i w_i [I_i(subtracted) - I_i(calculated)]^2}{\sum_i w_i I_i(subtracted)^2} \tag{2.14}$$

$$R_{exp} = \frac{\sqrt{n-m}}{\sum_i w_i I_i(subtracted)^2} \tag{2.15}$$

where n is the fitting procedure number of steps and m the number of fitted parameters.

2.3 Small-Angle X-Ray Scattering

The Small-Angle X-ray Scattering (SAXS) technique is used to determine the morphology of nanoparticles. In a SAXS experiment using transmission mode, one desires to measure the intensity of the X-rays scattered by the sample as a function of the scattering angle after the transmission of the incident beam flux through the sample. As the name suggests, the scattering angles probed in this type of experiment are usually between 0 ° and 5 °. A detailed analysis consists of obtaining information about the size, shape and electronic density of different nanostructures populations in the sample through the fitting of the scattering pattern. The experimental setup allows probing sizes ranging from 1 nm to a few hundred nanometers [94, 95, 96]. The SAXS pattern is usually represented by intensity as a function of the scattering vector $\mathbf{q} = \mathbf{k} - \mathbf{k}'$, which is defined as the difference between the wavevector of the incident and scattered X-rays, which can be related to the scattering angle 2θ shown in Figure 17:

$$q = \frac{4\pi}{\lambda} \sin\theta \tag{2.16}$$

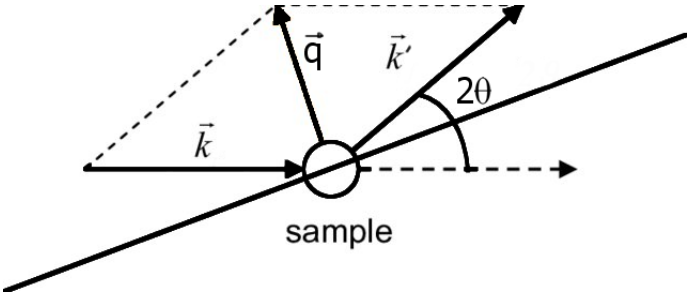

Figure 17 – Scattering vector $\mathbf{q}$ definition.

where λ is the wavelength of the incident X-ray. Since the electrons are not spatially localized, it is proposed that the electronic density function $\rho(\mathbf{r})$ can describe the average behavior of the structures composing the material. The scattering amplitude of a single primary nanoparticle, known as the form factor, can be derived as the Fourier transform of this electronic density function:

$$f(\mathbf{q}) = \int d\mathbf{r}' \rho(\mathbf{r}') e^{-i\mathbf{q}\cdot\mathbf{r}'} \tag{2.17}$$

The intensity of the scattered X-rays, which is proportional to the differential cross section of scattering, is defined as the absolute squared value of the form factor:

$$I(\mathbf{q}) = |f(\mathbf{q})|^2 = \int d\mathbf{r}_1 d\mathbf{r}_2 \rho(\mathbf{r_1})\rho(\mathbf{r_2}) e^{-i\mathbf{q}(\mathbf{r_1}-\mathbf{r_2})} = \int d\mathbf{r} \widetilde{\rho}^2 e^{-i\mathbf{q}\cdot\mathbf{r}} \tag{2.18}$$

where the last integral is performed over the relative distances $\mathbf{r}$. The element $\tilde{\rho}$ is the convolution function, or auto-correlation function, and it represents the density of electron pairs with a certain relative distance:

$$\widetilde{\rho}^2 = \int d\mathbf{r}_1 \rho(\mathbf{r_1})\rho(\mathbf{r_2}), \qquad \mathbf{r} = \mathbf{r_1} - \mathbf{r_2} \tag{2.19}$$

Two hypothesis can be established to proceed with this analysis. Firstly, it is supposed that the system under study is spatially isotropic so that the exponential of the Fourier Transform can be averaged to a function of $\sin(qr)/(qr)$. Secondly, there is not a correlation between two sufficiently distant points, which is interpreted as the system not having a long range order. Over large distances, only an average value of ρ exists. This leads to a subtraction of this average value of ρ from the electronic density:

$$\eta(r) = \rho(r) - \langle\rho\rangle \quad \Rightarrow \quad I(q) = \int d\mathbf{r}\ \widetilde{\eta}^2(r)\frac{\sin(qr)}{qr} \tag{2.20}$$

where the electronic density fluctuation is defined. Next, a correlation function related to the well-known pair-distance distribution function, $\gamma(r)$, is defined from the previous element. This represents the average $\langle\eta(\mathbf{r_1})\eta(\mathbf{r_2})\rangle$.

$$V\gamma(r) = \widetilde{\eta}^2 \quad \Rightarrow \quad I(q) = V\int d\mathbf{r}\ \gamma(r)\frac{\sin(qr)}{qr} \tag{2.21}$$

The inverse Fourier transform leads to:

$$V\gamma(r) = \int d^3q\ I(q)\frac{\sin(qr)}{qr} \tag{2.22}$$

The derivation for the form factor of a spherical nanoparticle, with radius R and a difference between the electronic density fluctuation of the particle and the matrix $\Delta\eta$, is trivial within this formulation [97]:

$$f(q) = 4\pi\Delta\eta\int_0^R \frac{\sin(qr)}{qr}r^2 dr = 4\pi\Delta\eta\left(\frac{\sin(qR) - qRcos(qR)}{q}\right) = f_{sp}(q, R, \Delta\eta) \tag{2.23}$$

The form factor of a spherical nanoparticle with a core-shell like structure can be derived from equation (2.23):

$$f_{cs} = f_{sp}(q, R_{shell} + R_{core}, \Delta\eta_{shell}) - f_{sp}(q, R_{core}, \Delta\eta_{shell} - \Delta\eta_{core}) \tag{2.24}$$

Generally, in the case of a dilute population of nanostructures, the intensity can be obtained through:

$$I(q) = \Delta\eta^2 \, V^2 \, |f(q)|^2 \tag{2.25}$$

For a polydisperse system, in which there are multiple populations of different nanostructures, the intensity can be obtained through:

$$I(q) = \sum_i \int_0^\infty n_i(r) V_i^2(r) \, |f_i(q)|^2 dr \tag{2.26}$$

where f_i represents the intensity of each separate population and n_i the statistical size distribution of each population, which the most commonly used for polydispersed nanoparticles are Gaussian, log-normal and Schull-Zimm distributions [96]. If the system is composed of multiple nanostructures, then the structure factor may be defined similarly to XRD:

$$F(q) = \sum_i^N f_i(q) e^{-iqr_i} \tag{2.27}$$

Then, the intensity is the absolute squared of the average over all possible structural orientations:

$$I(q) = \left\langle \sum_i \sum_j f_i f_j^* e^{-iq(r_i - r_j)} \right\rangle = \tag{2.28}$$

$$\sum_i^N I_i(q) + 2 \left\langle \sum \sum_{j \neq k} |f_i||f_j^*| \cos\left[q(r_i - r_j) + \varphi_k - \varphi_j\right] \right\rangle \tag{2.29}$$

The fitting process of a SAXS pattern considers different existing approximations in order to obtain the intensity using a form factor and a structure factor, such as the monodisperse approach, decoupling approximation, local monodisperse approximation or size-spacing correlation approximation. Figure 18 shows an example of SAXS patterns of 10 nm monodisperse nanoparticles, polydisperse nanoparticles with an average size of 10 nm and a polydisperse system formed by 4 nanoparticles with similar size in a tetrahedron-like structure [98].

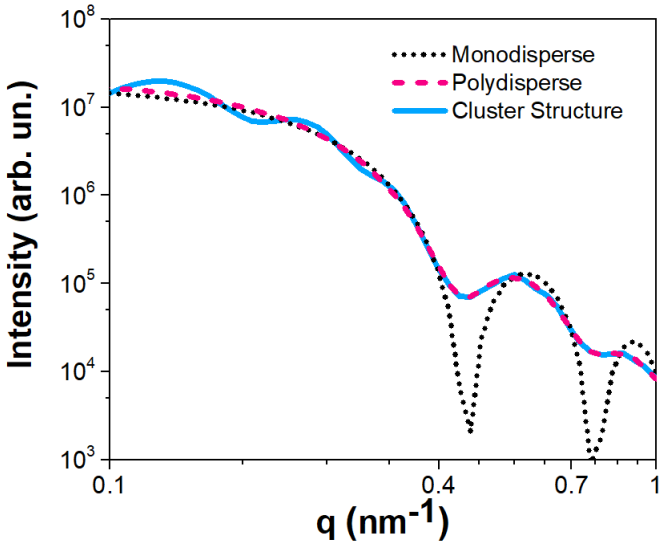

Figure 18 – Comparison between different SAXS patterns of nanoparticles.

The experimental setup of a SAXS experiment is represented in Figure 19. The system is evacuated, usually to 10^{-2} mbar in laboratory instruments, in order to reduce the scattering of the X-ray beam by the atmosphere. The incident X-rays can be generated through a conventional X-ray tube or with synchrotron radiation. X-rays emitted by conventional sources are usually polychromatic, and in order to prevent instrumental broadening a monochromator must be used. A usual way to monochromatize is to use pulse-height discriminators combined with a filter for the absorption of Kβ radiation and a crystal analyzer that selects the Kα wavelength of the X-ray source by applying Bragg's law.

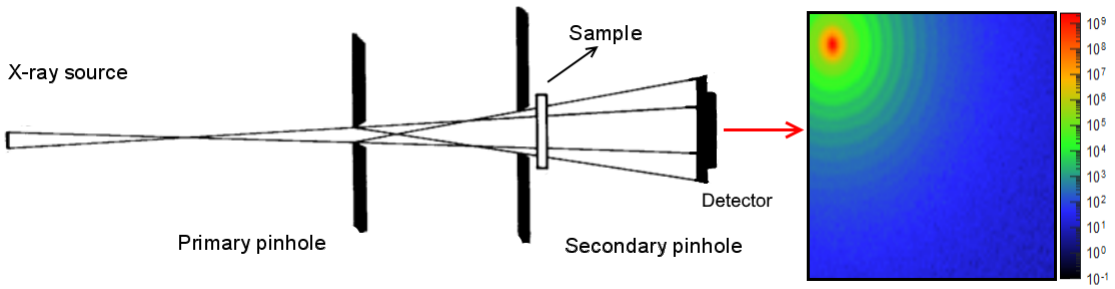

Figure 19 – Representation of SAXS pinhole collimation instrumentation. Adapted from [98, 94].

It is also important to separate the incident X-ray beam from the scattered X-ray beam at Small-Angles. This is accomplished by the use of a collimation system. Collimation can be divided between slit or point instrumentation. Slit collimation, also called line collimation, molds the X-ray beam practically in one dimension. An issue of this method is that the shape of the slit imposes a convolution with the incoming X-ray beam, which causes instrumental broadening,

specially at small angles. Point collimation molds the X-ray beam into a conical form by using small orifices called pinholes so that only a small area of the samples is illuminated. As the pattern obtained in the detector plane is symmetric with its center, the broadening is almost imperceptible. However, the intensity at the sample position is poorer and it implies longer measurements.

2.4 Transmission Electron Microscopy

The Transmission Electron Microscopy (TEM) technique is used for obtaining images of samples and direct morphology information. In a TEM experiment, an incident electron beam is [85] transmitted through the sample, which is thin (around 100 nm thickness), forming an image at the projection plane. The contrast comes from the electronic density and thickness. The areas of the image appearing darker represent regions with higher atomic density or thicker. The possibility of high magnification and the combination of diffraction and other spectroscopy measurements make TEM a great tool over other microscopy techniques, but ultimately the difficulty to obtain well prepared and representative samples impose some limitations to the technique [99].

The incident electron beam can be described as a plane wave due to the wave-particle duality, which has a de Broglie wavelength of $\lambda_e = h/\sqrt{2m_e E_0}$, where E_0 is the energy of the accelerated electrons. A standard transmission microscope usually accelerates the beam to energies between 80 keV and 300 keV. The electron beam suffers multiple types of interaction with the sample, such as backscattering and high angle scattering, that are mainly produced by the nuclei while the sample electrons mainly produce low angle scattering and inelastic scattering of the electron beam. Simultaneously, the electron beam excites the sample, and the relaxation process leads to the emission of secondary electrons, characteristic X-rays, Auger electrons and multiple other effects.

Figure 20 shows an illustration of a standard transmission electron microscope, kept in a high vacuum (around 10^{-7} mbar). Electron guns are mainly encountered in three different types: Thermionic Emission Sources, Schottky Emission Sources and Field Emission Sources. A thermionic emission source, commonly called a triode gun, is composed of a cathode filament (the source of the electrons from Joule's effect), a Wehnelt cylinder and an anode for the acceleration of the electrons. A negative potential bias is applied between the Wehnelt cylinder and the emitter,

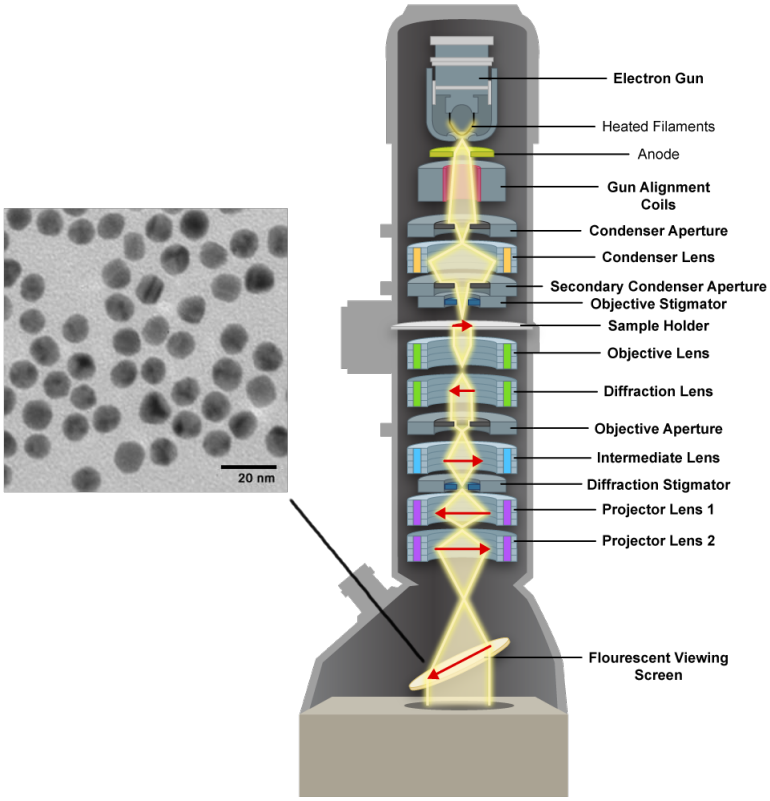

Figure 20 – Representation of a transmission electron microscope, its components and typical images obtained for nanoparticles. Adapted from [100].

while the acceleration anode receives a positive potential bias.

Magnetic lenses focus the electron beam in the sample, converge the beam for image formation and employ aberration corrections. The condenser lenses focus the beam on the sample, while the intermediate and projector lenses control the magnification and focus the transmitted beam towards a phosphorescent screen or CCD camera where the image is formed. The apertures are circular orifices that control the lateral width of the beam, thus providing beam collimation. While the condenser lenses aperture defines the convergence beam angle over the sample, the objective lenses aperture defines the selection of dark or bright fields.

Nanoparticle (powder) sample preparation is usually the most simple TEM preparation method. The powder is dispersed in a solution. Then, a drop is deposited over a grid covered with some carbon-based film.

2.5 UV-Visible Spectroscopy

UV-Visible spectroscopy is a standard technique to estimate both the degradation of molecules in solution after a photoreaction and the band gap of materials [11, 101]. It is based

on the measurement of the light intensity transmitted through or reflected by the sample as a function of the wavelength. It can be done both in transmission mode, in which the detector receives the light transmitted through the sample and provides a direct value of absorption by the sample, or in reflectance mode, where it is possible to obtain an estimation of the absorption amplitude $F(R_\infty)$. Reflectance mode can be applied to solid samples, where the transmission signal is strongly attenuated.

In transmission mode, the transmitted light intensity I can be related to the incident intensity I_0 through the Beer-Lambert's law, in which $\mu(E)$ is the absorption coefficient and x represents the sample optical path:

$$I = I_0 e^{-\mu(E)x} \tag{2.30}$$

Furthermore, the absorption coefficient can be related to the molar absorptivity coefficient $\kappa(E)$ and the molar coefficient C through $\mu(E) = \kappa(E)C$. Lastly, the spectra are usually measured by the absorbance, defined by $A = \ln I_0/I$, as a function of the wavelength of the incident beam.

Standard spectrophotometer equipment used for UV-Vis measurements is composed of three distinct parts: light source, monochromator and detector. The light source is composed of two different lamps: a deuterium lamp that generates the UV part of the spectrum and a tungsten halogen one used for the visible part of the spectrum. The monochromator uses diffraction gratings that select a narrow (ideally unique) wavelength. Moreover, the spectrum must be measured before sample introduction in order to subtract several internal factors (blank measurement) such as background intensity of the solvent if the sample is diluted, black body emission of the lamps, grating efficiency and detector sensibility factors. Figure 21 illustrates a spectrophotometer configured for measurements in transmission mode.

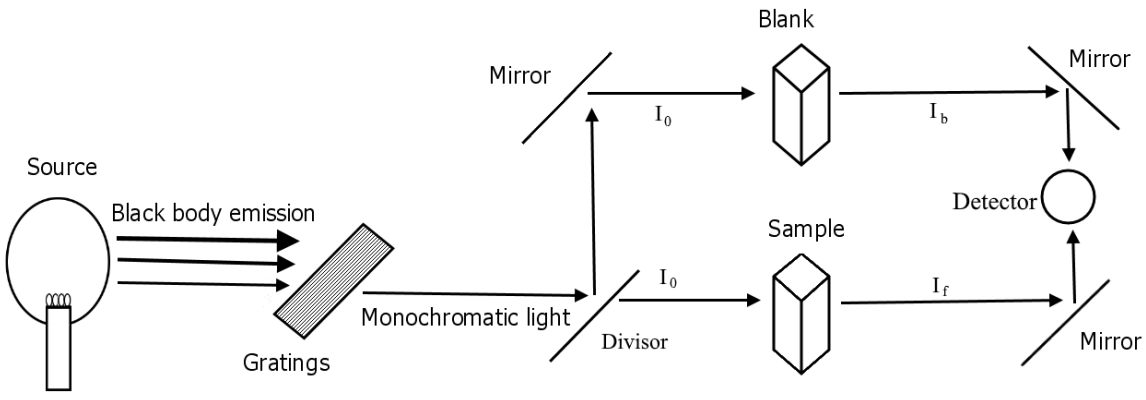

Figure 21 – Representation of a UV-vis spectrophotometer operating in transmission mode.

2.6 X-Ray Photoelectron Spectroscopy

X-Ray Photoelectron Spectroscopy (XPS) is a standard technique used for the characterization of materials surface [11, 102] and allows obtaining information about the chemical composition. This technique is based on the photoelectric effect, first explained by Einstein in his paper about the quanta of light [103], with which he won the Nobel prize in 1921. In an XPS experiment, a monochromatic X-ray beam is focused on the sample and presents a probability of ionizing the atoms. Then, ejecting photoelectrons. The photoelectrons emitted from the sample surface can be detected by an analyzer. Thus, providing a count of photoelectrons as a function of the kinetic energy of the photoelectron. A typical spectrum of Ni nanoparticles is shown in Figure 22 (a).

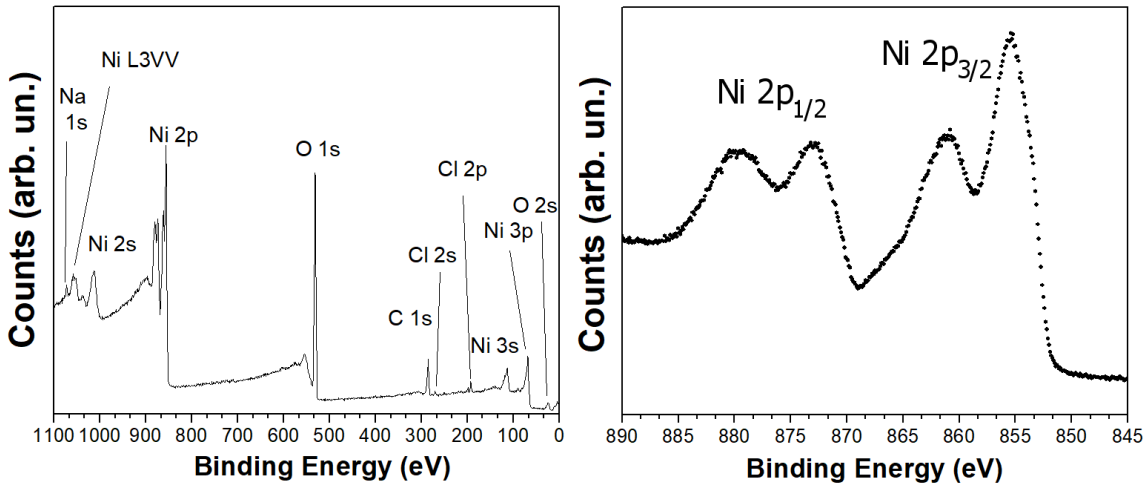

Figure 22 – XPS spectrum measurements of Ni nanoparticles in (a) long scan and (b) Ni 2p electronic region.

The kinetic photoelectron energy, K, can be related to the incident X-ray energy, $h\nu$, by the following equation:

$$K = h\nu - E_b - \phi_w \tag{2.31}$$

where E_b is the binding energy of the electron in a certain electronic level concerning the Fermi level and ϕ_w is the sample work function. The work function represents the additional energy needed for the ejection of a photoelectron to the vacuum level. The experiment setup makes that both the analyzer, which has its own work function (ϕ_a) and the sample are grounded. It implies that both Fermi levels become aligned, as shown schematically in Figure 23. As a consequence, there is the creation of an accelerating potential for the photoelectrons given by $\phi_w - \phi_a$, and

summing this offset to the kinetic energy equation above results in:

$$K = h\nu - E_b - \phi_a \tag{2.32}$$

Since the photon energy and analyzer work function are known, the measurement of the kinetic energy of the photoelectron enables the determination of the binding energy of the original electronic level, which is sensitive to the chemical environment around the atom. Thus, the determination of the binding energy gives the elemental composition and chemical components present at the surface of the sample.

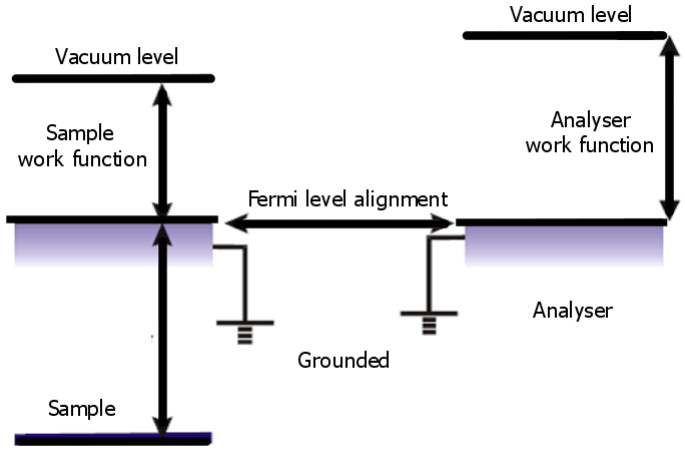

Figure 23 – Representation of the energy levels alignment between the sample and the analyzer.

The inelastic mean free path is the mean distance traveled by the photoelectron before suffering an inelastic collision. The XPS technique is surface-sensitive because the inelastic mean free path of photoelectrons is around tens of Å for the kinetic energies typically used in XPS. It means photoelectrons emitted from deeper regions are also leaving the surface, but most of these photoelectrons lose energy in the sample and are not considered in the XPS analysis. Figure 24 shows the universal curve that correlates the inelastic mean free path to the kinetic energy of the photoelectrons for different materials. It is possible to observe the same trend for all materials, there is not a strong dependence of the inelastic mean free path with the solid studied.

An arbitrary core hole can be created at the atomic level n, which has an orbital angular momentum l and a spin s. In XPS, this energy level can be characterized by the nl_J notation, where J is the total orbital momentum. The spin-orbit coupling generates a separation of the nl energy level, which value depends on the atomic species. As an example, a 2p state presents the $2p_{3/2}$ and $2p_{1/2}$ components, as observed in the Ni 2p XPS spectrum of Figure 22 (b).

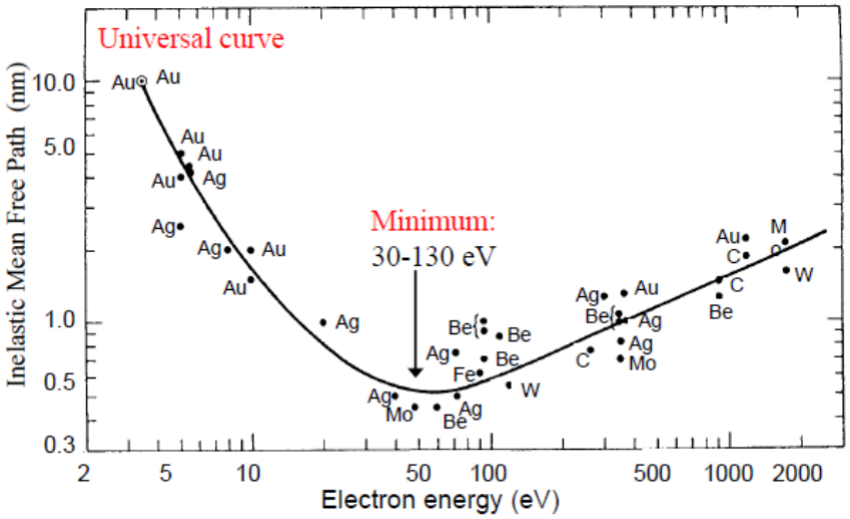

Figure 24 – Inelastic mean free path of photoelectrons generated as a function of the photoelectron kinetic energy. The points represent the experimental measurement and the solid line represents the universal curve. Adapted from [104].

The probability for the ejection of a photoelectron after the incidence of X-rays is determined by the differential cross section of the event, and it depends on the excitation energy [105]. Within the framework of quantum mechanics, the Hamiltonian describing the system of the electrons in an atom with a quantized electromagnetic field is given by $\hat{H} = \hat{H}_{atomic} + \hat{H}_{EM} + \hat{H}'$. The interaction Hamiltonian of the electromagnetic wave associated with the incident beam with the atomic electron in first order perturbation theory reads as:

$$\hat{H}' = \frac{e}{m_e c}\left(\hat{\mathbf{p}} \cdot \hat{\mathbf{A}}\right) + \frac{e}{2m_e c}\left(\boldsymbol{\sigma} \cdot \nabla \times \hat{\mathbf{A}}\right) \tag{2.33}$$

where m_e is the electron mass, $\hat{\mathbf{p}}$ is the linear momentum operator of the electrons, $\boldsymbol{\sigma}$ the electron spin and $\hat{\mathbf{A}}$ the vector potential operator of the electromagnetic field given by

$$\mathbf{A}(\mathbf{r}) \propto \sum_{\mathbf{k},\zeta} \boldsymbol{\epsilon}_{\mathbf{k},\zeta}(b_{\mathbf{k},\zeta} e^{i\mathbf{kr}} + b^{\dagger}_{\mathbf{k},\zeta} e^{-i\mathbf{kr}}) \tag{2.34}$$

where $\boldsymbol{\epsilon}$ is the polarization vector, $b_{\mathbf{k},\zeta}$ ($b^{\dagger}_{\mathbf{k},\zeta}$) is the photon annihilation (creator) operator in second quantization and the sum goes through all the possible wavevectors $\mathbf{k}$ and polarization ζ numbers.

The electronic state can be characterized by the ground state of the N electron system $|\Psi_k^N\rangle \approx |\Psi_k^{N-1}\rangle \otimes |\phi_k\rangle$, a composition of the single-electron state $|\phi_k\rangle$ and the $(N-1)$ passive electrons state. For the initial state in an absorption process, $|\phi_i\rangle$ represents the bound core electron, while the final state $|\phi_f\rangle$ is given by the free photoelectron. XPS is a one-photon

transition process and the transition operator M_{fi} can be generally obtained using the Lippmann-Schwinger equation, which relates M_{fi} to the interaction Hamiltonian $\hat{H}'$ and must be solved in an iterative way:

$$M_{fi} = H' + H' \frac{M_{fi}}{E_i - H + i\Gamma} \tag{2.35}$$

where Γ represents the lifetime broadening parameter of the excited state. H', in first order approximation, can describe a photon absorption process (one-photon transitions in general), so that $M_{fi}^{(1)} = H'^{(1)}$. Dropping the notation from $|\phi_k\rangle$ to $|k\rangle$, and considering the internal product $\left\langle \Psi_i^{N-1} | \Psi_f^{N-1} \right\rangle \approx 1$, the matrix element between the initial and the final state is given by inserting the vector potential into $H'^{(1)}$:

$$M_{fi} \propto \sum_f \left\langle f \left| \sum_{\mathbf{k},\zeta} \frac{e}{m_e c} b_{\mathbf{k},\zeta} \left[(\boldsymbol{\epsilon}_{\mathbf{k},\zeta} \cdot \mathbf{p}) e^{i\mathbf{kr}} + \frac{\hbar}{2} (\boldsymbol{\epsilon}_{\mathbf{k},\zeta} \cdot \boldsymbol{\sigma} \times \mathbf{k}) e^{i\mathbf{kr}} \right] \right| i \right\rangle \tag{2.36}$$

Then, by disregarding the relativistic effects carried by the spin operator and expanding the exponential with a Taylor expansion $e^{i\mathbf{kr}} \approx 1 + i\mathbf{kr} + \ldots$ until first order, which is known as the electric dipole approximation, it is possible to obtain the transition operator:

$$M_{fi} \propto \sum_f \left\langle f \left| \sum_{\mathbf{k},\zeta} \frac{e}{m_e c} b_{\mathbf{k},\zeta} (\boldsymbol{\epsilon}_{\mathbf{k},\zeta} \cdot \hat{\mathbf{p}}_i) \right| i \right\rangle \tag{2.37}$$

The electric dipole approximation is valid for an X-ray wavelength much higher than the typical dimensions of the system, in this case, the atom. The transition rate W_{fi} between the initial state with energy E_i and final state with E_f by the excitation of a photon with energy $h\nu$ can then be determined as:

$$W_{fi} \propto \frac{2\pi}{\hbar} |M_{fi}|^2 \delta(E_f - E_i - h\nu) \tag{2.38}$$

This is known as Fermi's golden rule. As a consequence, the dipole selection rules derived from Fermi's golden rule are given by the conditions for the azimuthal, magnetic and spin quantum numbers:

$$\Delta l = \pm 1 \quad \Delta m = 0, \pm 1 \quad \Delta s = 0 \tag{2.39}$$

It means the electronic transitions that are not characterized by changes in the quantum numbers given by these equations are not allowed in the dipole approximation. The differential cross section $\frac{d\sigma}{d\Omega}$ of photoionization of the nl atomic level is defined as:

$$\sigma_{nl}(h\nu) = \oint \frac{d\sigma_{nl}}{d\Omega}(h\nu)d\Omega \tag{2.40}$$

where σ is the absorption cross section and it comes from Fermi's golden rule. By using time-dependent perturbation theory, the photoionization differential cross section of a specific energy level for a linearly polarized incident beam can be encountered as:

$$\frac{d\sigma_{nl}}{d\Omega}(h\nu) = \frac{\sigma_{nl}(h\nu)}{4\pi}\left[1 + \beta_{nl}(h\nu)\left(\frac{3}{2}\cos^2\phi - \frac{1}{2}\right)\right] \tag{2.41}$$

$-1 \leq \beta_{nl} \leq 2$ is the asymmetry parameter, which originates due to the anisotropic effects of photoemission concerning the interaction with the atomic environment and ϕ is the angle between the polarization of the incident beam and the photoemission direction. Then, the XPS intensity measured can be calculated by:

$$I_{nl} = \frac{d\sigma_{nl}}{d\Omega}(h\nu)D(K)J\int_0^\infty \rho(z)e^{-z/[\lambda_{\text{IMFP}}(K)cos\theta]}dz \tag{2.42}$$

The term D stands for the efficiency of the analyzer at kinetic energy K, J represents the incident photon flux, z is the sample depth, ρ is the atomic density per volume, λ_{IMFP} the inelastic mean free path at kinetic energy K and θ is the angle between the surface's normal and the photoemission's direction.

After the photoelectron ejection, the original atomic shell will be refilled by an outermost electron. This process can either emit another photon, in a process called fluorescence, or another electron, which is dubbed Auger electron [106]. Both effects are illustrated in Figure 25. The fluorescence or Auger process will lead to the creation of other respective core holes, generating a cascade effect of hole refilling and particle emission. Auger electrons appear frequently in XPS spectra, as shown in the long scan spectrum of Figure 22. The Auger electrons receive a specific notation with three letters, in which the first letter corresponds to the initial core hole shell, the middle letter to the initial shell of the relaxing electron and the final letter to the initial shell of the Auger electron. The Auger signal differs from the typical photoelectrons because the Auger electron kinetic energy does not depend on the excitation energy. It means that, by varying the excitation energy, the Auger component remains with the same kinetic energy, differently of photoelectrons that change the kinetic energy in accordance to equation 2.32. Alongside Auger

and photoelectron components, satellites due to different photoelectron interaction effects such as shake up, shake off, plasmons and multiplet splitting can appear in the XPS spectrum. In special, shake-up satellites appear due to the excitation of a valence electron of the excited atom to a higher energy level, reducing the kinetic energy of the detected photoelectron and producing a smaller shifted component in the XPS spectrum. Nonetheless, shake-off satellites result from the ejection of a valence electron of the excited atom due to the photoelectron excitation during ejection.

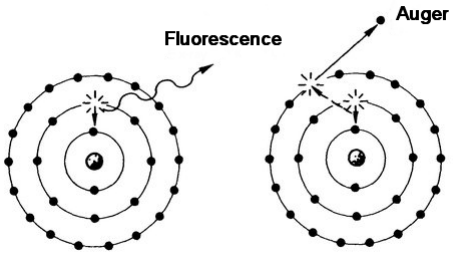

Figure 25 – Illustration of Auger and fluorescence relaxation mechanisms. Adapted from [107].

Laboratory conventional XPS systems commonly use radiation from Mg Kα (1253.7 eV) and Al Kα (1486.7 eV) X-ray sources, but in a synchrotron facility, this excitation energy can be tuned within a certain range that depends on the beamline configuration. The hemispherical analyzer, illustrated in Figure 26, consists of two concentric metallic hemispheres with different electrical potentials. The electric field generated in this region selects photoelectrons that reach the multi-channel detector with specific kinetic energy by using the effect of the electric force. Then, only photoelectrons with a given specific kinetic energy are able to reach the multi-channel detector (which is coupled to a photomultiplier) after entering the hemisphere region. The choice of the photoelectron kinetic energy detected is made by applying a potential before the hemisphere region, then selecting those photoelectrons with a specific kinetic energy. The energy that enables the photoelectron to reach the detector is named pass energy. This mode of operation is known as the Constant Analyzer Energy (CAE) mode. The conventional setup needs ultra-high vacuum ($< 1.10^{-8}$ mbar) to avoid the electron scattering by gas molecules after leaving the sample, surface contamination during the measurements, and to avoid the photoelectron spectrometer from burning out. Nowadays, Near Ambient Pressure XPS (NAP-XPS) experiments are available, where the sample is subjected to high temperatures and pressures of gas during the XPS measurements [108].

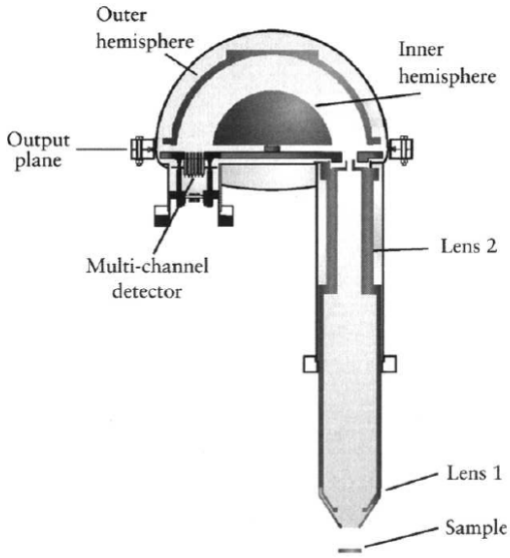

Figure 26 – Illustration of the analyzer used in XPS measurements. Adapted from [102].

2.7 X-Ray Absorption Spectrocospy

X-Ray Absorption Spectroscopy (XAS) is a technique used for probing the local structure and the electronic configuration around the atom that absorbs X-rays [11, 106, 109, 110]. It consists of the measurement of the sample's X-ray absorption coefficient as a function of the incident X-ray energy. The sample does not need to be crystalline, because only the local configuration around the absorbing atom is probed. XAS measurements can be done both in situ (high temperature and pressure of gases) and time-resolved, providing important data about the changes of the material structure during a catalytic reaction, for example. The absorption coefficient can be obtained from Beer-Lambert's law (equation 2.30) by measuring the incident and transmitted intensities.

Figure 27 (a) shows an example of an XAS spectrum at Ni K edge of Ni nanoparticles. The Ni K edge refers to an electronic transition from the 1s to 4p electronic level of Ni. For photon energies smaller than the binding energy of the electron at the Ni 1s electronic level, the absorption coefficient is null. When the photon energy is around the value of the binding energy, there is an abrupt increase in the absorption coefficient. This region is named the absorption edge. The visible oscillations of the absorption coefficient after the absorption edge characterize the X-ray Absorption Fine Structure (XAFS). When the X-ray photons are absorbed by a core electron, the emitted photoelectron can be viewed as a spherical wave that travels through the neighboring atoms and can be backscattered by their atomic potential, as illustrated in Figure

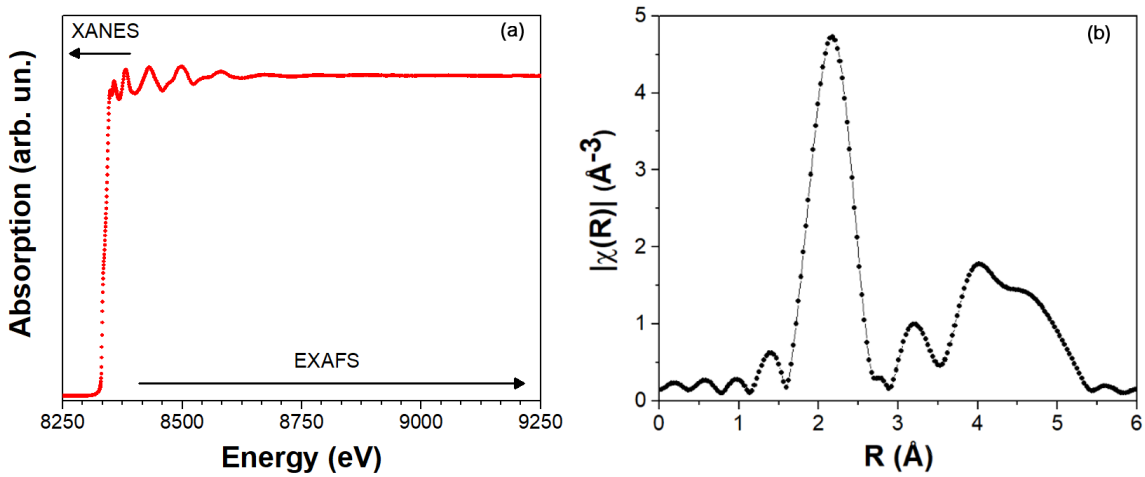

Figure 27 – (a) XAS spectrum of Ni nanoparticles at the Ni K edge and (b) the Fourier transform of the EXAFS oscillations.

28. It shows the interference between the emitted and backscattered photoelectrons that results in either constructive or destructive patterns. This interference dictates the XAFS oscillations, where a constructive interference increases the absorption coefficient while the destructive one decreases it. Furthermore, the XAS measurement is divided into two different energy regions. The X-Ray Absorption Near-Edge Spectroscopy (XANES) region is characterized by the oscillations contained approximately between 30 eV before the absorption edge until 50 eV after it, and it provides information about the oxidation state of the absorbing atom and the local atomic geometry. The Extended X-ray Absorption Fine Structure (EXAFS) region begins after the XANES region until the end of the XAS spectrum (typically 1 keV). The analysis of this region gives relevant information about the distance between first neighbors, the coordination number and the thermal disorder.

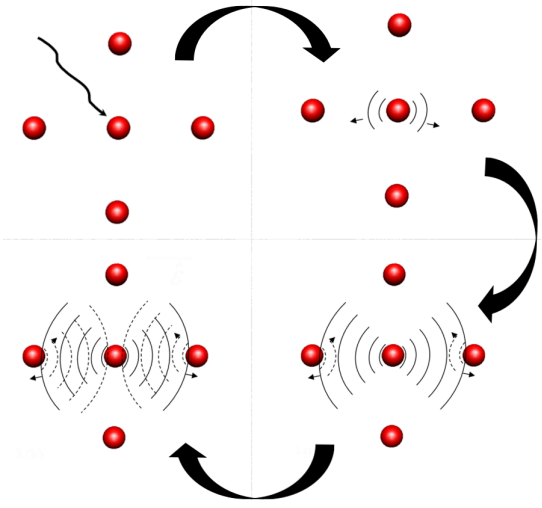

Figure 28 – Representation of the photoelectron backscattering in the first neighbors.

The XAS spectra of some elements, specially for the K edge of transition metals, can show an increase in absorption coefficient in the pre-edge region, not explained by transition dipole rules. Then, a higher order multipole transition rule can be used. Pre-edge regions are strongly determined by the local geometry. They depend as well on the hybridization of the molecular bonding, which can be interpreted by Crystalline Field Theory. By obtaining irreducible representations of the point groups in group theory, which are linked to the symmetries of the system, it is possible to analyze these structures.

Modern ab initio softwares such as FEFF [111, 112] use multiple-scattering theory to solve a quasi-particle Green's function [113, 114, 115, 116], where a Feynman diagram of the core-hole excitation in represented in Figure 29.

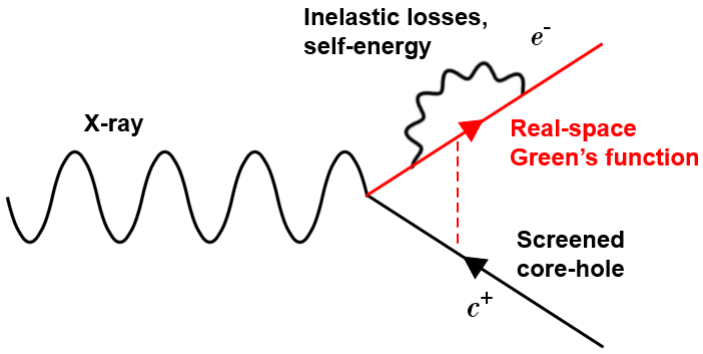

Figure 29 – Representation of the interaction absorption process by a Feynman diagram.

A limitation of this quasi-particle implementation is the general disregard of multiplets and satellites. It considers a flat interstitial potential $\hat{V}_{int}$ and scattering site potentials (atoms) as perturbations $\hat{V}$.

$$\hat{H}_{sct} = \hat{H}_0 + \hat{V}_{int} + \hat{V} \tag{2.43}$$

where $\hat{H}_0$ represents the single particle Hamiltonian. It is possible to use the one-particle Green's function, which has the same eingenfunctions as the solutions to its respective Schrödinger's equation and the eigenvalues of this solution are the poles of $\hat{G}$. If the wavefunction represents the probability amplitude to find an electron in a point $\mathbf{r}$, Green's functions represent the propagation of this amplitude from $\mathbf{r}$ to $\mathbf{r}'$. As $E = E_i + \hbar\omega$, the term $\hat{G}$ reads as:

$$\hat{G}(E) = \frac{1}{E - \hat{H} + i\Gamma}, \quad \hat{G}^0(E) = \frac{1}{E - \hat{H}_0 + i\Gamma} \tag{2.44}$$

where the free-electron propagator $\hat{G}^0$ represents the propagation of an outgoing wave. Furthermore, the full-electron propagator can be written in the spacial coordinates form:

$$\hat{G}(\mathbf{r}, \mathbf{r}_f, E) = \sum_f \langle \mathbf{r}_f | f \rangle \, G(E_f) \, \langle f | \mathbf{r} \rangle \tag{2.45}$$

By the use of the commutation relationship, $m_e[\mathbf{r}, \hat{H}_0] = i\hbar\mathbf{p}$, and defining the polarization vector $\boldsymbol{\epsilon}$ in $\mathbf{A} = \boldsymbol{\epsilon}(2\pi\hbar c^2 u/\omega)^{1/2} e^{i\mathbf{q}\cdot\mathbf{r}}$, where u is the photon density number and $\mathbf{q}$ the photon momentum, Fermi's golden rule for the dipole approximation of a photon absorption by the atom can be written as:

$$\mu(E) \propto \sum_f^{E_f > E_{\text{Fermi}}} |\langle f \, | \boldsymbol{\epsilon} \cdot \mathbf{r} | \, i \rangle|^2 \propto -\frac{1}{\pi} \text{Im} \left\langle i \left| (\boldsymbol{\epsilon}^* \cdot \mathbf{r}) \; \hat{G}(\mathbf{r}, \mathbf{r}_f, E) \; (\boldsymbol{\epsilon} \cdot \mathbf{r}) \right| i \right\rangle \Theta_\Gamma(E - E_{\text{Fermi}}) \tag{2.46}$$

where Θ_Γ is the step-function broadened by the lifetime of the core-hole. The full one-electron propagator in the presence of the scattering potential $\hat{G}$ can be expressed in a Dyson equation structure between the free-electron propagator and the transition operator, titled the full atomic scattering matrix, $\hat{\Upsilon}$, by the identity $\hat{V}\hat{G} = \hat{\Upsilon}\hat{G}_0$:

$$\hat{G} = \hat{G}^0 + \hat{G}^0 \hat{\Upsilon} \hat{G}, \quad \hat{\Upsilon} = \hat{V} + \hat{V}\hat{G}\hat{V} \tag{2.47}$$

A very simple approximation to the complex atomic scattering interactions is the use of a muffin-tin potential (illustrated in Figure 30), which is centered around the atoms and has a spherical shape. This potential can lead to good estimations for the EXAFS region of the spectrum because the high kinetic energy photoelectrons are scattered mainly by the internal part of the real scattering potential and travel almost freely in the interstitial region. Of course, using such a simple spherical potential comes with limitations: near the absorption edges, the theory loses accuracy because it corresponds to low kinetic energy electrons, which are more sensitive to the details of the potential in the interstitial region. Consequently, this approximation is not suitable for the XANES region. Expanding $\hat{V} = \sum_{n \neq c} \hat{V}_n$ as the sum between n (n different than the ionized atom) single site scattering operators $\hat{t}_n$:

$$\hat{G}_n = \hat{G}^0 + \hat{G}^0 \hat{t}_n \hat{G}^0 \Rightarrow \hat{t}_n = \hat{V}_n + \hat{V}_n \hat{G}^0 \hat{t}_n \tag{2.48}$$

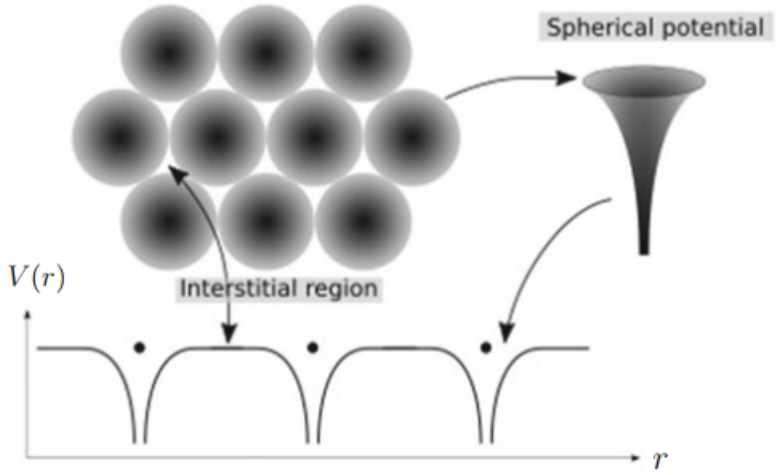

Figure 30 – Schematic representation of a muffin-tin potential. Adapted from [115].

Contrarily to the potentials, it is important to notice that the $\hat{t}_n$ terms do not simply add to form the full scattering matrix. Instead, $\hat{\Upsilon}$ should be expressed by taking into account the effect of all atoms:

$$\hat{\Upsilon} = \sum_{n \neq c} \left[\hat{V}_n + \hat{V}_n \hat{G} \sum_{m \neq c} \hat{V}_m \right] \tag{2.49}$$

It is possible then to expand the full scattering operator as:

$$\hat{\Upsilon} = \sum_{n \neq c} \hat{t}_n + \sum_{n \neq c} \hat{t}_n \, \hat{G}^0 \sum_{m \neq n,c} \hat{t}_m + \sum_{n \neq c} \hat{t}_n \, \hat{G}^0 \sum_{m \neq n} \hat{t}_m \hat{G}^0 \sum_{k \neq n,m,c} \hat{t}_k + \dots$$

The sums exclude the possibility of an initial scattering by the central atom or from the sequential scattering by the same atom. The propagator can be rearranged into a Born expansion structure [114]:

$$\begin{aligned} \hat{G} = \hat{G}^0 + \hat{G}^0 \sum_{n \neq c} \hat{t}_n \hat{G}^0 + \hat{G}^0 \sum_{n \neq c} \hat{t}_n \, \hat{G}^0 \sum_{m \neq n,c} \hat{t}_m \hat{G}^0 + \\ + \hat{G}^0 \sum_{n \neq c} \hat{t}_n \, \hat{G}^0 \sum_{m \neq n} \hat{t}_m \, \hat{G}^0 \sum_{k \neq n,m,c} \hat{t}_k \, \hat{G}^0 + \dots = \hat{G}^0 + \hat{G}^0 \hat{\Upsilon} \hat{G}^0 + \hat{G}^0 \hat{\Upsilon} \hat{G}^0 \hat{\Upsilon} \hat{G}^0 \dots \end{aligned} \tag{2.50}$$

By defining the central atom contribution $\hat{G}_c = \hat{G}^0 + \hat{G}^0 \hat{t}_c \hat{G}^0$, the EXAFS propagator can be expanded to different order contributions, in which some examples are represented graphically in Figure 31. Expanding $\hat{G}$ in terms of the central atom propagator, the single site scattering operator defines the EXAFS contribution:

$$\hat{G} = \hat{G}_c + \hat{G}_c \sum_{n \neq c} \hat{t}_n \hat{G}_c + \hat{G}_c \sum_{n \neq c} \hat{t}_n \hat{G}_c \sum_{m \neq n,c} \hat{t}_m \hat{G}_c \dots \tag{2.51}$$

The XANES contribution instead depends on the full scattering operator given by the expanded Dyson equation (2.50), and its solution, though not as simple to expand similarly to EXAFS can be found as:

$$\hat{G} = \left(1 - \hat{G}^0 \hat{\Upsilon}\right)^{-1} \hat{G}^0 \tag{2.52}$$

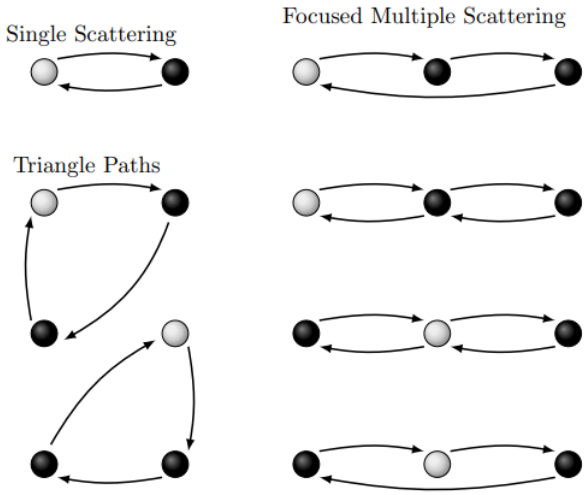

Figure 31 – Representation of different order scattering paths, where spheres with different colors represent different atomic species. Adapted from [117].

The reason why the difficulty to obtain a derived XANES equation is not only characterized by the impossibility of using a simple potential such as muffin-tin but that the excitation of the electrons to unoccupied electronic states contributes to the spectrum as well. In this way, a possible method to calculate XANES spectra relies on more precise types of electronic state computations such as Density Functional Theory. Using the derived EXAFS scattering propagator expansion, the absorption coefficient can be approximated as the following:

$$\mu \propto -\mathrm{Im}\left\langle i \left| \boldsymbol{\epsilon} \cdot \mathbf{r}\, \hat{G}_c\, \boldsymbol{\epsilon} \cdot \mathbf{r} \right| i \right\rangle - \sum_{n \neq c} \mathrm{Im}\left\langle i \left| \boldsymbol{\epsilon} \cdot \mathbf{r}\, \hat{G}_c \hat{t}_n \hat{G}_c\, \boldsymbol{\epsilon} \cdot \mathbf{r} \right| i \right\rangle + \ldots \tag{2.53}$$

The first term is proportional to the absorption coefficient of the free atom, μ_0, while the higher terms are related to the scattering of the photoelectron due to the surrounding atoms. The second term gives the single-scattering contribution to the signal from the n'th scattering site. The "EXAFS" oscillations are defined as the modulation of the atomic absorption coefficient [118]:

$$\chi = \frac{\mu - \mu_0}{\Delta\mu_0} \tag{2.54}$$

where $\Delta\mu_0$ is the change of μ at the absorption edge, and μ_0 represents the absorption coefficient of an isolated atom (without EXAFS oscillations). Restricting to first order (single-scattering) terms, the EXAFS oscillations can be approximated as:

$$\chi \approx \sum_n \chi_n \tag{2.55}$$

that is to say, the sum of the individual single-scattering sites. The EXAFS oscillations in the spectrum can be developed by considering different scattering shells centered around the central atom. This equation then evaluates χ as a function of the photoelectron wavevector k, given as:

$$k = \sqrt{\frac{2m_e}{\hbar^2}K}, \quad K = \hbar\omega - E_b \tag{2.56}$$

The E_b value is the binding energy of the electron in the core level of the system ground state and K is the kinetic energy of the photoelectron. Thus, by applying a summation through the different scattering shells j, the EXAFS oscillations reads as:

$$\chi(k) = \sum_j \frac{S_0^2}{k}\frac{N_j}{R_j^2} e^{-2k^2\sigma_j^2} e^{-\frac{2R_j}{\lambda_\tau(k)}} f_j(k,\Theta)\sin\left(2R_j k + \Phi_j(k)\right) \tag{2.57}$$

The EXAFS oscillations represent a sum over all possible atomic configurations. S_0^2 is a scattering amplitude correction that considers inelastic losses that reduce the scattering amplitude such as shake-up and shake-off processes. Theoretically, it depends on the photoelectron kinetic energy, but it turns out that in the EXAFS region this energy dependence can be neglected. It is important to point out that S_0^2 depends mostly on the atomic species of the absorbing atom, thus being transferable up to a certain degree in similar atomic environments during the analysis. N_j is the coordination number of the j-th shell. R_j is the distance from the absorbing atom to the scattering atom in the j-th shell, and the EXAFS dependence on the R_j^{-2} depicts the spherical wave propagation character of the photoelectron. σ_j is the Debye-Waller factor that represents the deviation in the distance between the central atom and the scattering atoms by thermal and structural disorder effects. Traditionally, anharmonic correlated Einstein and correlated Debye models are used in order to simulate the Debye-Waller factor [119]. λ_τ represents the mean distance covered by the photoelectron in the material, which depends on the inelastic mean free path of the photoelectron (result of inelastic losses, plasmon excitation and other possible effects) and of the finite lifetime of the core-hole. f_j is the scattering amplitude at an angle Θ and it depends on the photoelectron kinetic energy. The $2R_j$ term inside the sine and exponential

arguments indicates that the photoelectron travels a closed path between the central and the scattering atoms to produce an interference pattern. Lastly, Φ_j is the phase shift of the wave due to the scattering process.

The EXAFS analysis is actually done by making the Fourier Transform (FT) of the EXAFS oscillations (as shown in Figure 27 (b)) and fitting some parameters to different scattering paths that can be calculated from a given initial structure (*ab initio* calculation) by software such as FEFF [120]. The Fourier Transform is analyzed by proposing an atomic cluster and then calculating the $f_j(k, \theta)$ and Φ_j factors, using the muffin-tin potential. Then, parameters such as the coordination number, Debye-Waller factor and distance between the absorbing and neighbor atom are allowed to vary in the fitting. The FT $\chi(R)$ can then be adjusted by minimizing statistically dependent variables such as the R factor.

Unlike EXAFS, the XANES region is usually analyzed by obtaining standard spectra of reference materials in the same edge and using a linear combination of them to fit the sample spectrum. This type of regression is known as Linear Combination Analysis (LCA) and it allows obtaining a weight for each component. It is important to notice that the fitting result essentially depends on the reference materials used (availability of the material). Another possible type of analysis is dimensionality reduction, specifically Principal Component Analysis (PCA). This type of analysis does not rely on the guess of a component, as the algorithm would select linear combinations of basis spectra and produce new sets of basis vectors that minimize the number of basis vectors needed to fit the spectra. A limitation to this kind of approach is that the new sets of basis vectors may not provide physical interpretation to the data.

There are different detection modes of an XAS spectrum but the transmission mode is the most common one. In this case, the intensities of the incident and transmitted beam are measured with ionization chambers. They are composed of two electrodes and the excitable gas, which can be of Ar for measurements in incident energies higher than around 10 keV, N_2 for energies between 5 keV and 10 keV or He for lower energies. The electrodes collect the charges created after the X-ray ionizes the gas. Thus, producing a current proportional to the beam intensity.

2.8 Ion Irradiation

The modification of the solid properties by ion irradiation is an interesting aspect of materials science. The creation of O vacancies, defects and other possible processes induced

by the ion beam can affect the electronic structure of catalysts. In the collision of heavy ions with a material, there is the occurrence of energy transfer between the ions and the atoms of the matrix [121, 122]. The process can happen through collisions with the electronic cloud or with the nuclei of the system. The stopping power, $S(E)$, of a collision can be used to estimate the energy loss of the incident ion. It can be independently divided between the interaction of the electron cloud with the incident ions (electronic stopping power $S_e(E)$) and the interaction of the atomic nuclei with the incident ions (nuclear stopping power $S_n(E)$). As the projectile energy is a function of the penetration depth ($E = E(x)$), the total stopping power is defined as:

$$S(E) = S_e(E) + S_n(E) = -\frac{1}{N}\frac{dE}{dx_e} - \frac{1}{N}\frac{dE}{dx_n} \tag{2.58}$$

where x is the path length of the ion and N is the volume density of the target. The electronic stopping power is characterized by inelastic collisions, where the ion excites the electrons to higher energy levels. This term dominates for high ion energies of a few hundred MeV. If the ion is heavy and the target is dense (like Au^{+7} and $SrTiO_3$), then the nuclear stopping power may dominate as well for lower energies. The Bethe-Bloch equation relates the electronic stopping power with the ion velocity v:

$$S_e(v) = \frac{4\pi C^2 e^4}{m_e v^2} \ln\left(\frac{2m_e v^2}{I}\right) \tag{2.59}$$

where C is the charge of the ion, I the mean excitation potential of the target and m_e the electron mass.

The nuclear stopping power is characterized by elastic collisions, where the incident ions cause the displacement of the atoms in the matrix, which can create defects and atomic vacancies. It depends on the Coulomb repulsion between the nuclear charges of the atoms. Screened semi-empirical potentials can describe the nuclear repulsion between the ions and the nuclei. The ZBL potential is derived from the Rutherford elastic scattering and it has a screening function term ϕ that alters the Coulomb potential, where Z represents the atomic number:

$$V_{ZBL}(r) = \frac{CZe^2}{4\pi\epsilon_0 r}\phi\left(\frac{r}{a}\right) \tag{2.60}$$

After an atomic collision, a collision cascade effect may happen, where interstitial atoms and cavities are created by the process. In a first approximation, the range of the ion can be

calculated by the integration of the equation above:

$$R = \int_0^{E_0} \frac{dE}{NS(E)} \tag{2.61}$$

where E_0 stands for the initial ion energy. This result is only valid when the ion straggling becomes negligible, also called the Continuous Slowing Down Approximation (CSDA). For small fluctuations of the range, the straggling parameter, $W(E)$, can be used to calculate the fluctuation of the total range Ω_R^2:

$$\Omega_R^2 = \int_0^{E_0} \frac{NW(E)dE}{[NS(E)]^3} \tag{2.62}$$

The ion range profile can be simulated with the SRIM (Stopping and Range of Ions in Matter) package [123], where the TRIM (Transport of Ions in Matter) core program implements most of the calculations. It uses a Monte Carlo method to estimate the energy losses, number of atomic displacements per atom and the possible number of vacancies created by the ions. The simulation assumes a series of binary scattering events of the ions by an atomic potential, where the particle travels freely in the interstice (free-fly-path) and the target is amorphous. When the ion energy drops below a given value or the ion leaves the target, the simulation of this particle is terminated, and the next ion is inserted. The free-flight-path enables the simulation of heavier ions. One of the most important approximations in TRIM is called the Magic Formula, which describes the atom-atom scattering. This formula can be derived from the scattering triangle represented in Figure 32, and by expressing it by the screening length a, the Magic Formula reads as:

$$\cos\frac{\theta}{2} = \frac{B + R_c + \Delta}{R_0 + R_c}, \quad B = \frac{P}{a},\ R_0 = \frac{r_0}{a},\ R_c = \frac{\rho_1 + \rho_2}{a},\ \Delta = \frac{\delta_1 + \delta_2}{a} \tag{2.63}$$

Limitations include that SRIM does not conserve changes of the target material induced by the irradiation for the next iteration and collisions that transfer negligible amounts of energy and deflection angles in the ion trajectory are scaled together.

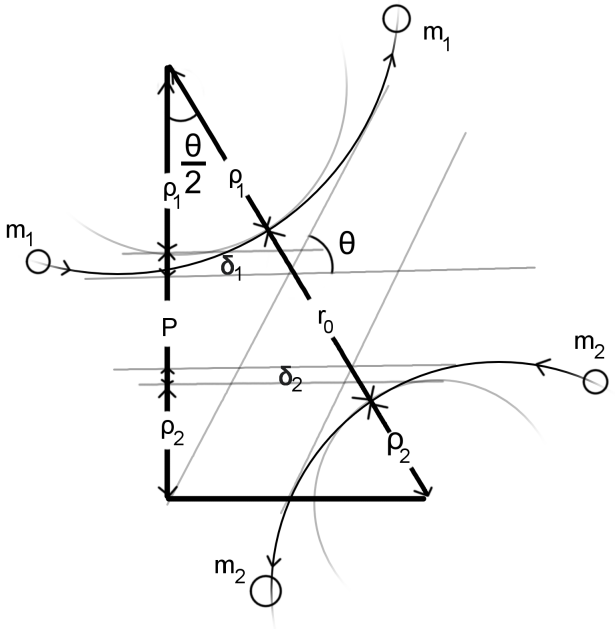

Figure 32 – Representation of the scattering particles at the center-of-mass frame. The scattering triangle is formed by considering the distance of closest approach r_0, the impact parameter P, radii of curvature ρ_i.

2.9 Density Functional Theory

The solution to the non-relativistic time-independent Schrödinger's equation (2.64) is the major challenge in most materials research fields, such as solid state, atomic and molecular physics. Since there is no analytical solution to almost any molecular or crystalline system, numerical and computational approaches are diversely applied to the study of such systems [124, 125, 126].

$$\hat{H}\Psi(\mathbf{x}_1,\ldots,\mathbf{x}_n,\mathbf{X}_1,\ldots,\mathbf{X}_N) = E_i\Psi(\mathbf{x}_1,\ldots,\mathbf{x}_n,\mathbf{X}_1,\ldots,\mathbf{X}_N) \tag{2.64}$$

The Hamiltonian of the above equation in an arbitrary system without external potentials, consisting of n electrons and N nuclei reads as:

$$\begin{aligned}\hat{H} = -\frac{\hbar^2}{2m_e}\sum_{i=1}^{n}\nabla_i^2 - \frac{\hbar^2}{2}\sum_{i=1}^{N}\frac{1}{M_i}\nabla_i^2 - \frac{e^2}{4\pi\epsilon_0}\sum_{i=1}^{n}\sum_{A=1}^{N}\frac{Z_A}{r_{iA}} + \\ + \frac{e^2}{4\pi\epsilon_0}\sum_{i=1}^{n}\sum_{j\neq i}^{n}\frac{1}{r_{ij}} + \frac{e^2}{4\pi\epsilon_0}\sum_{A=1}^{N}\sum_{B\neq A}^{N}\frac{Z_A Z_B}{r_{AB}}\end{aligned} \tag{2.65}$$

The first and second terms describe the kinetic energy of the electrons with mass m_e and each nucleus with atomic mass M_i, other terms describe the electrostatic potential of nuclei-

electron, electron-electron and nucleus-nucleus interaction, respectively. Z_A is the atomic number of each nucleus and r represents the relative distance between each element. The mass of a nucleus is more than a thousand times higher than the mass of an electron, such that the speeds of the electrons relative to the nuclei are much higher as well. Thus, there is the possibility of considering the electrons moving in a field of fixed nuclei, where the first term of (2.65) can be considered negligible and the last term a constant (E_N), known as the Born-Oppenheimer approximation. The Hamiltonian can then be organized as:

$$\hat{H} = \hat{H}_e + E_N = \left(\hat{T}_e + \hat{V}_{e,N} + \hat{V}_{e,e}\right) + E_N \tag{2.66}$$

$$\hat{H}_e \Psi_e = E_e \Psi_e \tag{2.67}$$

where the total energy reads as the sum of the electronic energy E_e and the nuclei energy E_N, and Ψ_e represents the electronic wave function. The variational principle states that the energy obtained from the use of a trial function Ψ_t is an upper bound for the ground state energy E_0. The minimization of $E[\Psi_t]$ concerning the n-electron wave functions gives the ground energy E_0.

$$E[\Psi_t] = \frac{\left\langle \Psi_t | \hat{H} | \Psi_t \right\rangle}{\langle \Psi_t | \Psi_t \rangle} \Longrightarrow E_0 = \min_{\Psi_t \to n} E[\Psi_t] \tag{2.68}$$

The theory that aims to solve Schrödinger's equation to obtain the wavefunctions of the Hamiltonian is the Wave Function Theory (WFT). The Hartree-Fock approximation, one of the most applied WTF methods, consists of supposing n-one-electron orthogonal wave functions, χ_i, with an anti-symmetric product given by the Slater determinant as a trial function for the variational principle:

$$\Psi_{HF} = \Psi(\mathbf{x}_1, \mathbf{x}_2, \ldots, \mathbf{x}_n) = \frac{1}{\sqrt{n!}} \begin{vmatrix} \chi_1(\mathbf{x}_1) & \chi_2(\mathbf{x}_1) & \ldots & \chi_n(\mathbf{x}_1) \\ \chi_1(\mathbf{x}_2) & \chi_2(\mathbf{x}_2) & \ldots & \chi_n(\mathbf{x}_2) \\ \vdots & \vdots & & \vdots \\ \chi_1(\mathbf{x}_n) & \chi_2(\mathbf{x}_n) & \ldots & \chi_n(\mathbf{x}_n) \end{vmatrix} \tag{2.69}$$

$$= \frac{1}{\sqrt{n!}} \sum_{j=1}^{n!} (-1)^{p_j} P_j \left\{ \chi_1(\mathbf{x}_1) \chi_2(\mathbf{x}_2) \ldots \chi_n(\mathbf{x}_n) \right\} \tag{2.70}$$

where $\chi_i(\mathbf{r}_i)$ is defined as the spin orbitals composed of the spatial orbital, $\phi_i(\mathbf{r}_i)$, and the spin function σ:

$$\chi_i(\mathbf{r}_i) = \phi_i(\mathbf{r}_i)\sigma \tag{2.71}$$

The Hartree-Fock approximation is widely used for obtaining ground states of the system. Nevertheless, it presents some issues. Although it can give a representation to electron exchange terms in the energy, it does not calculate how electrons influence each other. The correlation terms that can be viewed as the difference in energy between the exact solution and the Hartree-Fock solution are not treated (but it can be included in post-HF calculations). For a system with n-electrons, it scales with $3n$ variables, so that for bigger systems the computational effort is incredibly high. The ground state wave function is not an observable of the system so that a direct observable measurement cannot be made.

2.9.1 The electron density and Kohn-Sham equations

Considering the appointed issues for the HF approximation, there is the possibility to use an observable known as the electronic density, defined as:

$$\rho(\mathbf{r}) = n \int \int \dots \int |\Psi(\mathbf{x}_1, \mathbf{x}_2, \dots, \mathbf{x}_n)|^2 d\sigma_1 d\mathbf{x}_2 \dots d\mathbf{x}_n, \quad \begin{cases} \rho(\mathbf{r} \to 0) = 0 \\ \int \rho(\mathbf{r}) d\mathbf{x}_1 = n \end{cases} \tag{2.72}$$

where ρ represents the probability of finding one of the n electrons within the volume element $d\mathbf{x}_1$ with an arbitrary spin, while the other $n-1$ electrons can have any position and spin.

Hohenberg and Kohn [127] demonstrated two theorems that provide a basis for DFT and a reason for the use of electronic density. The first one can be read as "*the ground-state energy from Schrödinger's equation is an unique functional of the electron density*", and the second one as, "*the electron density that minimizes the energy of the overall functional is the true electron density corresponding to the full solution of the Schrödinger's equation*" [128]. The first theorem means that, since the external potential that describes the nuclei environment uniquely defines the wavefunction of the system, the wavefunction uniquely defines the electronic density in an injective mapping. Even if the density appears to be less information-rich in the first moment, the theorem states that it has a one-to-one mapping to the external potential, V_{ext}. Thus, the energy

functional can be solved as a function of the electronic density, and the ground state energy obtained from its minimization is:

$$E[\rho] = T_e[\rho] + E_{e,N}[\rho] + E_{e,e}[\rho] = F[\rho] + E_{e,N}[\rho] \tag{2.73}$$

$$E_{e,N} = \int \rho(\mathbf{r}) V_{ext} d\mathbf{r} \tag{2.74}$$

$$F[\rho] = T_e[\rho] + E_{e,e}[\rho] \tag{2.75}$$

Moreover, it is possible to split the electron-electron interaction potential as:

$$E_{e,e}[\rho] = \frac{e^2}{2} \int \int \frac{\rho(\mathbf{r})\rho(\mathbf{r}')}{|\mathbf{r} - \mathbf{r}'|} d\mathbf{r} d\mathbf{r}' + G[\rho] = J[\rho] + G[\rho] \tag{2.76}$$

where $J[\rho]$ represents the classical Coulomb interaction and $G[\rho]$ the non-classical terms, such as Coulomb corrections, exchange interactions and self-interaction. It can be noted that the complexity of DFT is difficult to correctly and explicitly find the forms of $T_e[\rho]$ and $G[\rho]$. If there was a way to obtain these two functionals, Schrödinger's equation could be solved exactly. A form to circumvent this problem is by using the proposition of Kohn and Sham [129] that substitutes the real electrons with effective ones, where it is suggested to use the kinetic energy of the non-interacting system to describe the real system (which has interaction):

$$T_s = -\frac{\hbar^2}{2m_e} \sum_i^n \langle \psi_i | \nabla^2 | \psi_i \rangle \tag{2.77}$$

The correction for the use of this term is called the exchange-correlation energy functional, $E_{xc}[\rho]$. A simple comparison between HF and DFT methods is that, while post-HF could give the exact solutions if not for the computational times, DFT solutions can only get as close to the exact solution of the system if the exchange-correlation potential was the exact one as well.

$$F[\rho] = T_s[\rho] + J[\rho] + E_{xc}[\rho] \tag{2.78}$$

$$E_{xc}[\rho] = (T[\rho] - T_s[\rho]) + (E_{e,e}[\rho] - J[\rho]) \tag{2.79}$$

It is still possible to define the local exchange-correlation potential:

$$V_{xc} = \frac{\delta E_{xc}(\mathbf{r})}{\delta \rho(\mathbf{r})} \tag{2.80}$$

To minimize the energy in order to find the ground state, Lagrange's multiplier approach ($L[\rho]$) can be applied, where $\delta L/\delta\rho = 0$:

$$L[\rho] = E[\rho] - \sum_i \varepsilon_i \left[\int \psi_i^* \psi_i d\mathbf{r} - 1 \right] \tag{2.81}$$

$$\frac{\delta L}{\delta \rho} = \frac{\delta T_s}{\delta \rho} + \int \frac{\rho(\mathbf{r}')}{|\mathbf{r} - \mathbf{r}'|} d\mathbf{r}' + V_{xc} + V_{e,N} - \varepsilon_i = 0 \tag{2.82}$$

$$\frac{\delta T_s}{\delta \rho} = \frac{\delta T_s}{\delta \psi_i^*} \frac{\delta \psi_i^*}{\delta \rho} = -\frac{\hbar^2}{2m_e} \frac{\nabla^2 \psi_i}{\psi_i} \tag{2.83}$$

Finally, the Kohn-Sham equations can be found as the following:

$$\left[-\frac{\hbar^2}{2m_e} \nabla^2 + v_{eff}(\mathbf{r}) \right] \psi_i = \varepsilon_i \psi_i \tag{2.84}$$

$$v_{eff}(\mathbf{r}_1) = e^2 \int \frac{\rho(\mathbf{r}')}{|\mathbf{r} - \mathbf{r}'|} d\mathbf{r}_2 + V_{xc}(\mathbf{r}) + V_{e,N} \tag{2.85}$$

It can be observed from the last equation that if the form of V_{xc} is known, the Kohn-Sham equations could be solved exactly. One interpretation of these equations shows that the value of the highest occupied orbital, ε_i^{max}, is equal to the negative of the ionization energy. As the electronic density is the input of equation (2.84), there must be a self-consistent approach to the determination of the ground state, summarized in Figure 33. By finding the self-consistent density, the energy can be written as:

$$E_{scf} = \sum_{i=1}^{n} \varepsilon_i - \frac{e^2}{2} \int \int \frac{\rho_{scf}(\mathbf{r}) \rho_{scf}(\mathbf{r}')}{|\mathbf{r} - \mathbf{r}'|} d\mathbf{r} d\mathbf{r}' - \int \rho_{scf}(\mathbf{r}) V_{ext}(\mathbf{r}) d\mathbf{r} + E_{xc}[\rho_{scf}(\mathbf{r})] \tag{2.86}$$

An additional step is to consider that, because of the steep potential variations around the nucleus and the core-electrons, the potential can be described by pseudopotentials that define a cut-off radius between the core and the valence electrons. These pseudopotentials can describe the core-electrons as independent of the chemical environment of the system. Some approximations used such as the Local Density Approximation, Generalized Gradient Approximation and the Plane Wave Basis are described in Appendix A.

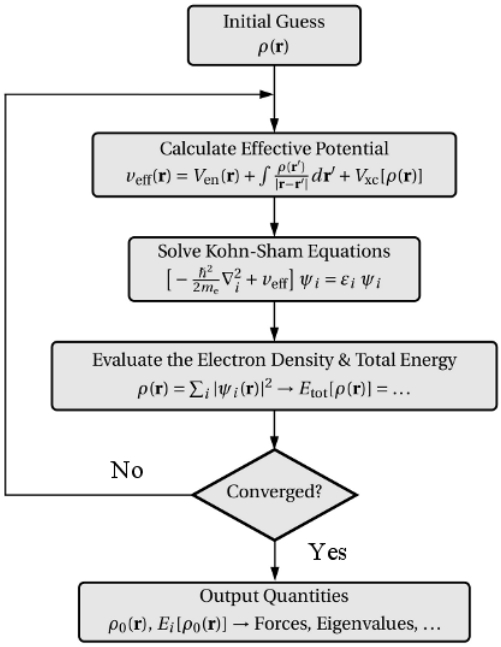

Figure 33 – Self-consistent approach to ground state calculation. Adapted from [130].

3 Experimental and Theoretical Procedures

A detailed description of the methodology used throughout the present work is given in this chapter.

3.1 Synthesis of Ni nanoparticles and heating treatment

Ni nanoparticles were synthesized in accordance with a previous work of the group [131]. In summary, a solution of $NiCl_2 \cdot 6H_2O$ (203 mg, 0.85 mmol) was dissolved in the 3 mL of the ionic liquid BMI·BF_4 (1-butyl-3-methylimidazolium tetrafluoroborate), then kept under magnetic stirring at room temperature for 15 min. A solution of $NaBH_4$ (321 mg, 8.5 mmol) dissolved in methanol (3 mL) was added to the initial solution. The formation of Ni nanoparticles could be observed as the reaction mixture turned black. The solution was then washed with methanol (3 times, 5 mL) and dichloromethane (3 times, 5 mL). In order to obtain the powder sample, the solution was centrifuged at 3500 rpm and dried under reduced pressure.

Aiming to optimize the oxidation state of the Ni nanoparticles for the methylene blue photodegradation reaction, the as-prepared Ni nanoparticles were heated from room temperature to selected temperatures of 100 ºC, 300 ºC or 500 ºC under ambient atmosphere inside a muffle furnace. A heating rate of 10 ºC/min was used, and the samples remained 1 hour at the target temperature. At the end, the samples were cooled inside the furnace until about 30 ºC. The as-prepared Ni nanoparticles and those treated at 100 ºC, 300 ºC, and 500 ºC are labeled as Ni, Ni100, Ni300 and Ni500, respectively. The Ni nanoparticles were mixed with commercial $SrTiO_3$ (Sigma Aldrich, 99% purity, size below 100 nm) with 5 wt% and mechanically stirred (solid grinding) for 10 min. After this, the powder achieved a homogeneous gray color. Then, the powder mixtures were sonicated for 30 min in a conventional ultrasonic bath. These samples are labeled hereafter as Ni/$SrTiO_3$, Ni100/$SrTiO_3$, Ni300/$SrTiO_3$ and Ni500/$SrTiO_3$. The $SrTiO_3$ powder presented a specific surface area of 24 m^2/g, as obtained by nitrogen adsorption-desorption measurements and estimated using BET theory (not shown here), and a non-porous structure.

3.2 Ion irradiation on $SrTiO_3$

In order to create O vacancies in the support, the $SrTiO_3$ powder was irradiated using Au^{7+} ions with an incident energy of 16 MeV. It must be noted that, with this energy not only O vacancies are created, but Sr and Ti vacancies can be promoted as well (see simulation results in 4.2). The ion irradiation was performed with the Tandetron 3MV accelerator at the Laboratório de Implantação Iônica at IF-UFRGS. Au^{1-} ions are initially created by sputtering and extracted by an applied potential. Then, the ions are directed towards a N_2 gas stripper, producing Au^{7+} ions by a multi-electron process (which creates a charge state distribution of the Au ions). An Al sample holder for powders previously designed by our group was used, which is shown in Figure 34. Around 48 mg of $SrTiO_3$ powder was dispersed at the delimited black area of the sample holder. The sample holder was installed at the vacuum chamber (pressure $\approx 5 \times 10^{-7}$ mbar) in the horizontal position so that the angle between the sample surface and the ion path is 65 °. The fluences used were 1×10^{13} ions/cm^2, 5×10^{13} ions/cm^2 and 1×10^{14} ions/cm^2. These samples are named hereafter as $SrTiO_3$ 1E13, $SrTiO_3$ 5E13 and $SrTiO_3$ 1E14, respectively. The current measured at the terminal varied between few nA to 20 nA.

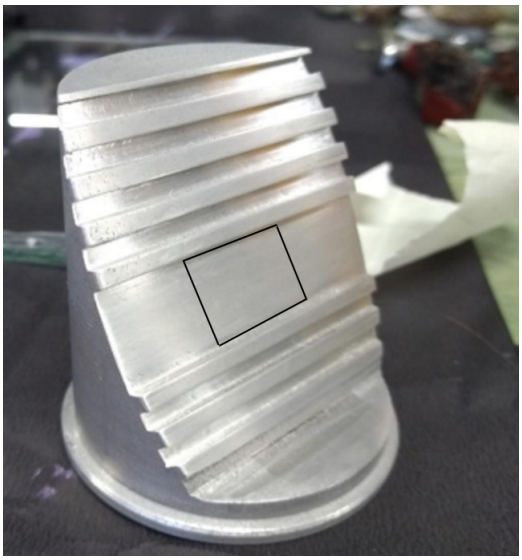

Figure 34 – The sample holder used for ion irradiation procedures. The powder is distributed inside the delimited 1×1 cm^2 black area (representation).

At the end of the ion irradiation process, it was observed that the aluminum sample holder changed, turning into a darker color, which occurs due to the Au implantation at the sample holder. The $SrTiO_3$ powder also changed from white to a grayish color.

3.3 X-Ray Diffraction measurements

The Ni and $SrTiO_3$ as-prepared nanoparticles and the ion irradiated $SrTiO_3$ nanoparticles were analyzed with XRD measurements. The measurements were conducted at the Centro de Nanociência e Nanotecnologia (CNANO-UFRGS) using a conventional Rigaku diffractometer with a Cu Kα X-ray source (λ = 1.5405 Å) working at 40 kV and 17 mA. The step size used in the measurements was 0.05 º, the step rate of 0.33 º/min and a 2θ range from 20 º to 90 º. The indexing of the XRD patterns was performed using the PCPPDFWIN version 2.1 (JCPDS-ICDD database). The powder samples were homogeneously deposited at the sample holder for these measurements.

After this procedure, Rietveld refinement was applied to analyze the diffractograms with the FullProf Suite package [132]. The patterns were fitted considering the CIF files retrieved from the JCPDS-ICDD database, fixing the occupancy numbers. Linear interpolation was selected to fit the background and Thompson-Cox-Hastings pseudo-Voigt peak shape was chosen to correct axial divergence asymmetry. Overall B-factors were considered to improve the fitting quality. Refinement was conducted by considering the least squares minimization method and a maximum of 100 steps. Additionally, in order to obtain the equipment resolution file, the diffractogram of a quartz standard sample was used. By refining this sample, the V and W parameters of the reflection profile were obtained. Afterward, they were fixed at 0 to obtain the size and strain from the refinement. The transparency instrumental parameter was constrained to have only positive values. The zero instrumental factor was fitted in the XRD pattern of the as-prepared $SrTiO_3$ sample and fixed to this value only for the XRD patterns of $SrTiO_3$ samples after ion irradiation. The zero instrumental factor for the XRD pattern of the Ni nanoparticles was allowed to vary.

3.4 Small-Angle X-Ray Scattering measurements

Information about the size distribution and general morphology of the Ni and $SrTiO_3$ as-prepared nanoparticles was investigated by the SAXS technique. The measurements were conducted in the Nano-inXider (Xenocs) equipment at CNANO-UFRGS. The powder sample was inserted in the sample holder for solids and sealed with a kapton tape (thickness around 0.1 mm). The SAXS patterns were acquired with a Cu Kα X-ray source ($\lambda = 1.54$ Å), a semitransparent beamstop and a Dectris Pilatus 3 detector. The measurements were performed

in transmission mode and the 2θ range from 0.00 ° to 5.25 ° with a 60 s exposure time for each scan. The final pattern resulted from an average of 120 scans for each sample. The kapton tape was measured as well in order to perform the background subtraction of the SAXS patterns.

The conversion of symmetric 2D SAXS data to 1D and the average between multiple scans were accomplished in the FOXTROT software [133]. The SAXS patterns were analyzed using the SASfit software [98]. The SAXS data was first subtracted by the SAXS pattern of a kapton foil. Then, it was subtracted by a background function

$$I(q) = c_0 + c_4 q^{-\alpha} \tag{3.1}$$

which was adjusted to reach the best c_0, c_4 and α parameters. The first parameter is related to the inelastic scattering background while the last two give information about the fractal dimension of the sample. The subtraction of the background function allows highlighting the oscillations while still preserving the general shape of the pattern. The scattering length density was estimated from the built-in plugin of the SASfit software, where the necessary input is given by the bulk density of the compound, the molecular formula and the X-ray energy. Overall, the fitting procedure was made using log-normal size distributions, given by:

$$L_N(r) = \frac{N}{r^p} \exp\left[-\frac{(\ln(r) - \ln(\mu))^2}{2\sigma^2}\right] \tag{3.2}$$

where N is the normalization factor, proportional to the percentage of the population contribution to the pattern; r is the radius of the nanoparticle; p, μ and σ are related to the m-th moment of the distribution:

$$\langle r^m \rangle = \mu^m e^{\frac{1}{2}\sigma^2 m(2-2p+m)} \tag{3.3}$$

3.5 Transmission Electron Microscopy measurements

The size distribution of the $SrTiO_3$ and the Ni as-prepared nanoparticles were obtained through TEM using the JEOL JEM–1200 EXII microscope at Centro de Microscopia e Microanálise (CMM-UFRGS). The nanoparticles powder samples were dispersed in Milli-Q water by sonication for 30 min. Afterward, a drop of the corresponding solution was deposited on a C-coated Cu grid. The microscope was operated with an accelerating voltage of 80 kV. The TEM images were analyzed using the ImageJ software [134]. The sizes were estimated manually by

drawing two perpendicular lines across selected nanoparticles and averaging the length between both lines.

3.6 In situ X-ray Absorption measurements

In situ XAS and in situ time-resolved XAS measurements were performed at the Laboratório Nacional de Luz Síncrotron (LNLS), aiming to probe the local atomic order around Ni atoms and the time evolution of the Ni oxidation state during thermal treatment. For the measurements, around 9 mg of Ni nanoparticles powder was mixed with 41 mg of BN. The powder was compacted in order to produce 5 mm diameter pellets. The pellet was inserted in a tubular furnace connected to a gas flux system. Then, 100 ml/min of synthetic air was inserted into the furnace and the pellet was heated to the selected temperatures of 100 ºC, 300 ºC, or 500 ºC, with a heating rate of 10 ºC/min. For a given selected temperature, the sample was kept under synthetic air for 1 h. Then, the sample was cooled to room temperature under exposition to synthetic air. The measurements were conducted at the Ni K edge (8333 eV) in the transmission mode during the full thermal treatment described.

The in situ EXAFS measurements were performed at the D08B-XAFS2 beamline [135] at LNLS. A Si(111) double crystal monochromator and three ionization chambers filled with Ar composed the workstation in which the spectra were obtained. A Ni foil was placed in front of the third ionization chamber and it was used for calibration purposes. The measurements were performed at the selected temperatures described above, from 8260 to 9130 eV range, with a 1 eV (EXAFS) and 0.4 eV (XANES) step size and 2 s/point (EXAFS) and 1 s/point (XANES). In order to improve the signal-to-noise ratio, two to three scans were measured for each sample.

The in situ time-resolved XANES measurements were conducted at the D06A-DXAS beamline [136] at LNLS. The dispersive polychromator consisted of a curved Si(111) crystal that focuses the X-ray beam in the horizontal plane down to about 200 μm. A mirror also focused the beam in the vertical plane to about 500 μm. The detector consisted of a position-sensitive CCD camera. The time resolution is around 100 ms. The in situ time-resolved XANES spectra were acquired during the thermal treatment every 2 s in the 8167 to 8735 eV range.

The IFEFFIT [120] package integrated into Demeter [137] was used for the standard procedure of data reduction [138] of the EXAFS and XANES spectra. The Fourier transformation of the k^2-weighted EXAFS oscillations was made using a Kaiser-Bessel window with a Δk

range of 8.6 Å^{-1}. The scattering paths and the corresponding scattering amplitude and phase shift were obtained with the FEFF6 code [120]. A metallic cluster of Ni and another cluster of NiO, both of 10 Å size, were considered in the scattering path calculations. After determining the S_0^2 parameter as 0.80 from the fitting of the FT of the Ni standard, it was fixed for the other Ni samples. The R-factor was always lower than 0.005, which shows a great agreement between the model proposed and the experimental result.

The in situ XANES spectra from both XAFS2 and DXAS bealmines were fitted with a linear combination analysis using Ni^0, NiO and $NiCl_2$ standard spectra. The sum of the weight of the compounds was set to be equal to 1.0 and their values were constrained to vary between 0 and 1.

3.7 Photocatalytic reactions

The homemade photoreactor used in the present work is described elsewhere [139]. For the reaction, 5 mL of 3.5 ppm methylene blue (0.01 mM) in Milli-Q water was mixed with 28 mg of Ni/$SrTiO_3$, Ni100/$SrTiO_3$, Ni300/$SrTiO_3$ or Ni500/$SrTiO_3$, maintaining the solution in the dark under magnetic stirring for 30 min to disperse the nanoparticles. The photodegradation reaction was conducted with a germicidal UV lamp (UV-Bravo, λ centered around 254 nm) of 15 W for 30 min. The distance from the surface of the lamp to the surface of the solution was fixed to 5 cm. Along with the catalyst solution, a solution of methylene blue without nanoparticles was used as a control group in order to verify the stability of the reactor. At the end, the solution with the nanoparticles was centrifuged under 2500 rpm for 20 min and UV-Vis measurements in transmission mode were carried out with the supernatant using a Shimadzu UV-2450PC UV-Vis spectrometer. As the data presented a constant background due to the scattering of very small particles in the solution that were not separated by centrifugation, the absorbance was subtracted by this minimum value (at 800 nm).

The ion irradiated $SrTiO_3$ samples were used in the photodegradation reaction in the same reactor but using a 10 W LED light source (λ centered around 365 nm). Under this configuration, the methylene blue solution was optimized to 5 ppm, and 4 mg of the powder was dispersed on 4 mL of the solution.

3.8 X-ray Photoelectron Spectroscopy measurements

The X-Ray Photoelectron Spectroscopy (XPS) measurements of the nanoparticles before and after photodegradation reaction were performed at the D04A-SXS beamline [140] at LNLS. The InSb(111) double-crystal monochromator installed at the workstation was set for a fixed photon energy of 1900 eV. The monochromator photon energy calibration was done at the Si K edge (1839 eV). The XPS spectra were acquired using a hemispherical electron analyzer (PHOIBOS HSA500 150 R6) and obtained at a 45 ° take-off angle at room temperature. The samples were investigated at the long scan, C 1s, O 1s, Ni 2p, Ti 2p and Sr 3d electronic regions. The long scan and high resolution spectra were obtained with a 60 eV and 20 eV pass energy, and energy step of 1 eV and 0.1 eV, respectively. The dwell time was 100 ms/point in all cases. The overall resolution was around 0.3 eV. The base pressure used inside the chamber was around 5.0×10^{-9} mbar. The analyzer's energy was calibrated using a standard Au foil (Au $4f_{7/2}$ peak at 84.0 eV). Charging effects were considered by referring to the C 1s adventitious peak position at 284.5 eV.

The spectra were analyzed with the XPSpeak 4.1 software. The fitting used a Shirley-type background and a symmetric Gaussian-Lorentzian sum function (23 % Lorentzian contribution), as determined from the analysis of the Au 4f region of Au standard. No significant charging effects were observed. The FWHM and relative binding energy of a given component was constrained to the same value in all samples.

3.9 Density functional theory calculations

Density functional theory (DFT) calculations were performed within the Quantum ESPRESSO 5.4.0 [141] suite of codes through the plane waves self-consistency field (PWSCF) method at Centro Nacional de Supercomputação (CESUP-UFRGS). Projector-Augmented Wave (PAW) pseudopotentials generated by the *atomic* code [142] within the pslibrary were used to describe the Sr (4s, 5s, 4p, 5p), Ti (3s, 4s, 3p, 3d), O (2s, 2p) and Ni (3d, 4s, 4p) electronic states. The calculations were initially performed in the generalized gradient approximation (GGA), using Perdew−Burke−Ernzerhof (PBE) exchange-correlation functionals. A slab model was built for both SrO and TiO_2 terminations of $SrTiO_3$ (001) surface, where the vacuum layer was fixed to 20 Å. The TiO_2 termination slab was composed of a $2 \times 2 \times 3$ supercell with 60 atoms. The SrO termination slab was composed of a $2 \times 2 \times 3$ supercell, except that its last layer was

removed to obtain the proper termination, obtaining a 48 atom system. The total energy per atom convergences are shown in Figures 35 and 36. Vacuum size convergence and supercell size convergences are shown in Appendix A.

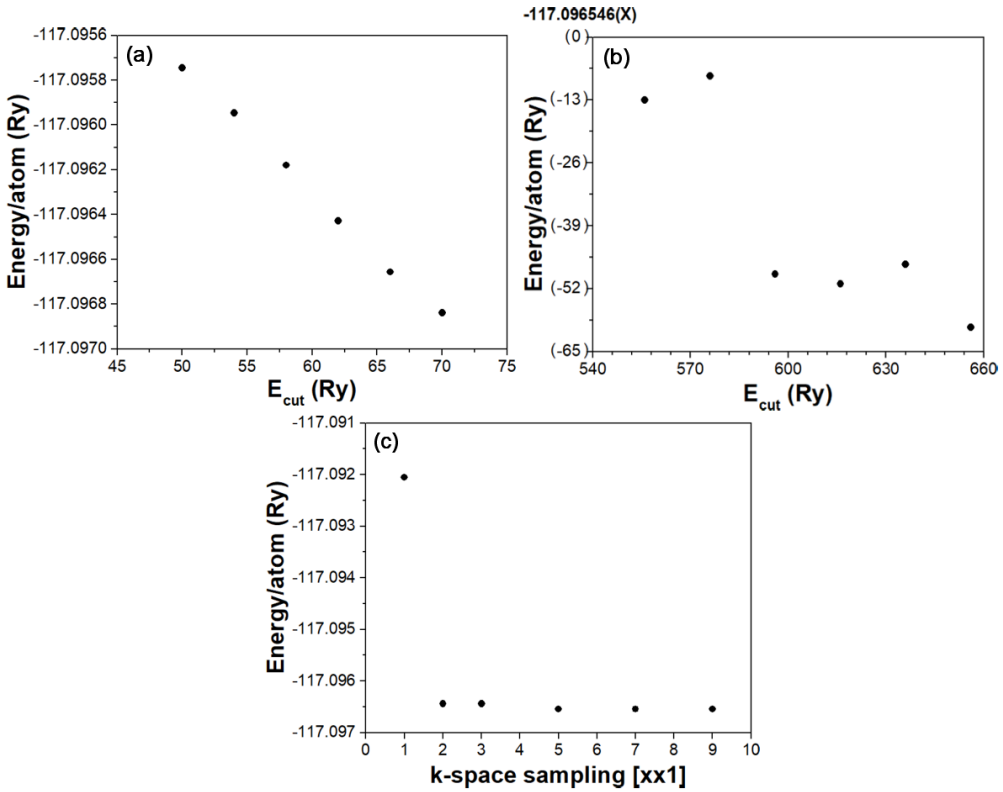

Figure 35 – Convergence tests for SrO terminated $SrTiO_3$ slabs (48 atoms) (a) wavefunction energy cut-off, (b) electron density energy cut-off and (c) [k k 1] reciprocal space sampling.

A sequence of energy minimization and geometry optimization calculations were performed, relaxing the system until the force per atom reached 10^{-5} eV Å^{-1}. The kinetic energy cutoff for the wave functions was set to 60 Ry and the charge density cutoff to 620 Ry after convergence tests. The Brillouin zone was integrated using a $5 \times 5 \times 1$ k-point mesh for the slab representations. Gaussian smearing, with a σ value equal to 0.01, was used to improve the convergence of the system. The electronic ground states were determined after an electronic energy convergence of 10^{-6} eV. Since the indirect band gap of the TiO_2 termination slab was close to zero, the Hubbard U parameter was considered. First, the linear response method was used, obtaining a value of 1.6 eV. However, this value did not improve the band gap value, thus values from the literature were used. Different U and J parameters were tested [143]: $U = 3.2$ and $J = 0$, $U = 3.2$ and $J = 0.9$, $U = 5$ and $J = 0$, $U = 5$ and $J = 0.64$. The band gap value did not improve much with either value. By changing the GGA+U approximation to the LDA+U

($U = 5$ and $J = 0$) approximation (and relaxing the system under the same configuration from the initial state) with Perdew-Zunger exchange-correlation functional (PZ), the indirect band gap value of the TiO_2 termination could be somewhat improved. In order to improve even further the band gap, a hybrid functional approximation would be necessary, but this is outside the scope of the present work.

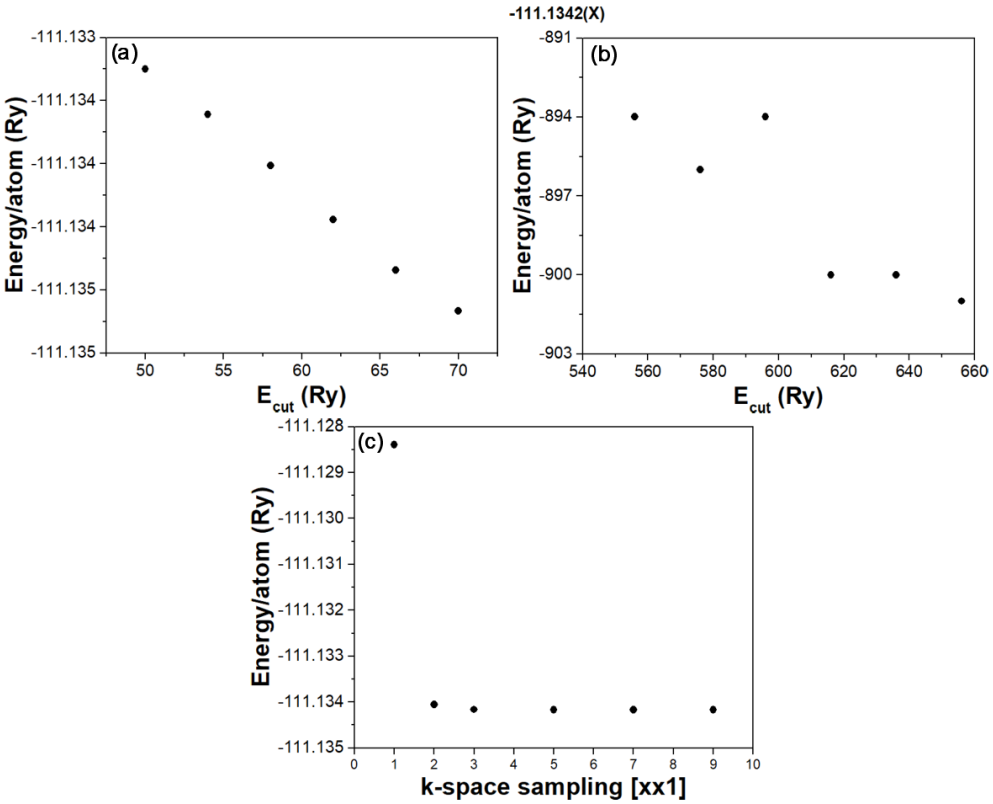

Figure 36 – Convergence tests for TiO_2 terminated $SrTiO_3$ slabs (60 atoms) (a) wavefunction energy cut-off, (b) electron density energy cut-off and (c) [k k 1] reciprocal space sampling.

After the slab systems energy minimization processes, a 4 atom Ni cluster was included over each slab. The system was allowed to relax again with the Local-Spin Density Approximation (which includes magnetization effects). The vacuum size between the top of the Ni cluster and the bottom of the slab was maintained at 20 Å. Overall, the same previous values for convergence were used for these setups. No Hubbard parameter was assigned for the Ni valence orbitals. However, the Gaussian smearing had to be changed from 0.01 until 0.0004 to decrease fractional occupancy effects during the minimization process.

4 Results and Discussion

4.1 Ni/$SrTiO_3$ nanoparticles

Figure 37 shows the XRD patterns of (a) $SrTiO_3$ and (b) Ni nanoparticles. The Bragg reflections of $SrTiO_3$ support can be assigned to $SrTiO_3$, $SrCO_3$, and $BaTiO_3$ crystalline phases. Both $SrCO_3$ and $BaTiO_3$ compounds come from the synthesis procedure (molten salts) [56] and they are present in small amounts (around 2 % each). The Rietveld refinement allows obtaining the mean crystallite size of around 35 nm for $SrTiO_3$ nanoparticles. For the Ni nanoparticles, the XRD pattern presents Bragg reflections wider than those of the XRD pattern of $SrTiO_3$ nanoparticles and a pronounced inelastic background. The Bragg reflections are assigned to Ni and $NiCl_2$ crystal structures and are associated with small or highly disordered nanoparticles. It is possible to infer that the $NiCl_2$ compound comes from the synthesis procedure, as observed previously [131]. A mean crystallite size of 2 nm was obtained for the Ni nanoparticles through Rietveld refinement.

Figure 38 shows the SAXS patterns for both (a) $SrTiO_3$ and (b) Ni nanoparticles. The optimized background α parameter presents values of 3.98 for the $SrTiO_3$ support and 3.95 for the Ni nanoparticles, which indicates that both surfaces are not very rough. Since monodisperse samples show steep minima in the patterns, the oscillations are associated with polydisperse

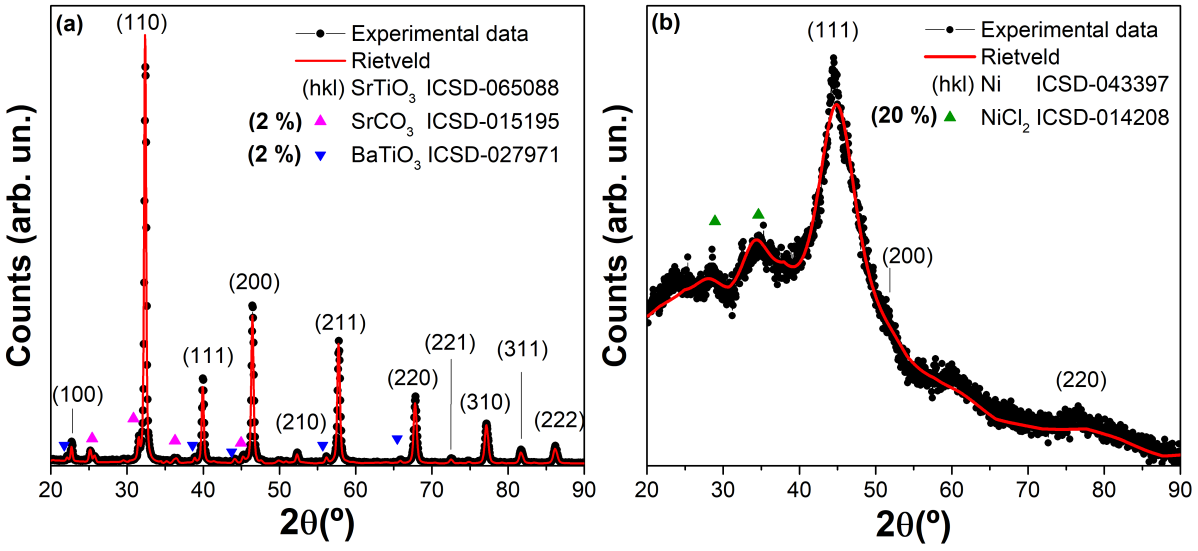

Figure 37 – XRD patterns of (a) $SrTiO_3$ and (b) as-prepared Ni nanoparticles. Rietveld refinement results are shown as in the red lines.

samples in both cases. In the Ni nanoparticles SAXS data, it is possible to see an oscillation with a longer wavelength than that of the $SrTiO_3$ sample, which indicates the Ni nanoparticles are smaller than the $SrTiO_3$ nanoparticles. The SAXS pattern of the $SrTiO_3$ nanoparticles is fitted by a single population of spherical shape nanoparticles with an average size of (33.0 ± 0.2) nm, which is in agreement with the XRD results. Furthermore, Transmission Electron Microscopy (TEM) images were obtained for the $SrTiO_3$ sample, and the average size of (30 ± 3) nm corroborates the size obtained by both XRD and SAXS measurements, as shown in Figure 39 (a).

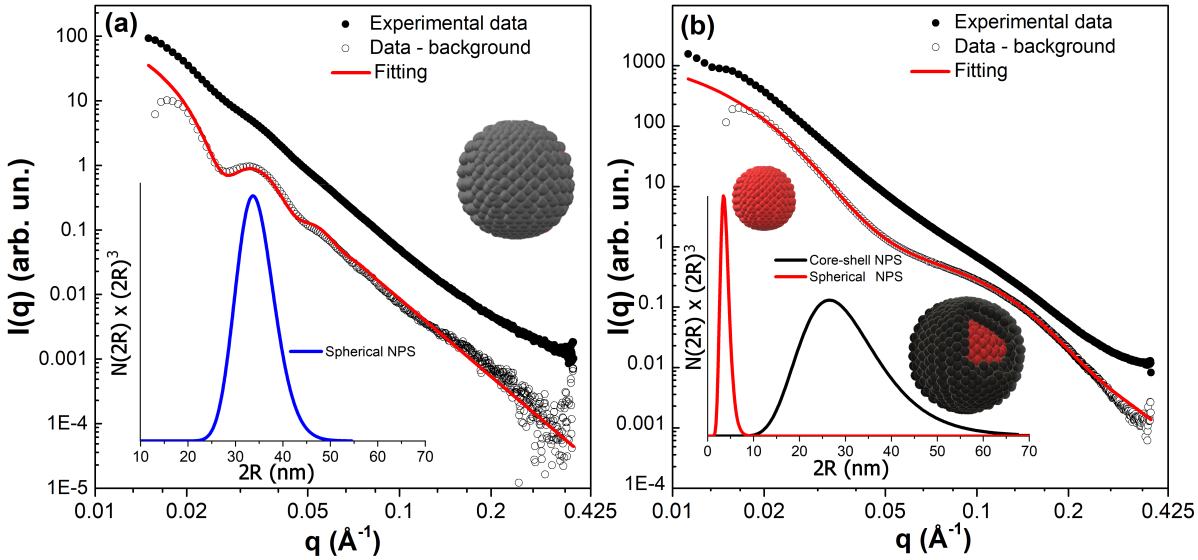

Figure 38 – SAXS patterns for (a) $SrTiO_3$ and (b) Ni nanoparticles. The insets present the log-normal distributions obtained from the fitting procedure. Nanoparticles morphology are also represented by the spheres.

Nonetheless, the SAXS pattern of the Ni nanoparticles was adjusted by a combination of two spherical populations of different sizes. The bigger one presents a core-shell-like structure, where the ratio between the electronic density at the core and shell regions is fitted to 1.56. The electronic density of the core region was restricted to the same value found in the spherical population of smaller sizes. It can be interpreted initially in two distinct ways: as the core composed mainly of Ni^0 and the shell composed mainly of oxidized Ni phases such as NiO, $Ni(OH)_2$ or $NiCl_2$, which comes from the synthesis procedure or atmosphere moisture, or aggregation of smaller Ni nanoparticles more densely-packed at the core. The average size of the spherical and core-shell-like spherical populations are found as (3.04 ± 0.04) nm and (22.6 ± 0.4) nm (shell thickness of around 7 nm), but the main contribution (around 99 %) comes from the smaller size population. This result is in agreement with the XRD data but

enables detecting a morphology hardly observed by TEM due to the low concentration. The size histogram of the Ni nanoparticles (Figure 39 (b)) obtained through TEM analysis has an average size of (4 ± 2) nm, which also corroborates both XRD and SAXS data.

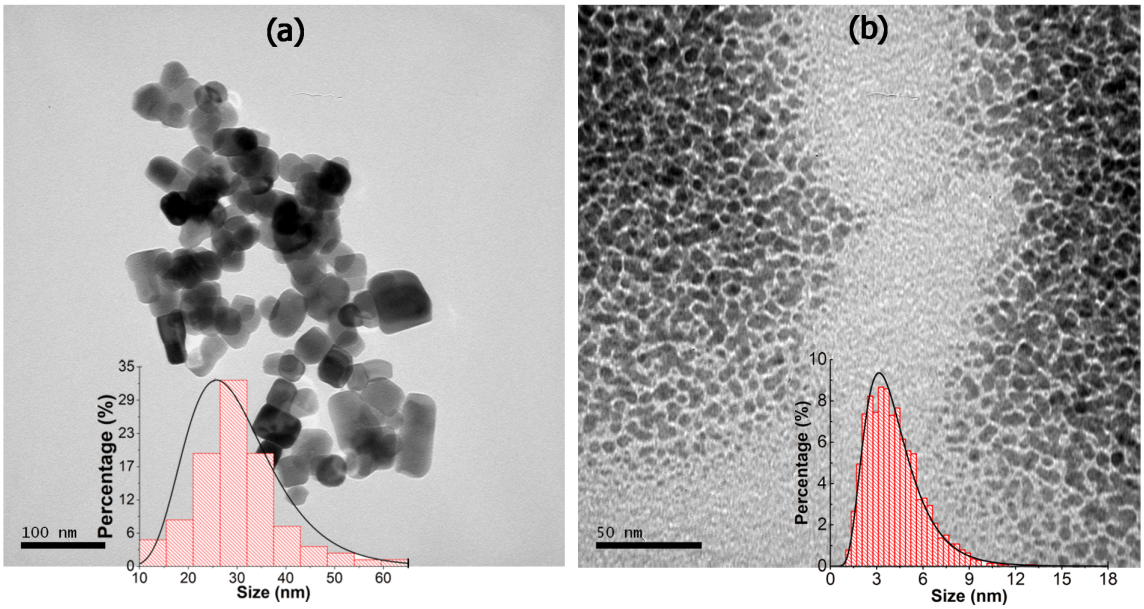

Figure 39 – Typical TEM images of the (a) $SrTiO_3$ and (b) Ni nanoparticles. The histograms are shown in the inset.

Figure 40 shows the in situ XANES measurement at Ni K edge during thermal treatment at selected temperatures and the respective linear combination analysis. The chemical component percentage for the different samples can be observed in Figure 41. The Ni K edge XANES spectrum comes from the electronic transition $1s \rightarrow 4p$. It is possible to observe a clear increase of the intensity at the edge region during heating treatment at 500 ºC, which is associated with an increase of the number of empty states at Ni 4p electronic level and it indicates the occurrence of oxidation of the Ni nanoparticles. One can observe also the presence of Ni^0 and $NiCl_2$ compounds in the as-prepared Ni nanoparticles, in accordance with the XRD data. The observed percentages do not need to match the ones obtained from XRD, as XAS can detect more than the atoms present in a crystalline structure. Even if not identified in the XRD pattern, the NiO compound was considered in the analysis and it is present at the surface of the nanoparticles (as shown later by XPS analysis). It makes a significant contribution to the XANES spectra due to the small size of the Ni nanoparticles. The analysis of the results shows a high amount of Ni^0 $(55\ \%)$ in the as-prepared Ni nanoparticles. The thermal treatment induces a slight increase of the Ni^0 amount to $65\ \%$ at 300 ºC, with a slight decrease of the NiO contribution. The reduction of NiO crystals has been observed in diluted O atmospheres to begin at 330 ºC [144], and this process could be

facilitated for nanoparticles presenting a very small size of around 3 nm. These results show the possibility of tuning the oxidation state of the Ni nanoparticles.

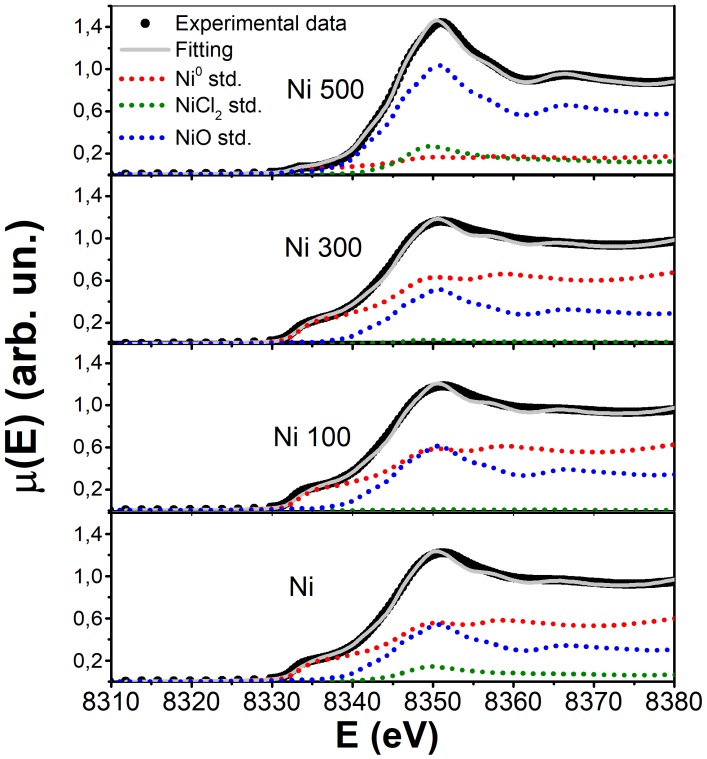

Figure 40 – In situ XANES measurements at the Ni K edge nanoparticles during heating treatment in synthetic air. Dotted lines represent the standard samples measured and used for the linear combination analysis.

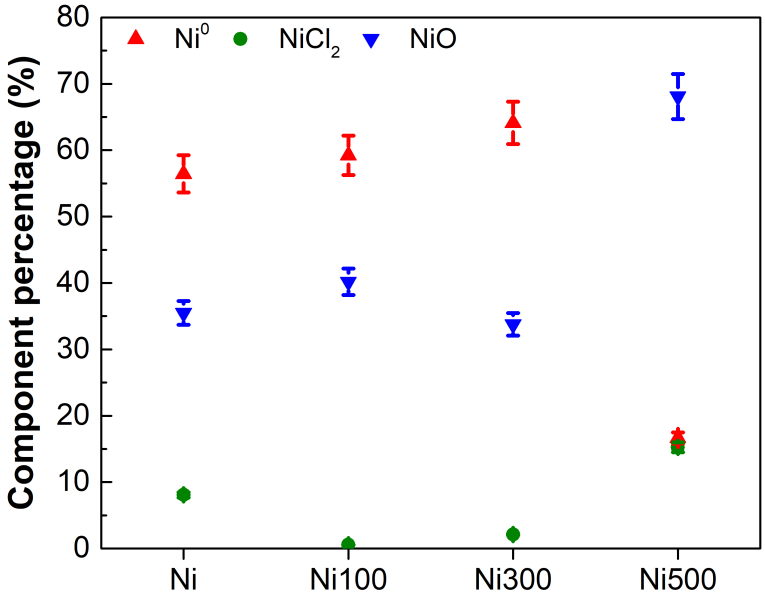

Figure 41 – Percentage of chemical components from in situ XANES analysis during heating treatment in synthetic air of Ni nanoparticles.

The local atomic order around Ni atoms was probed by in situ EXAFS measurements at

the Ni K edge. Figure 42 shows (a) the k^2 weighted EXAFS oscillations and (b) the corresponding Fourier Transform. The EXAFS oscillations of the as-prepared Ni nanoparticles show the main features of fcc metallic Ni, as observed in comparison to the Ni standard data, but the EXAFS oscillations are dumped due to the small particle size. The increase of the temperature of thermal treatment to 300 ºC induces a slight change in the EXAFS oscillations at around 4 Å^{-1}. At 500 ºC, there is a stronger change in the EXAFS oscillations, which occurs due to the transformation from Ni^0 to NiO. It is interesting to note that, besides increasing temperature, it is not observed a further dumping of the EXAFS oscillations in comparison to the as-prepared case. A possibility is that the thermal disorder is compensated by the increase of the mean particle size. The Fourier Transform presents two main contributions at the coordination shell at around 1.5 Å and 2.2 Å (not phase corrected). The contribution at a shorter distance comes from a Ni-O scattering path, while that at a longer distance comes from Ni-Ni scattering path. It is also possible to observe that the Ni-O contribution becomes less important until 300 ºC, corroborating the XANES analysis, but at 500 ºC it has a significant contribution to the Fourier Transform.

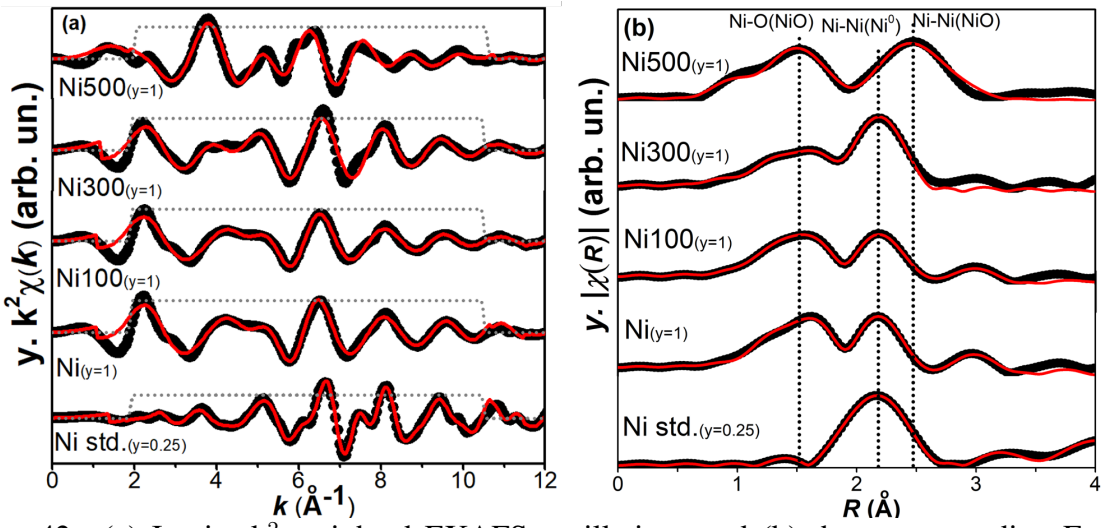

Figure 42 – (a) In situ k^2 weighted EXAFS oscillations and (b) the corresponding Fourier transform of EXAFS measurements at Ni K edge. The black points, grey dotted line and the red solid line represent the experimental data, Kaiser-Bessel window and the best fitting result, respectively. Ni-O(NiO), Ni-Ni(Ni^0) and Ni-Ni(NiO) stand for Ni-O, Ni-Ni and Ni-Ni scattering paths from NiO, Ni^0 and NiO clusters, respectively. The EXAFS oscillations and the corresponding FT of Ni standard were multiplied by 0.25 for comparison purposes.

Table 2 shows the fitting results. There is a strong change in the local atomic order around Ni atoms after thermal treatment at 500 ºC. Note that the Ni-Ni contribution from Ni^0 tends to zero ($N_{\text{Ni-Ni}} = 0.3 \pm 0.2$) but it increases from 2.38 ± 0.07 to 4.9 ± 0.2 for increasing temperatures until 300 ºC. The corresponding change is observed in the coordination numbers of

the Ni-O and Ni-Ni from NiO cluster scattering paths. The expected increase of the Debye-Waller factor and scattering path due to the increase of the temperature is also observed in Table 2.

Table 2 – Parameters obtained from the fit of the FT of the EXAFS oscillations for the Ni nanoparticles

Parameter	N			σ^2 (Å^2)		
Path	**Ni-O(NiO)**	**Ni-Ni(Ni^0)**	**Ni-Ni(NiO)**	**Ni-O(NiO)**	**Ni-Ni(Ni^0)**	**Ni-Ni(NiO)**
Ni	3.18 (0.09)	2.38 (0.07)	2.0 (0.2)	0.0109 (0.0006)	0.0058 (0.0003)	0.011 (0.001)
Ni100	2.78 (0.06)	2.83 (0.06)	0.9 (0.1)	0.0113 (0.0005)	0.0092 (0.0002)	0.012 (0.002)
Ni300	2.4 (0.1)	4.9 (0.2)	-	0.013 (0.001)	0.0102 (0.0003)	-
Ni500	4.6 (0.3)	0.3 (0.2)	11.7 (0.8)	0.011 (0.001)	0.014 (0.007)	0.0157 (0.0007)

Figure 43 shows the in situ time-resolved XANES measurement at Ni K edge for the thermal treatment in synthetic air at (a) 100 ºC, (b) 300 ºC and (c) 500 ºC and the respective chemical component percentage evolution as a function of time and temperature. The major changes in the in situ time-resolved XANES spectra are observed for the sample heated to 500 ºC with the increase of the intensity at the edge due to the oxidation of the nanoparticles. The analysis results show that the Ni^0 component is the predominant one until 500 ºC. At 500 ºC, a gradual oxidation of the sample occurs during the isothermal step. After 60 minutes in this temperature no more significant changes are observed in the NiO percentage, which stabilizes at approximately 65 %. These results show the possibility of a fine-tuning in the oxidation state of Ni nanoparticles, as observed in the region around 450 ºC in the component percentage of Ni nanoparticles heated to 500 ºC, which should have a great influence on the photodegradation of methylene blue. Particularly, the thermal treatment at 500 ºC allows the presence mainly of NiO and, consequently, the possibility of a NiO/$SrTiO_3$ heterojunction.

Figure 44 shows the UV-Vis measurements carried out after the photodegradation reactions. The spectra shown represent the major absorption band of methylene blue. The decrease in the absorption band intensity is directly related to the amount of methylene blue removed from the solution or adsorbed by the nanoparticles (which should be negligible). The photodegradation can sometimes induce a shift in the absorption spectrum. This can be explained by the formation of oligomers and the agglomeration of the dye molecules [145]. Furthermore, the interaction of active oxygen species formed in the reaction, such as $\cdot O^{-2}$, with the N-ethyl group of some dyes can cause a blue shift in the spectrum as well. The degradation percentages can be calculated as

$$\text{Percentage of degradation} = 100(\%)\left(1 - \frac{A}{A_0}\right) \tag{4.1}$$

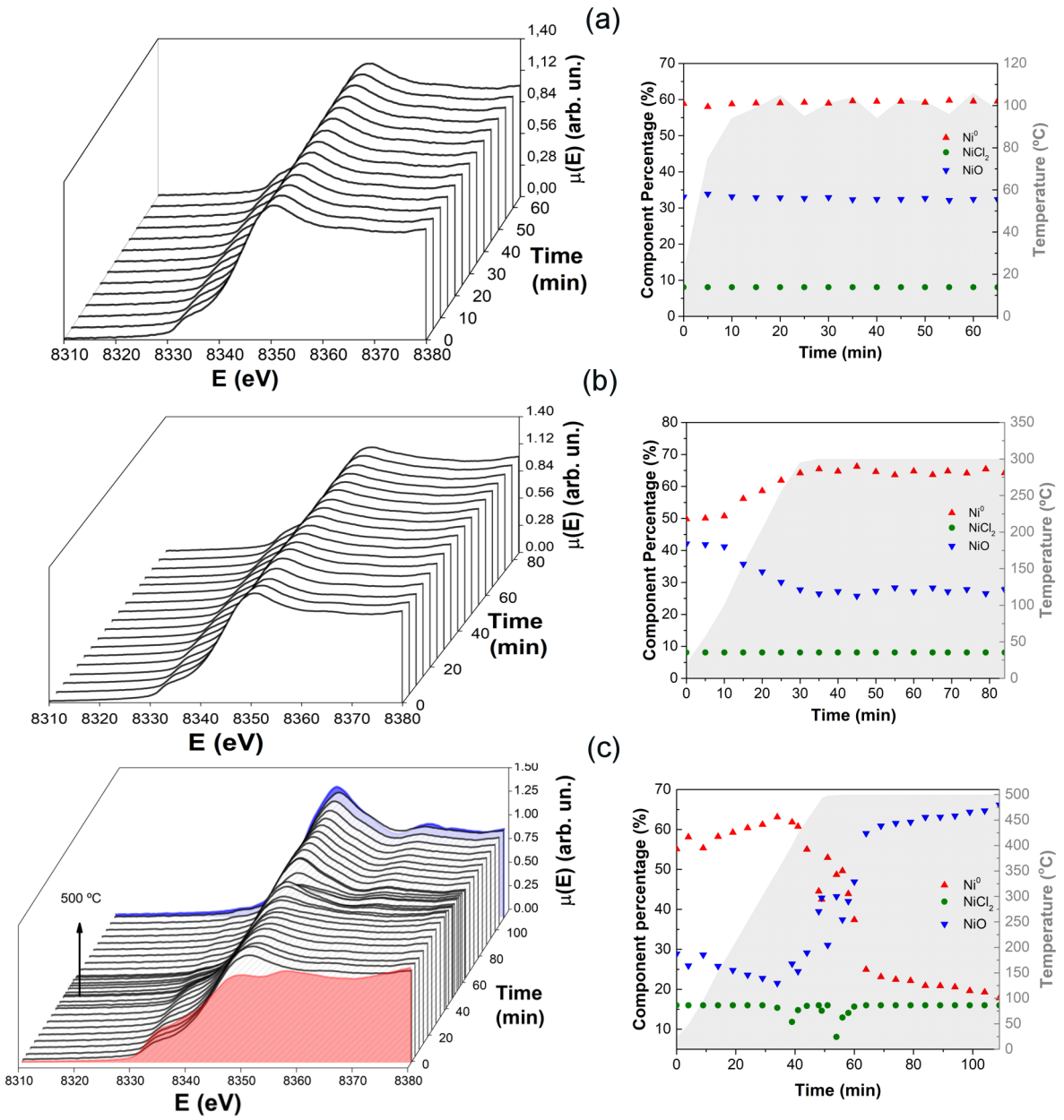

Figure 43 – In situ time-resolved XANES data of the Ni nanoparticles at the Ni K edge during heating treatment to (a) 100 ºC, (c) 300 ºC and (e) 500 ºC and the respective component percentages obtained by linear combination analysis as a function of time and the temperature measured inside the furnace. The red and blue filled-area XANES spectra represent the Ni^0 and NiO standards, respectively.

where A is the area between 500 nm and 800 nm after the reactions and A_0 before the reaction. These values are shown in Table 3. The high-temperature thermal treatment in the Ni nanoparticles induced a stronger degradation of methylene blue, where both Ni nanoparticles were heated to 300 ºC and 500 ºC and present the same degradation percentage of 26 % after 30 min of reaction. The worse activity is attributed to the Ni nanoparticles heated to 100 ºC, which is smaller than the value found for the as-prepared $Ni/SrTiO_3$ nanoparticles. To the best of our

knowledge, the Ni/$SrTiO_3$ nanoparticles were not applied yet for dye photodegradation reactions, but the results for the water-splitting reaction show that the presence of NiO is beneficial for the reaction [49, 52, 75, 146]. The formation of NiO observed in the in situ XAS measurements at 500 ºC indicates that the increase of the photodegradation efficiency is linked to the formation of NiO, probably due to the formation of a heterojunction [49]. However, this simple relation between NiO amount and photodegradation efficiency does not fully explain the results. One might wonder the reason that the degradation percentage of Ni300/$SrTiO_3$ and Ni500/$SrTiO_3$ samples are the same. Aiming to shed light on this point, the surface region of the nanoparticles was probed by XPS measurements.

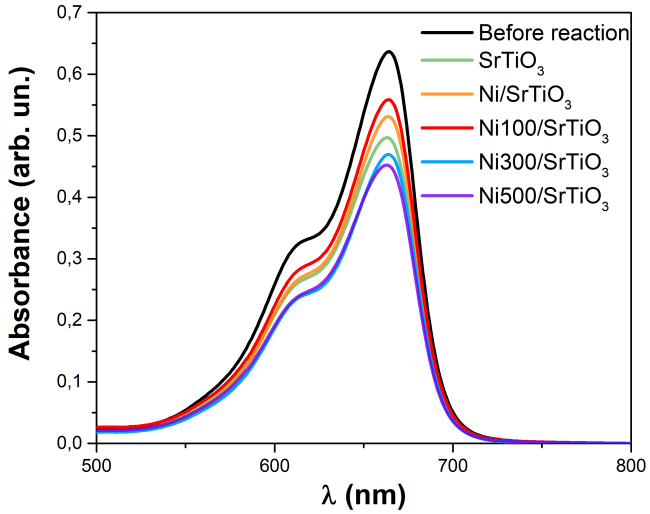

Figure 44 – UV-Vis measurements of methylene blue solution after 30 min of the photodegradation reaction for Ni/SrTiO3 nanoparticles.

Table 3 – Degradation results after 30 min of photodegradation reaction obtained from UV-Vis measurements.

Sample	**Degradation (%)**
$SrTiO_3$	20(2)
Ni/$SrTiO_3$	17(2)
Ni100/$SrTiO_3$	11(2)
Ni300/$SrTiO_3$	26(2)
Ni500/$SrTiO_3$	26(2)

The XPS long scans of $SrTiO_3$ and Ni nanoparticles are shown in Figure 45. It is observed the presence of Ni, Sr, Ti, O, and C elements, as expected. However, it is also possible to visualize the Ba impurity at the surface of $SrTiO_3$, as observed previously in the XRD data. Since the same batch of $SrTiO_3$ support was used in the full work, it does not influence the trend observed

for the photocatalytic degradation and it represents a systematic error. For the long scan of the Ni nanoparticles, the very small Cl contribution comes from the NaCl compound, which is a remnant of the synthesis procedure [131].

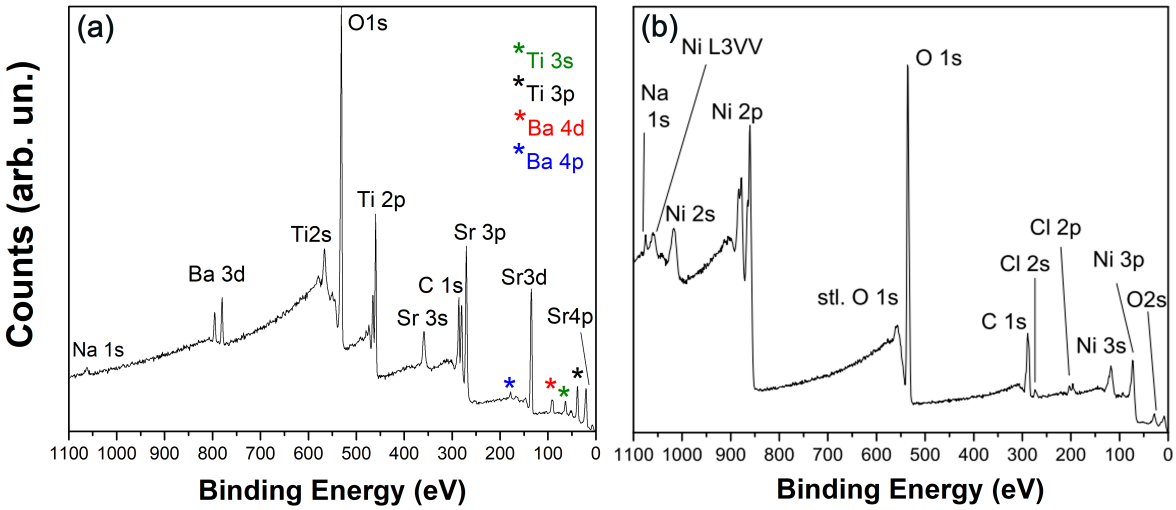

Figure 45 – XPS long scan of (a) $SrTiO_3$ and (b) as-prepared Ni nanoparticles.

The XPS spectra at the Ni $2p_{3/2}$ electronic region are shown in Figure 46 before and after the photodegradation reaction. The spectra are decomposed into three different components and their respective satellites. The Ni, Ni100 and Ni300 spectra present two main components assigned to NiO at 853.5 eV [147, 148] and $Ni(OH)_2$ at 856 eV [149, 150]. The presence of $Ni(OH)_2$ may come from individual entities located at the surface, then not forming long-range order to be detected in XRD. The $NiCl_2$ component is expected at 856.1 eV [151], but it is not observed in the XPS spectra, besides appearing in the XRD pattern of the as-prepared Ni nanoparticles. The $NiCl_2$ compound is probably not located at the surface region of the nanoparticles. This interpretation is also consistent with the XPS spectra at Ni $2p_{3/2}$ before supporting on $SrTiO_3$ (not shown here). The Ni^0 component is not observed after the support due to the low percentage near the surface, but it appears in the spectrum of the Ni nanoparticles before the support (not shown here). The increase of the heating temperature decreases the NiO amount until 300 ºC, and after thermal treatment at 500 ºC, a dramatic change is observed in the Ni $2p_{3/2}$ XPS spectrum. It is clear the appearance of a new component at 851.8 eV referent to Ni^0 [147, 152] besides the existence of the NiO component. Table 4 shows the percentages of the chemical components at the Ni $2p_{3/2}$ region. It is possible to observe that the NiO amount follows the same trend observed in the in situ XAS data with different absolute values since only the surface region is probed in these XPS measurements.

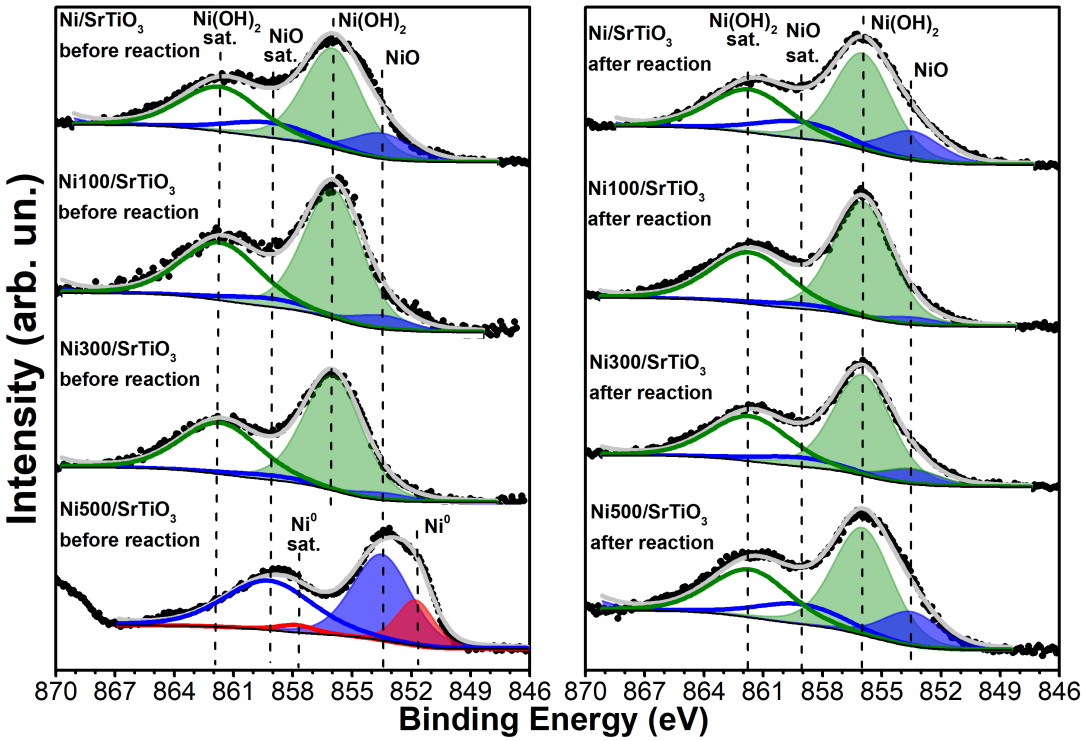

Figure 46 – XPS spectra at Ni $2p_{3/2}$ region before and after the photodegradation reactions for the $Ni/SrTiO_3$ nanoparticles.

After the photodegradation reactions, there are no significant changes on the Ni $2p_{3/2}$ XPS spectra for all cases, except for nanoparticles exposed to thermal treatment at 500 ºC. In this case, there is a suppression of the Ni^0 signal at the surface and the appearance of the $Ni(OH)_2$ component, evidencing overall oxidation of the Ni nanoparticles after the reaction. It should not be associated with atmosphere exposition after reaction and before XPS measurements since the nanoparticles treated at 500 ºC do not present these components before the photodegradation reaction. Therefore, the presence of $Ni(OH)_2$ and NiO can be explained through the NiO(s) + H_2O(l) $\rightarrow$ $Ni(OH)_2$(s) [146, 153] and Ni(s) + H_2O(l) $\rightarrow$ NiO(s) + H_2 (g) reactions occurring during the photodegradation of methylene blue. Furthermore, the coexistence of NiOOH and other similar binding energy compounds with the $Ni(OH)_2$ component cannot be discarded. Generally, the NiOOH component lies at slightly higher binding energies than the $Ni(OH)_2$ component due to the Ni^{+3} oxidation state [154, 155]. Some authors argue that, upon illumination, the formation of NiOOH from $Ni(OH)_2$ is possible [146]. The pH of the solution immediately before light illumination was measured to be around 5, which turned to 6 after 30 min of reaction. The Pourbaix diagram of Ni enables the determination of the Ni chemical components as a function of pH and electrode potential [156], and stable phases of Ni^{2+}, NiO, NiOOH or $Ni(OH)_2$ are possible at this pH, depending on the molar concentration [156]. Then, the $Ni(OH)_2$

compound comes probably due to the pH of the solution.

Table 4 – Ni chemical components percentage obtained from the XPS analysis

Sample	$Ni(OH)_2$ %	NiO %	Ni %
Ni/$SrTiO_3$ before	77	23	0
Ni/$SrTiO_3$ after	73	26	1
Ni100/$SrTiO_3$ before	89	11	0
Ni100/$SrTiO_3$ after	93	7	0
Ni300/$SrTiO_3$ before	93	7	0
Ni300/$SrTiO_3$ after	85	15	0
Ni500/$SrTiO_3$ before	0	81	19
Ni500/$SrTiO_3$ after	73	27	0

Figure 47 shows the XPS spectra at the Sr 3d electronic region and Table 5 shows the percentage of each component obtained from the fitting result at Sr 3d XPS region. The XPS spectra before the photodegradation reaction show the presence of two main components at 132.5 eV and 133.4 eV, which are associated with $SrTiO_3$ [157, 158] and $SrCO_3$, respectively. The presence of $SrCO_3$ is in accordance with the XRD pattern (Figure 37). Interestingly, there is a further component with the same FWHM of the $SrTiO_3$ component observed at low binding energy for Ni/$SrTiO_3$ nanoparticles before the photodegradation reaction. This component can be assigned to negatively charged Sr atoms in $SrTiO_3$, there is evidence for a charge transfer process in this case.

After the photodegradation reactions, there is an overall increase of the $SrCO_3$ component and a decrease of the $SrTiO_3$ one in comparison to the corresponding case before the photodegradation reaction. Curiously, a new component at low binding energy appears after the photodegradation reaction, except for the Ni500/$SrTiO_3$ nanoparticles. This component is interpreted as a SrO_x oxygen deficient phase [159]. Since the reaction $SrCO_3(s) \rightarrow SrO$ (fcc) + CO_2 occurs between 900 K and 1000 K [160], the appearance of SrO_x may come from the surface reconstruction of the $SrTiO_3$ compound. The observation of $SrTiO_3$ surface reconstruction to a surface with outermost SrO_x layers was observed in the literature during heating treatment at 550 ºC in an O_2 gas atmosphere [161, 162]. In the present case, the $SrTiO_3$ sample (without Ni) does not present this new component after the photodegradation reaction, indicating that the Ni nanoparticles affect the surface reconstruction. The UV-light irradiation, which induces localized heating, along with a weak acid (or even non-acid [163]) aqueous environment, could induce surface reconstruction as well. The proposed reconstruction occurs through $SrTiO_3 \rightarrow SrO_x$ transformation, which explains the smaller amount of $SrTiO_3$ component after the photodegradation

reaction in comparison to before reaction.

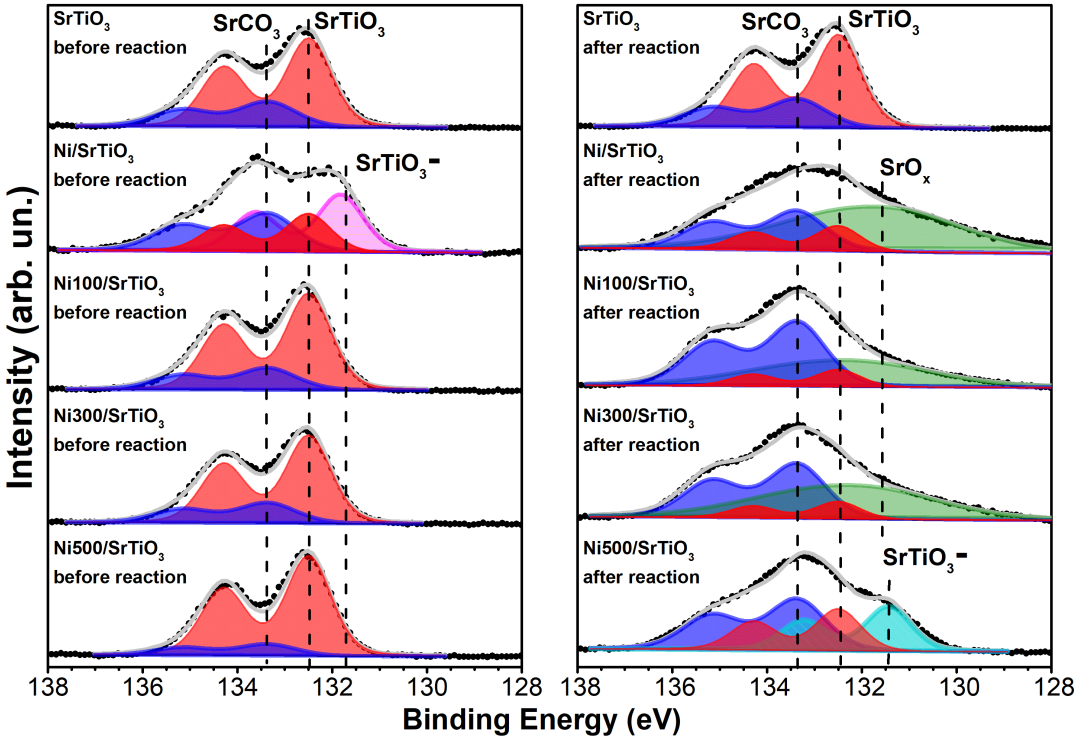

Figure 47 – XPS spectra at Sr 3d region before and after the photodegradation reactions for the $Ni/SrTiO_3$ nanoparticles.

One could argue that another possibility of interpretation for the low binding energy components would be a combination between initial-state and final-state screening effects by, for example, the formation of Sr-C bonds. By decreasing the average number of cationic sites (Sr^{+2}) at the oxide structure, Sr 3d would be affected by a weaker electrostatic potential, which lowers the electron binding energy. However, this effect is unlikely to predominate in $SrTiO_3$, as discussed by Van der Heide *et al.* [164]. A $SrTiO_3^-$ component appears in the Sr 3d XPS spectrum of $Ni500/SrTiO_3$ nanoparticles after the photodegradation reaction as well. In this case, it may be directly associated with the oxidation of methylene blue during the photodegradation reaction. It is indicative of the heterojunction formation since the Ni atoms are oxidized in this sample after the photodegradation reaction (see Figure 46). These hypotheses of surface's reconstruction, charge transfer and oxidation of methylene blue molecule should be strengthened by analyzing the Ti 2p XPS spectra.

The XPS spectra at the Ti $2p_{3/2}$ electronic region are shown in Figure 48. Table 5 shows the percentage of each component obtained from the fitting result at Ti $2p_{3/2}$ XPS region. In general, the XPS spectra of the nanoparticles before photodegradation reaction present a single

component at 457.7 eV associated with $SrTiO_3$ [165]. However, there is a further component at high binding energy in the $Ni/SrTiO_3$ nanoparticles before the photodegradation reaction. This component meets the low binding energy component at Sr 3d XPS spectrum of the same sample and it is associated with a charge transfer process from Ti to Sr atoms at the surface of the $SrTiO_3$ nanoparticles.

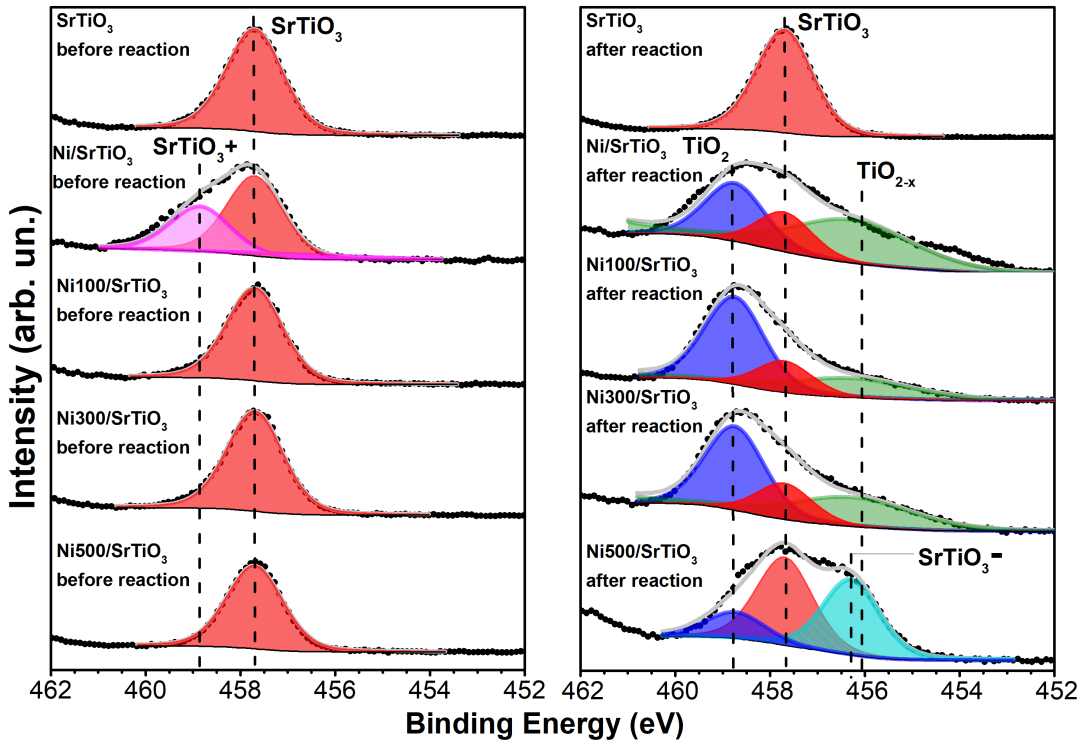

Figure 48 – XPS spectra at Ti $2p_{3/2}$ region before and after the photodegradation reactions for the $Ni/SrTiO_3$ nanoparticles.

After the photodegradation reactions, the major component of the Ti $2p_{3/2}$ XPS spectra turns into a new component appearing at 458.8 eV, which is interpreted as TiO_2 [166]. Furthermore, a new component is also evident at low binding energy and it is associated with TiO_{2-x} [167, 168, 169]. It is well known the existence of two possible surface terminations of $SrTiO_3(100)$ with SrO and TiO_2 in the outermost layer [170]. Then, the presence of TiO_2 after the photodegradation reaction agrees with the presence of SrO_x at Sr 3d XPS spectra in the same condition, corroborating the interpretation of surface reconstruction during the photocatalytic reaction. The presence of TiO_{2-x} comes from O vacancies formed in the TiO_2 outermost layer, i.e., the most superficial atomic layers of many $SrTiO_3$ nanoparticles change into segregated Ti-O or Sr-O compounds. It is also known that an HNO_3 etching of $SrTiO_3$ nanocrystals induces a surface reconstruction to TiO_2 outermost layers [161, 162]. Then, an environment with a weak

acidity such as in the present work ($5 < \text{pH} < 6$) may induce the surface reconstruction. Again, the surface reconstruction is not observed after the reaction in the $SrTiO_3$ sample (without the Ni nanoparticles). Although the Ni $2p_{3/2}$ XPS region does not present any clear component related to some type of interaction with the support, the surface reconstruction must be induced by the presence of the Ni nanoparticles, the methylene blue solution and/or the UV light. For the Ni500/$SrTiO_3$ nanoparticles after the photodegradation reaction, a new low binding energy component appears. This is in agreement with the corresponding Sr 3d XPS spectrum, a negatively charged $SrTiO_3$, which represents further evidence of the heterojunction formation and the oxidation of methylene blue during photodegradation reaction occurs at the $SrTiO_3$ support. The presence of a TiO_2 component in the Ti $2p_{3/2}$ XPS spectrum of the Ni500/$SrTiO_3$ sample may indicate the surface reconstruction is also present in this sample but in a less extent. From the XPS data, it is not possible to discard the presence of the SrO_x and TiO_{2-x} components overlapping those present in the Sr 3d and Ti $2p_{3/2}$ XPS spectra measured of this sample. However, this is not the main effect since these single components are not able to fit the XPS spectra and the $SrTiO_3^-$ represents the main contribution.

The XPS spectra at the O 1s electronic region are shown in Figure 49. Before the reaction, all samples show the $SrTiO_3$ and $SrCO_3$ components, as expected [157, 171]. It is hard to identify the NiO component located at around 529 eV [148], which is overlapping with the $SrTiO_3$ component, due to the low concentration of Ni nanoparticles in the sample. The Ni/$SrTiO_3$, Ni100/$SrTiO_3$ and Ni300/$SrTiO_3$ samples also present characteristic C-O or C=O components [172] coming from either synthesis procedure of the Ni nanoparticles or exposure of the Ni nanoparticles to the atmosphere. This last option is unlikely because the Ni500/$SrTiO_3$ sample also had contact with the atmosphere and does not show this type of component. The decrease in the intensity of this component with the increase of the temperature used in the thermal treatment shows it comes as a remnant from the synthesis procedure and it decomposes entirely when reaching 500 ºC. The Ni/$SrTiO_3$ sample also presents a further component at 530.5 eV, which is related to the charge transfer process observed in the Sr 3d and Ti $2p_{3/2}$ XPS region. In this case, there is a charge transfer from the TiO_6 environment atoms to the Sr atoms.

After the reaction, the $SrTiO_3$ sample shows a new component interpreted as physisorbed OH radicals [173]. The slight increase of the C-O components after reaction may be due to coking of the surface by the subproducts of the photodegradation reaction. The Ni/$SrTiO_3$, Ni100/$SrTiO_3$ and Ni300/$SrTiO_3$ samples after the photodegradation reaction present a new

component attributed to surface reconstruction components [171], as observed in Sr 3d and Ti 2p XPS regions. Note that these SrO_x and TiO_{2-x} components fully hide the $SrTiO_3$ component at O 1s XPS spectra.

Table 5 – Sr and Ti chemical components percentage obtained from the XPS analysis

Region	**Sr 3d**				**Ti $2p_{3/2}$**				
Sample	$SrCO_3$ %	$SrTiO_3$ %	$SrTiO_3^-$ %	SrO %	TiO_2 %	$SrTiO_3^+$ %	$SrTiO_3$ %	TiO_{2-x} %	$SrTiO_3^-$ %
$SrTiO_3$	26	74	0	0	0	0	100	0	0
$SrTiO_3$ after	28	72	0	0	0	0	100	0	0
Ni/$SrTiO_3$ before	33	27	40	0	0	37	63	0	0
Ni/$SrTiO_3$ after	32	21	0	48	28	0	23	49	0
Ni100/$SrTiO_3$ before	22	78	0	0	0	0	100	0	0
Ni100/$SrTiO_3$ after	51	11	0	38	56	0	19	25	0
Ni300/$SrTiO_3$ before	23	77	0	0	0	0	100	0	0
Ni300/$SrTiO_3$ after	42	11	0	47	47	0	19	33	0
Ni500/$SrTiO_3$ before	13	87	0	0	0	0	100	0	0
Ni500/$SrTiO_3$ after	43	28	30	0	15	0	46	0	39

Again, the Ni500/$SrTiO_3$ sample after reaction does not present evidence for this component but it is observed the presence of H_2O [173] due to the component located at 535.5 eV. Of course, this component may be superposed in the other samples since it is located between the C-O and SrO_x, TiO_{2-x} components. A recent study on Pt/$SrTiO_3$ nanoparticles [174] has shown that the spillover effect of the H_2 due to the Pt atoms creates O vacancies at the surface of $SrTiO_3$ even at 150 ºC. Theoretically, the Ni^0 component supported on $SrTiO_3$ can split H_2O to form H_2 molecules [49], which in turn could show a spillover effect due to the Ni^0 component, and that would be responsible for the surface reconstruction effect. It could explain the reason behind not observing the surface reconstruction in the $SrTiO_3$ sample and, if observed, only a small amount of surface reconstruction in Ni500/$SrTiO_3$ since the Ni^0 fraction is small in this case, but it should be investigated in details in a further work.

The XPS results allow shedding light on the atomic mechanism of methylene blue photodegradation reaction. Two entirely different mechanisms take place to explain the results obtained. One mechanism is valid for the Ni500/$SrTiO_3$ sample and it is named Model A (from thermal treatment "at" 500 ºC) and the other is valid for Ni nanoparticles exposed to a maximum temperature of 300 ºC, hereafter named Model B (from thermal treatment "below" 500 ºC). Figure 50 resumes the models proposed. In the literature [146, 75, 77], it is documented that the combination of Ni^0 and NiO components increases the hydrogen production from the water-splitting reaction in comparison to the pristine $SrTiO_3$ sample. In the present work, for Model B the highest Ni^0 amount the best photodegradation efficiency was observed. The $SrTiO_3$(100) surface presents the SrO_x and TiO_{2-x} terminations and it can dissociate water easily in its steps

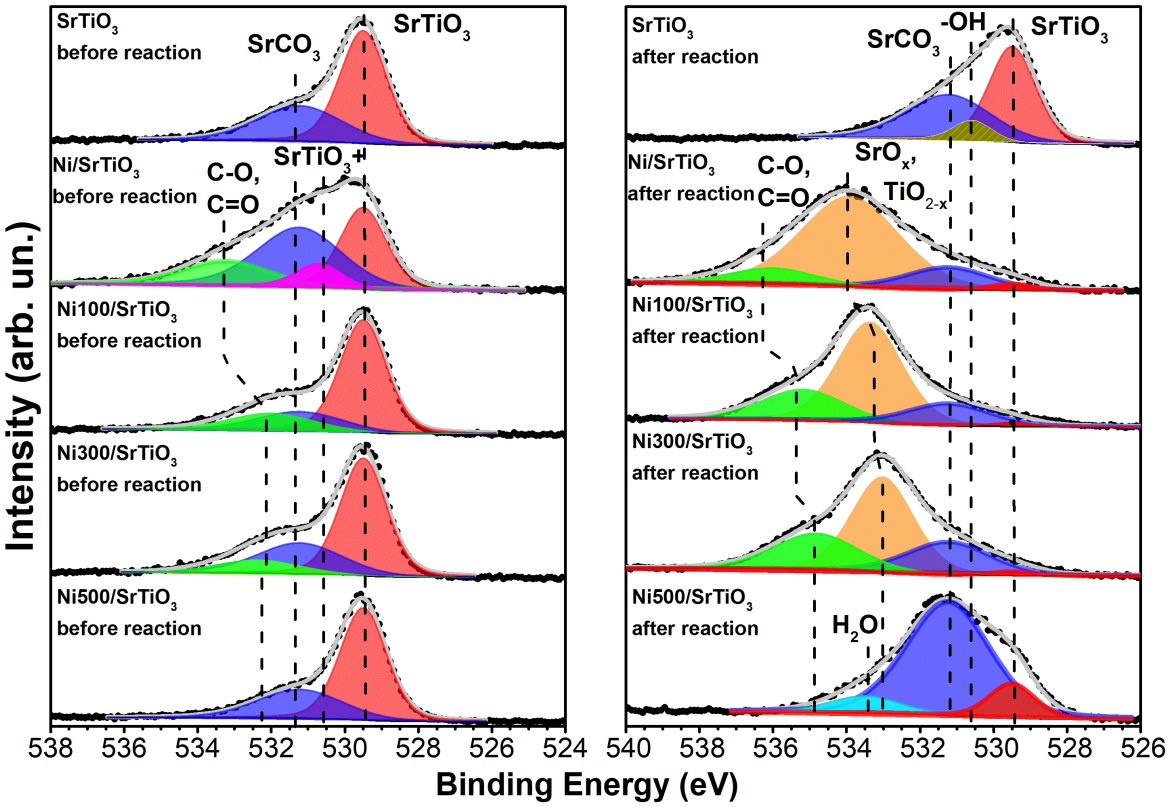

Figure 49 – XPS high resolution spectra at O 1s region before and after the photodegradation reactions for the Ni/$SrTiO_3$ nanoparticles.

[64], thus favoring the mechanism of radical formation (see discussion in 1.3). Nonetheless, Model A does not consider the radical formation but a direct mechanism for methylene blue photodegradation. It is proposed the formation of the NiO/$SrTiO_3$ heterojunction, that improves the photodegradation of methylene blue. While the $SrTiO_3$ reduces (as in the $SrTiO_3^-$ component), the NiO nanoparticles oxidize even further during the reaction. It means there is a charge transfer from NiO to $SrTiO_3$ for electrons and in the opposite direction for holes, as expected from the electric field formed in the NiO/$SrTiO_3$ heterojunction (see Figure 9). Then, the heterojunction must decrease the electron-hole pair recombination, thus increasing the photocatalytic efficiency. UV-Vis spectroscopy measurements (not shown here) evidence that the optical band gap does not change after supporting the NiO nanoparticles.

The calculated projected density of states after structural relaxation for the $SrTiO_3$ slab systems is presented in Figure 51. The energy gap (1.1 eV) of the TiO_2 terminated $SrTiO_3$ slab is reduced in comparison to bulk $SrTiO_3$ (1.9 eV). However, it does not occur for SrO, where the gap value is essentially the same as in bulk. These values are in agreement with other works in the literature even if using GGA-PBE [79]. The reason for the gap reduction in the TiO_2

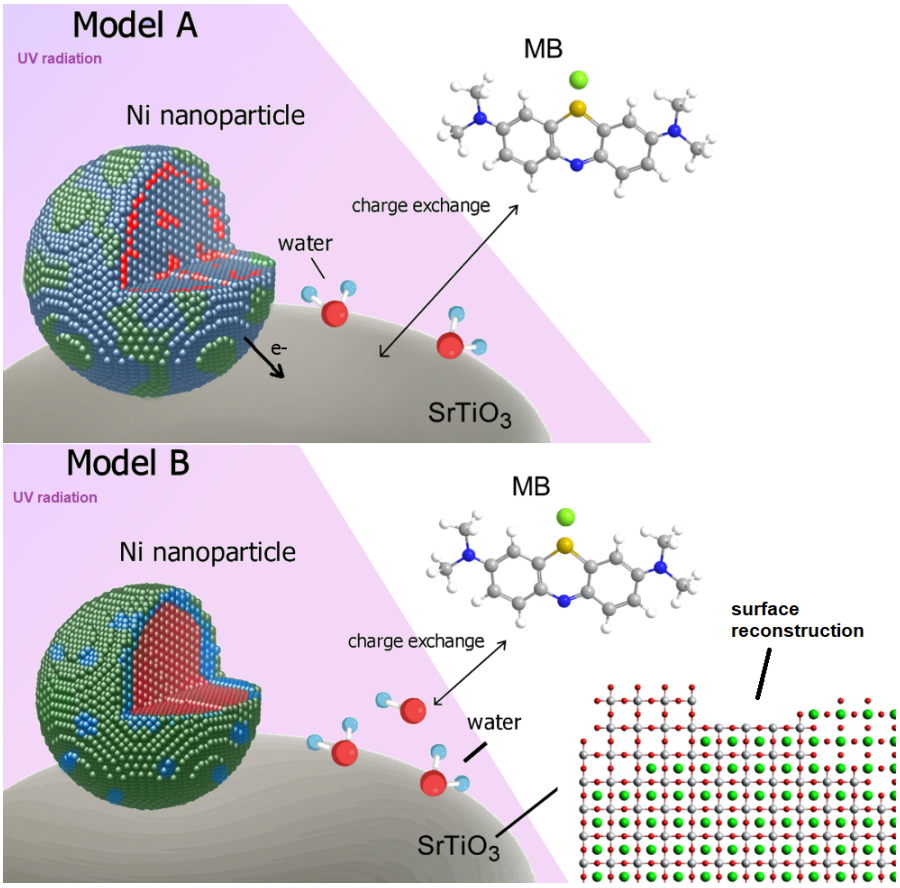

Figure 50 – Two models proposed for the photodegradation reactions with the Ni/$SrTiO_3$ nanoparticles. The green, blue and red spheres at the nanoparticles represent the $Ni(OH)_2$, NiO and Ni^0 compounds, respectively.

terminated surface is the presence of dangling bonds composed by the p_y and p_z orbitals of O perpendicular to the surface [63]. It is also observed that, even if the band edges are composed by O 2p and Ti 3d levels, the SrO termination slab has a slight increase of the Sr 4p levels at the conduction band.

Figures 52 and 53 compare the charge density of the slab systems before and after the support of a 4 atom Ni cluster. It can be seen in Figure 52 (b) that the SrO terminated $SrTiO_3$ (001) surface shows a slight shift of the surface O atoms positions away from the Ni cluster and closer to the Sr peripheral atoms. In this case, the charge density changes slightly around the Sr-O bonding adjacent to the Ni cluster, where the Löwdin charge at the p orbital of Sr increases (atoms 1 and 2 in Figure 53 (a) and (b)) and that of p orbitals of the adjacent O atoms decreases. The charge density at the Ni atoms does not present any change. Even with such a slight change in the charge density, it can potentially bring insight to the components that appeared in the XPS spectra of the Ni/$SrTiO_3$ sample. The increase in charge density around the surface Sr atoms may explain the component that appears at lower binding energy at the Sr 3d XPS region (Figure

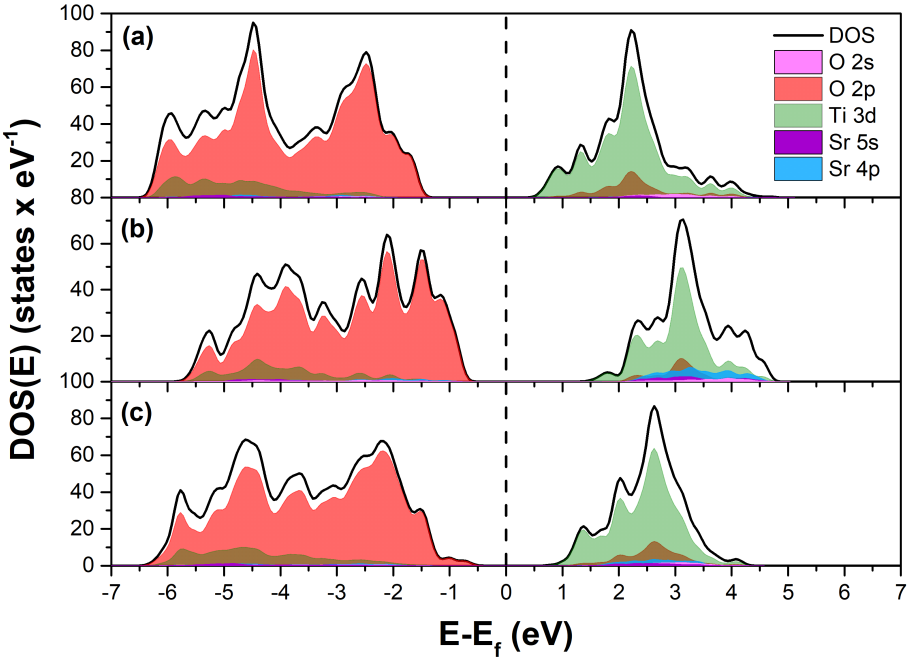

Figure 51 – Density of states of the $SrTiO_3$ (a) bulk and (001) slabs with (b) SrO termination and (c) TiO_2 termination.

47), while the decrease of the charge density around the O atoms can explain the component that appears at higher binding energy at the XPS O 1s region (Figure 49). Of course, the real case presents a variety of surface terminations but these DFT results help to understand possible trends. It is interesting to note that this charge transfer is not observed in the TiO_2 terminated $SrTiO_3$ system shown in Figure 53 (b) and (d). However, a bonding is formed between the Ni cluster and the surface Ti atoms, different from the SrO terminated $SrTiO_3$ (001) surface.

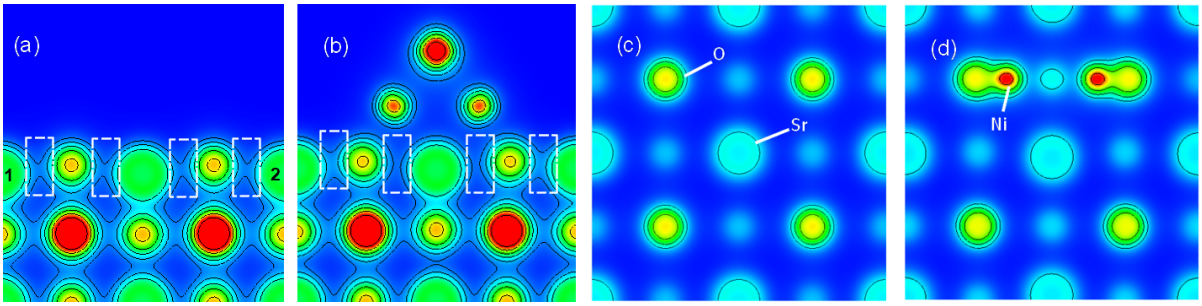

Figure 52 – Charge density of SrO terminated $SrTiO_3$ surface (a) lateral view before Ni inclusion, (b) lateral view after Ni inclusion, (c) top view before Ni inclusion and (d) top view after Ni inclusion.

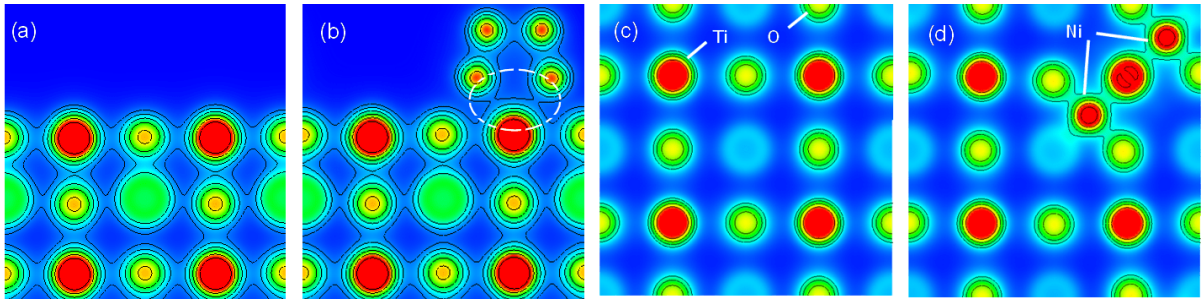

Figure 53 – Charge density of TiO_2 terminated $SrTiO_3$ surface (a) lateral view before Ni inclusion, (b) lateral view after Ni inclusion, (c) top view before Ni inclusion and (d) top view after Ni inclusion.

4.2 Ion irradiated $SrTiO_3$ nanoparticles

The SRIM code [123] was used to estimate the amount of vacancies created during the ion irradiation process. A simulation with 500 Au ions at 16 MeV impinging over a 0.48 g/cm^3 layer of $SrTiO_3$ was carried out, and the results can be visualized in Figure 54. The density was roughly estimated during powder deposition in the sample holder. In this configuration, approximately 57000 vacancies/ion were produced, where around 54 % are O vacancies. Without considering the recoil of the lattice atoms, the irradiation presents a value of around 47000 vacancies/ion created. It is only an approximation since Au ions are implanted in the sample holder and the simulation results show a maximum depth of only 20 μm. Decreasing the $SrTiO_3$ density used in the calculations by one order of magnitude to 0.03 g/cm^3, the simulation results in the decrease of the O vacancies/ion to about 20000 vacancies/ion. Since the density of the $SrTiO_3$ nanoparticle powder is hard to be determined in this case, the O vacancies/ion created may lie below 30000 vacancies/ion. It is important to stress out that SRIM does not provide information about dynamic changes. In the real experiment, the range is shifted if compared to the calculated one.

The XRD patterns of the ion irradiated $SrTiO_3$ nanoparticles are shown in Figure 55. All the ion irradiated samples show Bragg reflections in the same position of pristine $SrTiO_3$, indicating that these Au^{7+} fluences do not induce phase transition. Table 6 presents the parameters obtained from Rietveld refinement analysis. No significant changes in the crystallite size, $SrTiO_3$ amount, lattice parameter (a) and strain are observed between the samples.

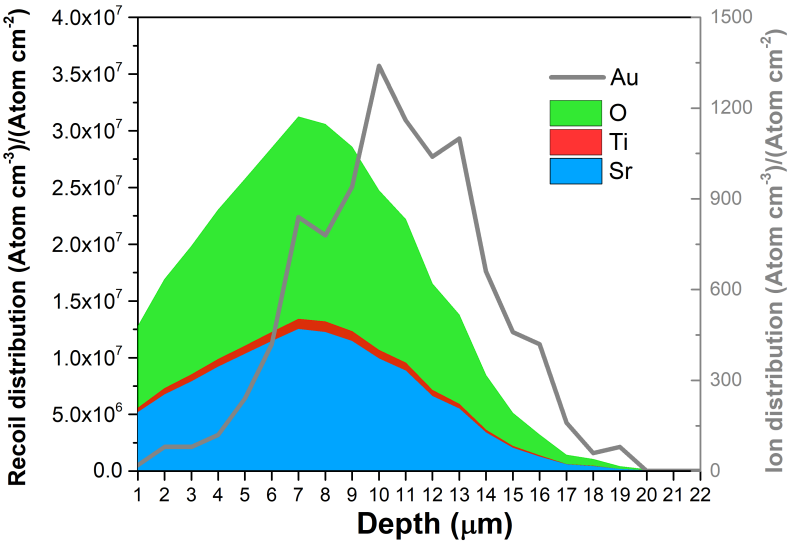

Figure 54 – Full cascades of the ion irradiation simulation on a 0.48 g/cm^3 $SrTiO_3$ layer where it is shown the Au ions range distribution and lattice atoms recoil distribution.

Table 6 – Structural parameters obtained from Rietveld refinement results.

Sample	**$SrTiO_3$ (%)**	**Size (nm)**	**Strain (%%)**	**a (Å)**
$SrTiO_3$	$93.0(0.8)$	28	2	3.907
$SrTiO_3$ 1E13	$92.2(0.9)$	29	4	3.907
$SrTiO_3$ 5E13	$91.9(0.9)$	28	4	3.908
$SrTiO_3$ 1E14	$91(1)$	28	3	3.908

UV-Vis Spectroscopy in reflectance mode (Figure 56) measurements were made for these samples. By transforming the reflectance into the Kubelka Munk function, $F(R)$, and analyzing the Tauc plot (Figures (b) and (c)), it was possible to estimate that both the direct and indirect band gaps did not change after ion irradiation, as presented in Table 7.

Table 7 – Band gap values obtained from UV-Vis measurements in reflectance mode

Sample	**Indirect gap value (eV)**	**Direct gap value (eV)**
$SrTiO_3$	$2.95(0.09)$	$3.22(0.03)$
$SrTiO_3$ 1E13	$2.96(0.08)$	$3.19(0.05)$
$SrTiO_3$ 5E13	$2.95(0.08)$	$3.19(0.06)$
$SrTiO_3$ 1E14	$3.00(0.03)$	$3.24(0.04)$

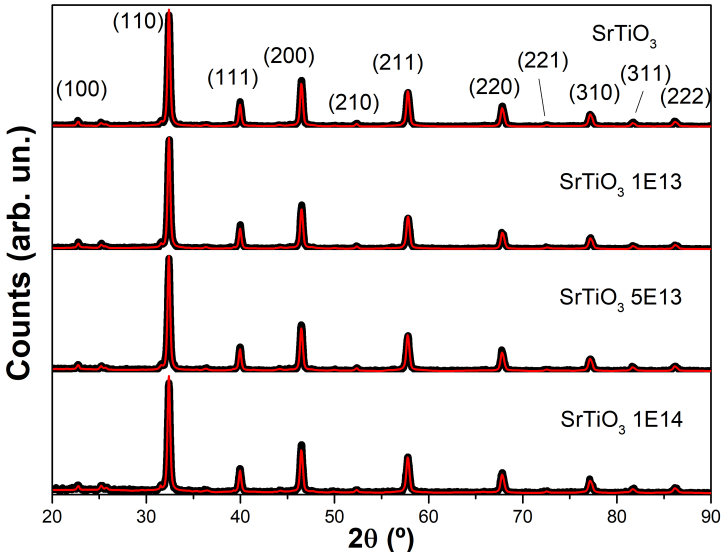

Figure 55 – XRD patterns of ion irradiated $SrTiO_3$ nanoparticles. The black points represent the experimental data while the red lines represent the Rietveld refinement result.

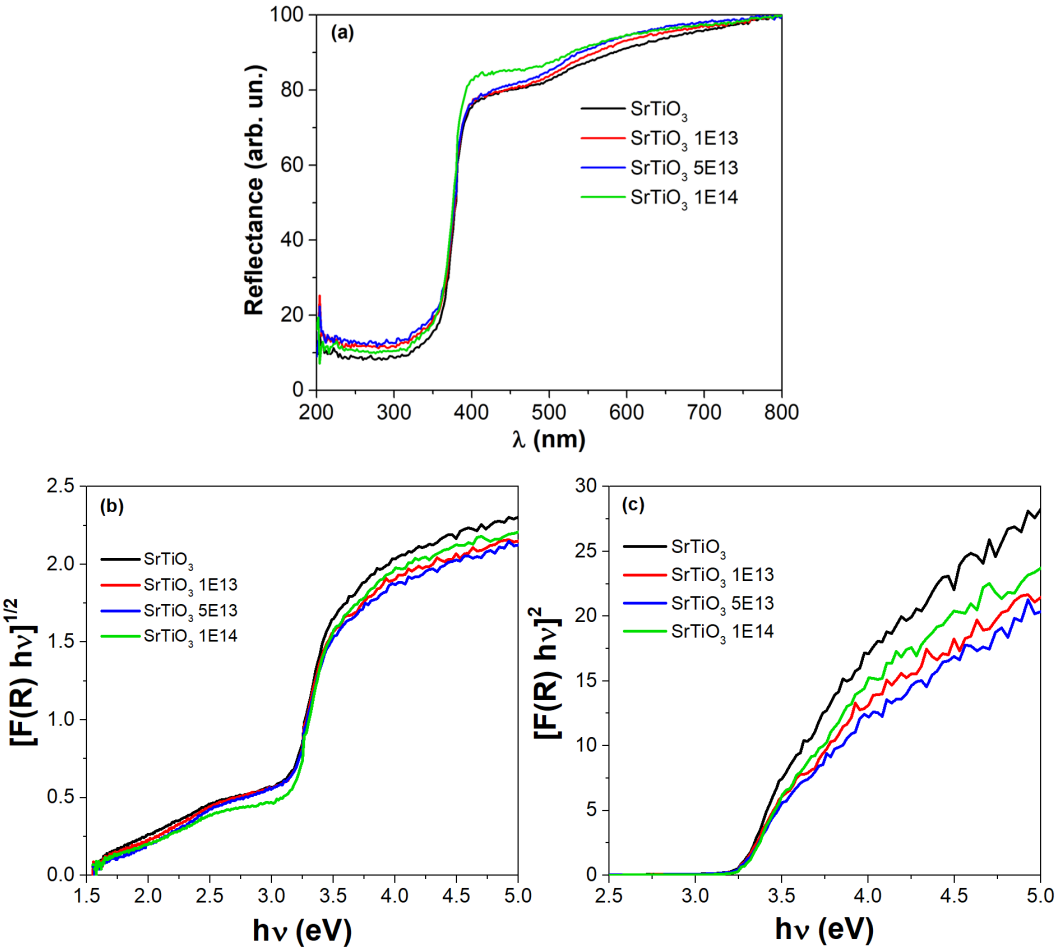

Figure 56 – UV-Vis measurements of the ion irradiated samples: (a) reflectance mode, (b) Tauc plot with indirect band gap parameter and (c) Tauc plot with direct band gap parameter.

The photodegradation results with the 365 nm LED lamp can be visualized by the UV-

Vis spectra in Figure 57 measured after (a) 2 h and (b) 3 h of reaction. The photodegradation percentages are shown in Table 8. The improvement in photodegradation results due to ion irradiation on $SrTiO_3$ nanoparticles is evident. It occurs due to the atomic vacancy creation, which enables the adsorption of methylene blue molecules or radicals with the consequent photodegradation of the molecules. Again, the blue-shifts observed in the spectra may be related to the formation of methylene blue dimers made possible by the longer time of reaction. The ion irradiated samples present similar photodegradation results considering the uncertainty associated. For comparison purposes, the best Ni supported on $SrTiO_3$ sample ($Ni500/SrTiO_3$) for photodegradation of methylene blue was used with the LED lamp and the same experimental setup of ion irradiated samples. The UV-Vis spectra after 3 h reaction show a photodegradation of $32(2)$ %. This result is better than the case of $SrTiO_3$ nanoparticles, as expected from the results obtained with the Hg lamp. However, the ion irradiation method is more efficient than heating the Ni nanoparticles to high temperatures for photodegradation of methylene blue. It shows, in a pioneering way, a new proposal for improving the photodegradation efficiency. To the best of our knowledge, there is no study in the literature aiming to improve the photocatalytic activity by high energy ion irradiation of $SrTiO_3$. Overall, the photodegradation results with LED lamp are worse than those with Hg lamp, even for longer reaction times. It occurs because the LED lamp emits radiation closer to the visible region instead of UV region of the electromagnetic spectrum like the Hg lamp. It must be stressed out that, besides the samples show a decreased absorption of light with the LED lamps, this energy allows probing almost directly the photocatalytic activity of the nanoparticles without the influence of dye-sensitizing mechanisms.

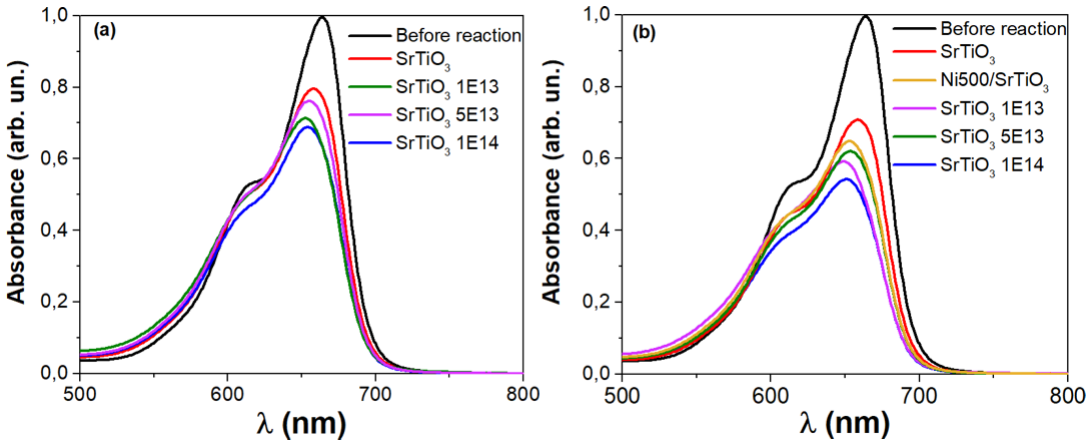

Figure 57 – UV-Vis measurements after (a) 2 h and (b) 3 h photodegradation reactions of the ion irradiated $SrTiO_3$ samples.

Table 8 – Photodegradation results obtained from the UV-Vis measurements for the ion irradiated $SrTiO_3$ nanoparticles.

Sample	**2 h photodegradation (%)**	**3 h photodegradation (%)**
$SrTiO_3$	13(2)	25(2)
$SrTiO_3$ 1E13	27(2)	38(2)
$SrTiO_3$ 5E13	19(2)	36(2)
$SrTiO_3$ 1E14	27(2)	41(2)

The XPS long scan spectra after ion irradiation (not shown here) do not show the presence of Au, as expected due to the low amount of Au implanted. Figure 58 shows the XPS spectra at the Sr 3d electronic region before and after the photodegradation reactions. It is possible to observe the presence of two main components at 132.3 eV and 133.1 eV, interpreted as $SrTiO_3$ and $SrCO_3$, respectively [157, 158]. The FWHM of the different components was averaged between the different samples after the initial fitting procedure. The chemical component fraction of each component is presented in Table 9. The ion irradiation does not promote a perceptible change in the Sr 3d electronic region for the $SrTiO_3$ sample. After the photodegradation reaction, the $SrCO_3$ component amount increases slightly in the $SrTiO_3$ sample, which reproduces the previous XPS. The intensity of this same component shows a pronounced increase in the ion irradiated samples after reaction, which is more evident for the 1×10^{13} and 5×10^{13} at/cm^2 irradiation doses. The increase of this component after the photodegradation reaction was also observed in the Ni/$SrTiO_3$ nanoparticles for Ni nanoparticles heated in different temperatures.

Table 9 – Chemical component percentages of the irradiated nanoparticles from XPS analysis at Sr 3d, Ti $2p_{3/2}$ and O 1s electronic regions. VR stands for the vacancy-related components.

	Sr 3d		**Ti $2p_{3/2}$**		**O 1s**		
Sample	$SrCO_3$, VR	$SrTiO_3$	VR	$SrTiO_3$	C-O, OH	VR, $SrCO_3$	$SrTiO_3$
$SrTiO_3$ before	15	85	0	100	3	30	67
$SrTiO_3$ after	20	80	0	100	2	31	67
$SrTiO_3$ 1E13 before	15	85	0	100	0	28	72
$SrTiO_3$ 1E13 after	41	59	33	67	5	39	56
$SrTiO_3$ 5E13 before	14	86	0	100	2	31	67
$SrTiO_3$ 5E13 after	42	58	44	56	8	47	46
$SrTiO_3$ 1E14 before	15	85	0	100	5	32	63
$SrTiO_3$ 1E14 after	24	76	15	85	7	35	59

Figure 59 shows the XPS spectra at the Ti $2p_{3/2}$ electronic region. Before the photodegradation reaction, the XPS spectra presents a single component at 457.6 eV, which is assigned to $SrTiO_3$. Again, the ion irradiation is not sufficient to modify the overall surface of the nanoparticles. After the reaction, however, a new component appears at around 458.2 eV for the XPS

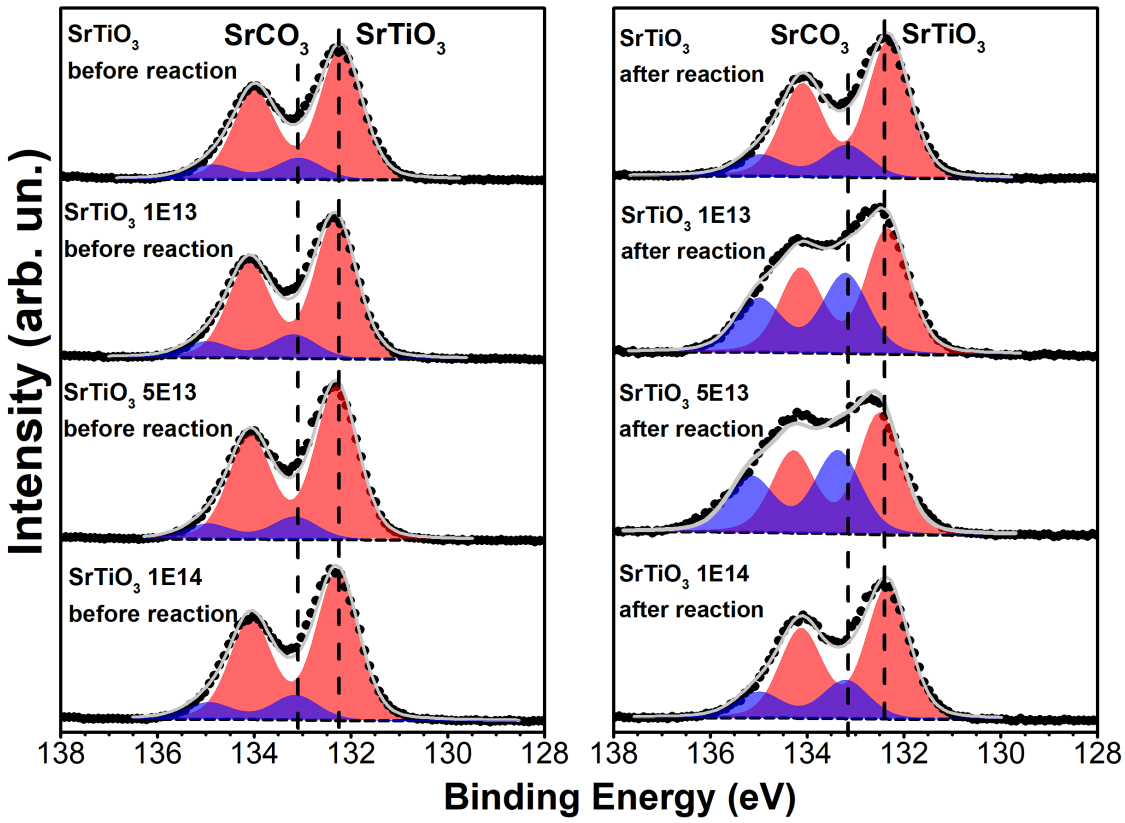

Figure 58 – Sr 3d XPS spectra before and after the photodegradation reaction for the ion irradiated $SrTiO_3$ nanoparticles.

spectra of the irradiated samples. This component is shifted $+0.6$ eV in comparison to the $SrTiO_3$ component. It cannot be assigned as TiO_2, like in the Ni/$SrTiO_3$ samples, because, in that case, the TiO_2 component after the photodegradation reaction shifted $+1.1$ eV. The widening of the Ti 2p region was related in the literature to the creation of vacancies for $SrTiO_3$ in a $NaBH_4$ environment [8]. The authors argue that the shift in the Fermi energy due to the presence of atomic vacancies induces a $+0.4$ eV shift in the overall Ti 2p and Sr 3d electronic regions of $SrTiO_3$, which is very close to the value observed in the present work. The presence of such component in the Sr 3d electronic region is not seen because it is overlapping with the $SrCO_3$ component. In fact, there is a clear correlation between the increase of the vacancy-related component in Ti 2p with the increase in the $SrCO_3$ component in Sr 3d XPS region, both after the photodegradation reaction (see Table 9). The O 1s XPS region interpretation should corroborate this idea.

Figure 60 shows the XPS spectra at the O 1s electronic region. The XPS spectra before photodegradation reaction present two components at 528.8 eV and 530.3 eV, which are attributed to $SrTiO_3$ and $SrCO_3$, respectively [157, 171]. After the photodegradation reaction, a new

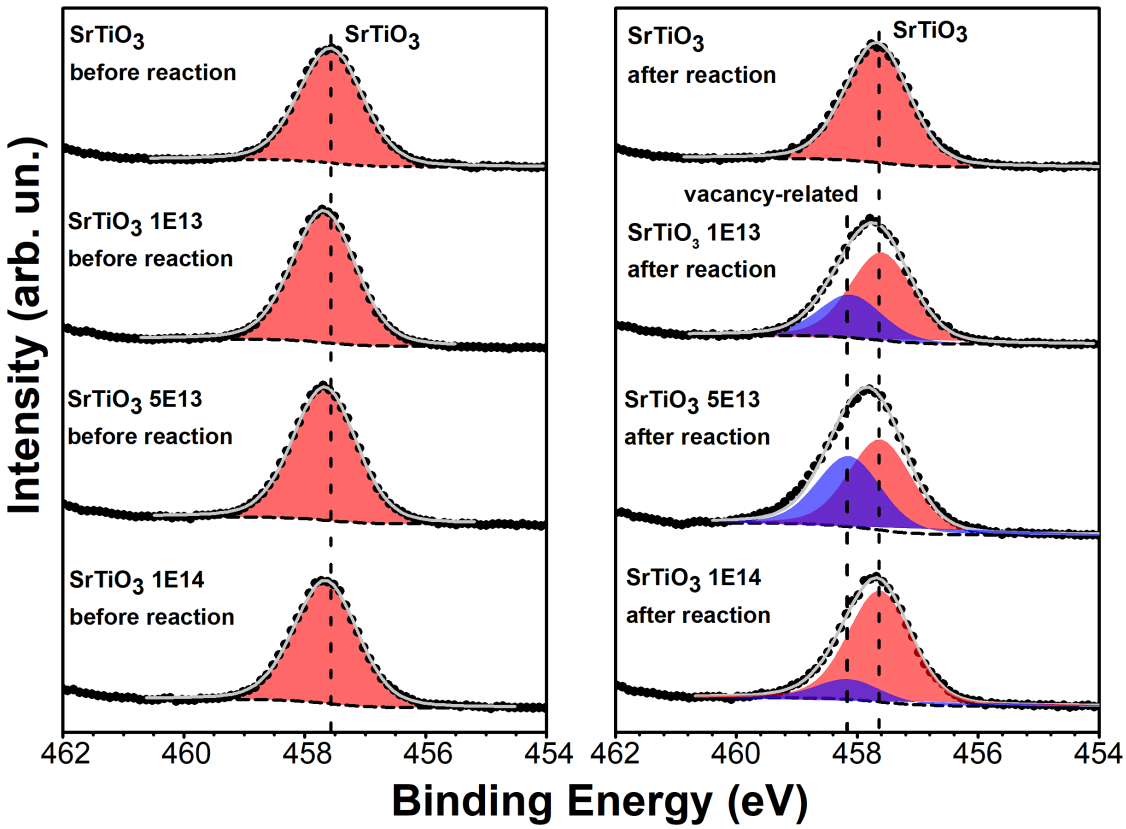

Figure 59 – Ti $2p_{3/2}$ XPS spectra before and after the photodegradation reaction for the ion irradiated $SrTiO_3$ nanoparticles.

component appears at 532.5 eV, which is assigned to C-O or C=O bonding [175]. Again, the $SrCO_3$ component intensity increases after the photodegradation reaction and the vacancy-related component overlaps with this one [8]. The component percentage of this component correlates almost linearly with the vacancy-related component in Ti 2p XPS region, as observed in Figure 61. As discussed previously, this is a further indication of the presence of the vacancy-related component at Ti 2p. The atomic vacancies are created during ion irradiation and they are not present at the surface of the nanoparticles due to the high energy of Au^{+7} ions. The XPS vacancy-related components are not observed before reaction, but the localized heating due to the photon flux could potentially induce the vacancy diffusion from the bulk to the surface, thus appearing in the XPS measurements after the photodegradation reaction. The vacancies could then be filled by, for example, OH radicals from the water molecules or even subproducts of the methylene blue molecule degradation. This would also explain why the $SrTiO_3$ sample does not present these new C-O and C=O components after the reaction, i.e., due to the lack of surface vacancies.

Since the point of zero charge of $SrTiO_3$ has been reported to have values around pH 8 [176], the surface of the nanoparticles in the present work may present OH radicals adsorbed

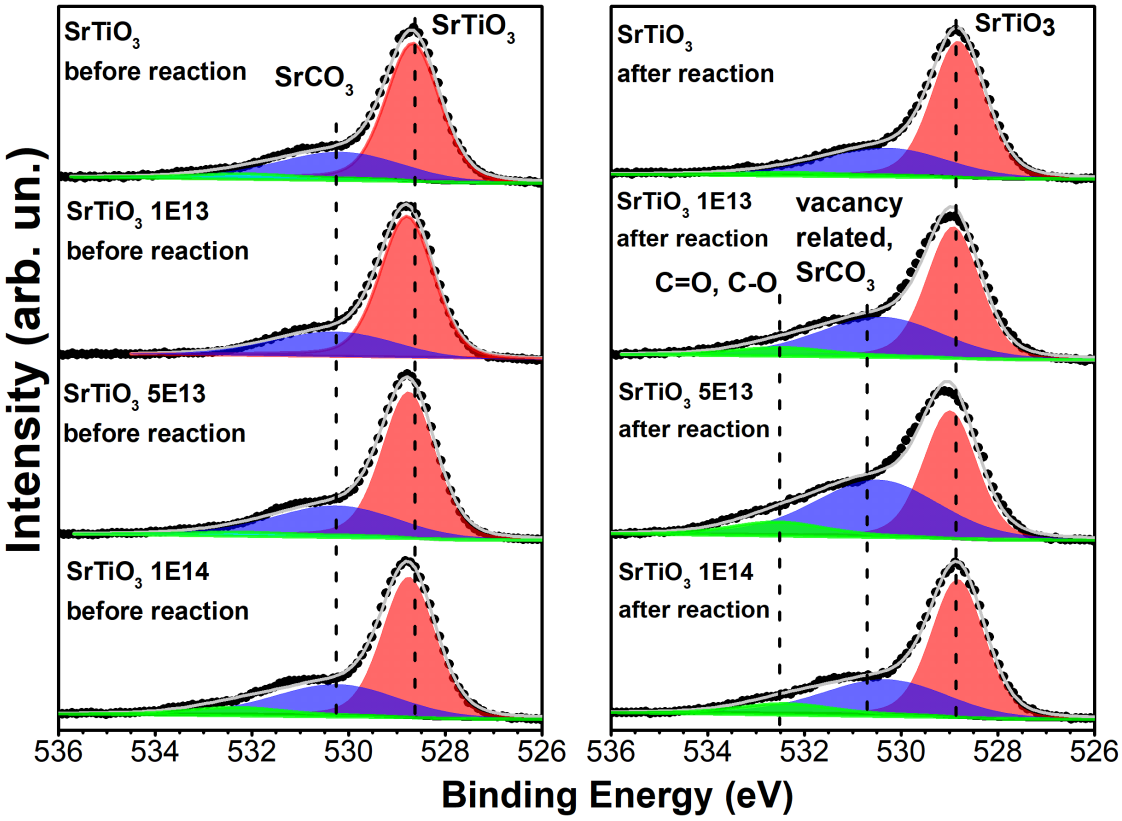

Figure 60 – O 1s XPS spectra before and after the photodegradation reaction for the ion irradiated $SrTiO_3$ nanoparticles.

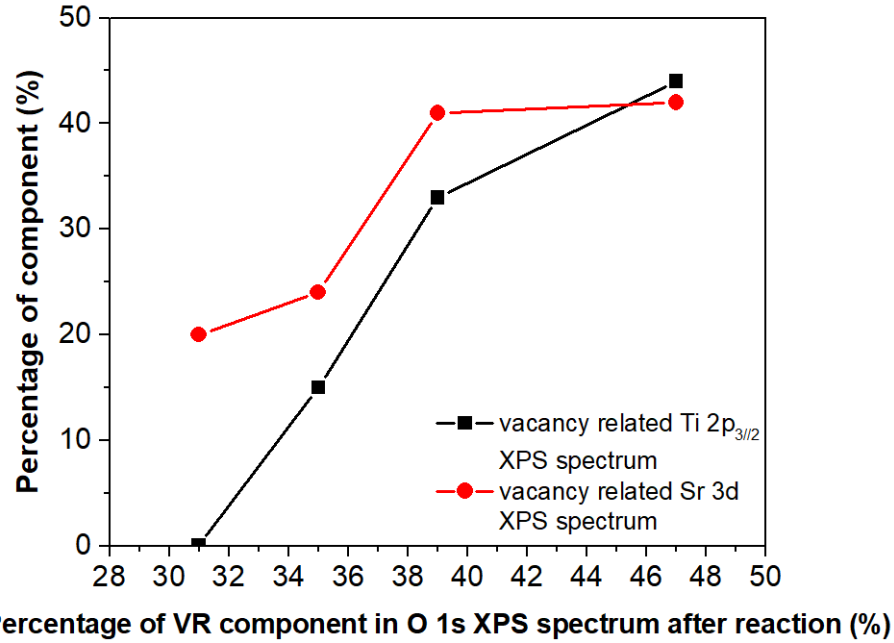

Figure 61 – Relation between vacancy-related components at different XPS regions.

while the surface itself is positively charged through the equilibrium equation (Sr,Ti)-OH + H^+ $\longleftrightarrow$ (Sr,Ti)OH_2^+. As methylene blue is a cationic dye, i.e., it decomposes into positively charged ions in the solution. Then its adsorption at the surface is reduced due to electronic repulsion, resulting in the higher probability for the vacancies to be filled by water produced radicals than to be filled by the dye.

The mechanism proposed for the improvement of the photodegradation results with ion irradiation is the filling of the vacancies at the surface by these radicals formed through either the simple dispersion of $SrTiO_3$ in water (OH radicals) and/or aided by the UV-light-induced heating (radicals produced by light absorption). The radicals produced from the dissociated water molecules after light absorption reduce/oxidize the methylene blue molecules. Figure 62 illustrates the hypothesized mechanism. A remaining question is the reason that the different fluences of the irradiation present a comparable degradation efficiency. In 48 mg of sample, there are around 5.10^{20} atoms. In a crude approximation, the percentage of atoms at the surface of 30 nm $SrTiO_3$ nanoparticles is less than 10 %. Since each ion can create at least 10^4 vacancies, then the total number of vacancies created is between 1×10^{17} and 1×10^{18}. Thus, even if the fluence is increased, not all vacancies diffuse to the surface, creating a limiting effect. Further work should corroborate both propositions.

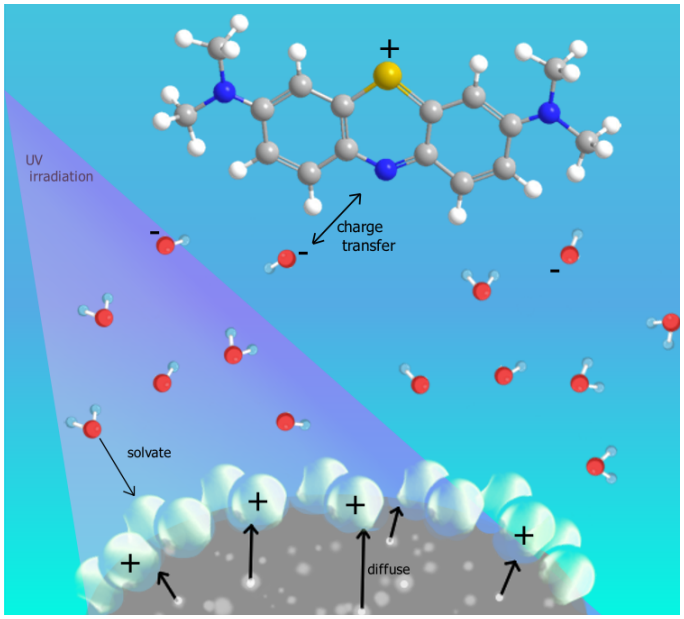

Figure 62 – Model proposed for the photodegradation of methylene blue with ion irradiated $SrTiO_3$ nanoparticles.

5 Conclusions and Perspectives

In this work, two different methods for improving the methylene blue photodegradation by $SrTiO_3$ nanoparticles were proposed. The first proposal concerns the tuning of the oxidation state of Ni nanoparticles that are supported on $SrTiO_3$. When the Ni nanoparticles present mainly a metallic component (Ni^0), as observed by XANES and EXAFS analysis, they induce a surface reconstruction of the $SrTiO_3$ nanoparticles, which was inferred by XPS analysis. This surface reconstruction of the $SrTiO_3$ nanoparticles is understood as segregated components of TiO_{2-x} and SrO_x at the first atomic layers. The increased fraction of Ni^0 is linked to an optimization of photodegradation. Nonetheless, for Ni nanoparticles mainly oxidized to NiO, it is proposed the formation of a NiO/$SrTiO_3$ heterostructure. This decreases the electron-hole pair recombination, thus increasing the reaction efficiency. In order to understand better the mechanisms of interaction with the methylene blue molecules and H_2O, DFT studies are planned for different $SrTiO_3$ surfaces. XRD measurements of the samples after the reaction will corroborate the surface reconstruction hypothesis.

Alternatively, the ion irradiation of $SrTiO_3$ induces the creation of atomic vacancies, which are beneficial for the photodegradation of the methylene blue molecule. A direct comparison with the literature is difficult, but the substantial increase in the photodegradation (around $60\ \%$ more of methylene blue degradation after three hours of reaction in comparison to the non-irradiated sample) reveals the better catalytic capabilities obtained after this procedure. There is evidence for the diffusion of vacancies to the surface of $SrTiO_3$, as observed by XPS, where new components appear at higher binding energies for the Ti $2p_{3/2}$, Sr 3d and O 1s electronic regions. These match oxygen vacancies related components of $SrTiO_3$ in previous works from the literature. The vacancies act as extra adsorption sites and recombine with radicals or molecules present in the solution. This system is currently being studied by DFT calculations, where different radicals are selected to adsorb at the surface. Raman Spectroscopy and Fourier Transform Infrared Spectroscopy measurements will help to identify which radicals are present at the surface after the reactions.

It was possible to elucidate the atomic mechanisms occurring during the photodegradation reaction. The results obtained from studying these two systems will guide and assist the development of new catalysts that can efficiently clean the effluent of industries around the world.

The lower overall expense to produce the Ni^0-rich sample in comparison to the NiO-rich and Au irradiated ones makes this sample promising for further applications.

APPENDIX A – Density Functional Theory calculations

A.1 Local Density Approximation

The Local Density Approximation takes the potential V_{xc} in equation (2.84) as the isotropic electron gas with the density $\rho(\mathbf{r})$, by expressing the energy as[125]:

$$E_{xc}^{LDA}[\rho] = \int \rho(\mathbf{r})\xi_{xc}(\rho(\mathbf{r}))d\mathbf{r} \tag{A.1}$$

where ξ_{xc} is the electron gas exchange-correlation energy and it can be further split into a sum of two components $\xi_x + \xi_c$. The form of ξ_x is the same as if evaluating in the Hartree-Fock approximation using Slater's determinant:

$$\xi_x = -\frac{3}{4}\left[\frac{3}{\pi}\rho(\mathbf{r})\right]^{1/3} \tag{A.2}$$

It must be noted that, while the LDA is one of the most simple approximations used in DFT, it is a valid configuration and presents good predictions for most solid state systems. Furthermore, if the system is spin-polarized, i.e., the spin components do not have the same electronic density, then a straightforward generalization of the LDA is the Local Spin-Density Approximation (LSDA).

A.2 Generalized Gradient Approximation

As the LDA approach can be insufficient to the study of chemical systems, a further step is to employ a Taylor expansion to the exchange-correlation energy, where LDA could be viewed as the first term [177]:

$$E_{xc}^{GEA}\left[\rho_\uparrow\rho_\downarrow\right] = \int \rho(\mathbf{r})\xi_{xc}\left(\rho_\uparrow\rho_\downarrow\right)d\mathbf{r} + \sum_\sigma\sum_{\sigma'}\int C_{xc}^{\sigma\sigma'}\left(\rho_\uparrow\rho_\downarrow\right)\frac{\nabla\rho_\sigma}{\rho_\sigma^{2/3}}\frac{\nabla\rho'_\sigma}{\rho_{\sigma'}^{2/3}} + \ldots \tag{A.3}$$

where $\rho_\uparrow$, $\rho_\downarrow$ represent both spin states. This is known as the Gradient Expansion Approximation (GEA) and can be applied where the electronic density varies slowly. But this approach can fail

due to the fact that, since exchange holes associated with the functional of this equation are not restricted to be negative for every $\mathbf{r}_i$:$\mathbf{r}_j$ pair, it can lead to unrealistic results. The solution is to truncate any part of the exchange holes that violate this restriction, resulting in the Generalized Gradient Approximation (GGA):

$$E_{xc}^{GGA}\left[\rho_{\uparrow}\rho_{\downarrow}\right] = \int f\left(\rho_{\uparrow}, \rho_{\downarrow}, \nabla\rho_{\uparrow}, \nabla\rho_{\downarrow}\right) d\mathbf{r} \tag{A.4}$$

A.3 Plane waves basis

The solutions to the Kohn-Sham equations can be expanded in a basis set $\{f_\alpha\}$ with N_b as the size of the set:

$$\psi_i(\mathbf{r}) = \sum_{\alpha}^{N_b} c_{i\alpha} f_\alpha(\mathbf{r}) \tag{A.5}$$

Then, the problem reduces to a system of linear equations, and there is the need to diagonalize the $N_b \times N_b$ matrix:

$$\sum_{\beta} H_{\alpha\beta} c_{i\beta} = \varepsilon_i c_{i\alpha} \tag{A.6}$$

These basis functions can be plane waves, gaussian functions, atomic orbitals, and hybrids. A plane wave basis has an advantage for the simplicity of making a Fourier transform:

$$\bar{f} = \sum_{\alpha}^{N-1} f_\alpha e^{-i2\pi k\alpha/N} \tag{A.7}$$

For plane waves, there is a need for the use of periodic systems, where Bloch's theorem can be called:

$$u_{\mathbf{k}} = \frac{1}{V}\sum_{\mathbf{K}} c_{\mathbf{k},\mathbf{K}} e^{i\mathbf{K}\cdot\mathbf{r}} \Longrightarrow \psi_{\mathbf{k}} = \frac{1}{V}\sum_{\mathbf{K}} c_{\mathbf{k},\mathbf{K}} e^{i(\mathbf{K}+\mathbf{k})\cdot\mathbf{r}} \tag{A.8}$$

So that the solution does not require an infinite number of expansions, the basis can be truncated at a cut-off energy:

$$\frac{\hbar^2}{2m_e}\left|\mathbf{k}+\mathbf{K}\right|^2 \leq E_{cut} \tag{A.9}$$

In practical calculations, the sum over the first Brillouin zone can be approximated by a grid with a finite number of Brillouin zone sampling points. The electronic density can be expressed Fourier transformed as well:

$$\bar{\rho}_s(\mathbf{K}) = \sum_i \sum_{\mathbf{K}'} \widetilde{\psi}_i^*(\mathbf{K}')\widetilde{\psi}_i(\mathbf{K}-\mathbf{K}') \tag{A.10}$$

If a certain operator $\langle \mathbf{r}|A|\mathbf{r}'\rangle = A(\mathbf{r},\mathbf{r}')$ is local in the form $A(\mathbf{r})\delta(\mathbf{r}-\mathbf{r}')$, than it can be expanded in the reciprocal space as:

$$\bar{A}(\mathbf{k}+\mathbf{K},\mathbf{k}+\mathbf{K}') = \int\int d\mathbf{r}d\mathbf{r}' e^{i(\mathbf{k}+\mathbf{K})\cdot\mathbf{r}} A(\mathbf{r})\delta(\mathbf{r}-\mathbf{r}')e^{-i(\mathbf{k}+\mathbf{K}')\cdot\mathbf{r}'} = \bar{A}(\mathbf{K}-\mathbf{K}') \tag{A.11}$$

Equation (A.6) can be rewritten in the basis as:

$$\sum_{\mathbf{K}'} H_{\mathbf{k}+\mathbf{K},\mathbf{k}+\mathbf{K}'} c_{i,\mathbf{k}+\mathbf{K}'} = \varepsilon_i c_{i,\mathbf{k}+\mathbf{K}} \tag{A.12}$$

And the hamiltonian matrix elements can be written as:

$$\begin{aligned} H_{\mathbf{k}+\mathbf{K},\mathbf{k}+\mathbf{K}'} &= \frac{1}{2}\left|\mathbf{k}+\mathbf{K}\right|^2 \delta_{\mathbf{K},\mathbf{K}'} + \bar{v}_{eff}(\mathbf{k}+\mathbf{K},\mathbf{k}+\mathbf{K}'), \\ \bar{v}_{eff} &= \bar{V}_c(\mathbf{K}-\mathbf{K}') + \bar{V}_{xc}(\mathbf{K}-\mathbf{K}') + \bar{V}_{e,N}(\mathbf{k}+\mathbf{K},\mathbf{k}+\mathbf{K}') \end{aligned} \tag{A.13}$$

The main issues with plane waves arise when dealing specially with the potential close to the nuclei, $V_{e,N}$, that becomes very steep. An alternative approach is to substitute these features with pseudopotentials and to use a modified basis that has these features built in them. One of these modified basis is the Projector Augmented Wave Method (PAW). The approach to this basis is to split the all-electron Kohn-Sham wavefunction into three parts:

$$\psi_i(\mathbf{r}) = \varphi_i(\mathbf{r}) + \sum_A \psi_i^A(\mathbf{r}) - \sum_A \varphi_i^A(\mathbf{r}) \tag{A.14}$$

where φ represents a pseudo wave function that, instead of ψ, can be smooth and defined close to the nucleus, and A represents a summation over the atoms on the lattice.

A.4 DFT+U

In the study of strongly correlated systems such as metal oxides and Mott insulators, standard DFT ignores the electronic repulsion of the electrons localized at the same site. In order

to take it into account, the Hubbard term, U, is added [178, 179]. An example to interpret this term is traditionally discussed in a $3d$ electron system with n $3d$ electrons per atom, where U is the energy cost for the $3d^n + 3d^n \rightarrow 3d^{n+1} + 3d^{n-1}$ electron hopping. The modification to the hamiltonian must be to add the following term [180]:

$$\hat{H}'_d = \frac{U}{2} \sum_{m,m',\sigma} (\hat{n}_{m,\sigma}\hat{n}_{m',-\sigma}) + \frac{(U-J)}{2} \sum_{m' \neq m,\sigma} (\hat{n}_{m,\sigma}\hat{n}_{m',\sigma}) \tag{A.15}$$

where $\hat{n}$ is the occupation number operator of the atomic orbital m and spin σ. The term J represents Hund's rule exchange parameter, associated with the decrease in repulsion energy when placing two electrons in orbitals with parallel spins. If the system is rotationally invariant concerning a unitary transformation of orbitals, the energy modification can be given by the terms contained in density matrix Γ^σ of d electrons:

$$E'_d = \frac{U-J}{2} \sum_{\sigma} \left[Tr\{\Gamma^\sigma\} - Tr\{\Gamma^\sigma \Gamma^\sigma\} \right], \quad \Gamma^\sigma_{p,q}(\mathbf{r},\mathbf{r}') = \psi_{p\sigma}(\mathbf{r}) n_{p\sigma} \delta_{p,q} \psi_{p\sigma}(\mathbf{r}') \tag{A.16}$$

A.5 Convergence tests

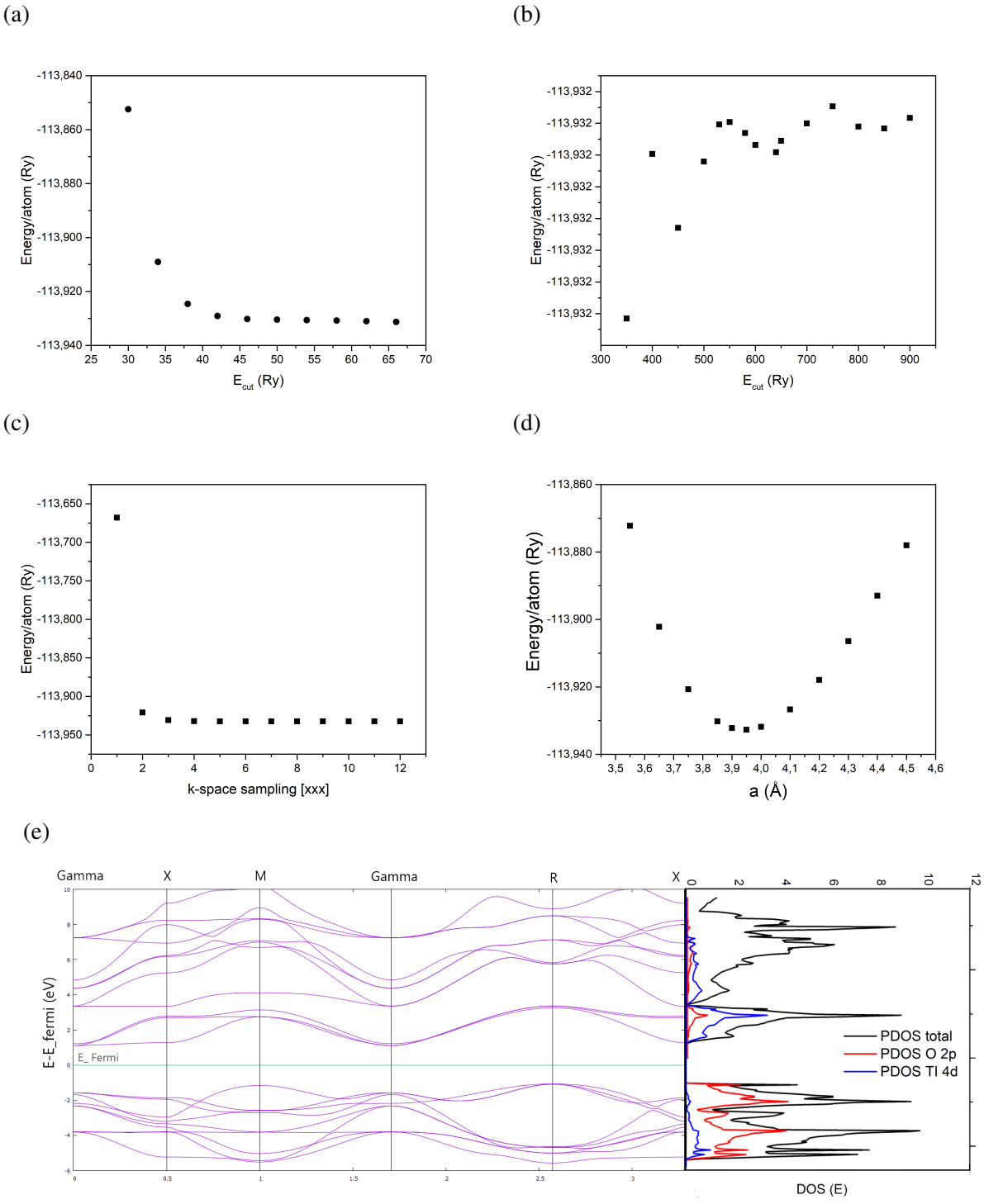

Figure 63 – Convergence of unit cell (a) wavefunctions cut-off energy, (b) density cut-off energy, (c) k-grid sampling, (d) equation of state, (e) density of states and bands plot.

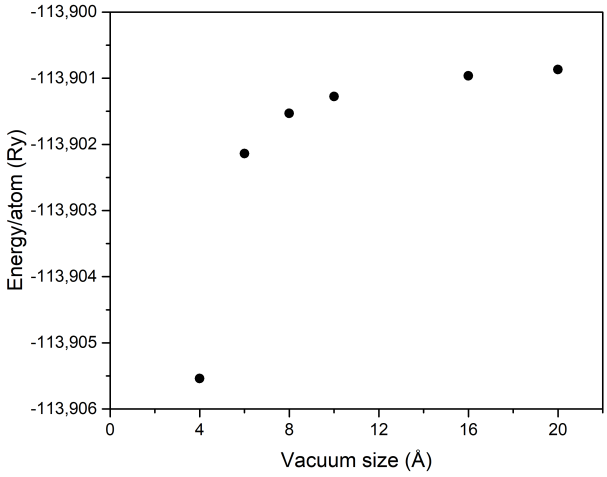

Figure 64 – Convergence of total energy of different vacuum layer's size by using a unit cell of $SrTiO_3$. Wavefunctions cut-off energy was put to 58 Ry, density cut-off energy to 650 Ry and k-space sample by a [777] grid.

(a) (b)

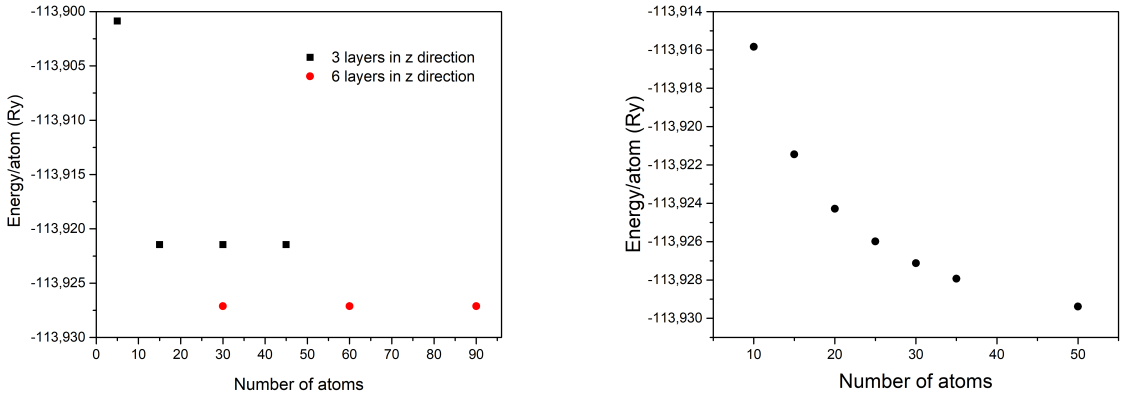

Figure 65 – Convergence of total energy for $SrTiO_3$ slab model (TiO_2 termination, 20 Å vacuum size, $[001]$ plane cut) as a function of increasing number of atoms in the (a) $\hat{x}$ and (b) $\hat{z}$ directions.

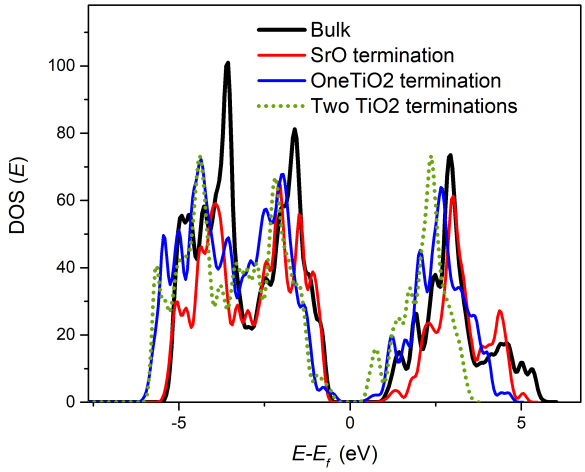

Figure 66 – Density of states comparison between different configurations of $SrTiO_3$.

(a) (b)

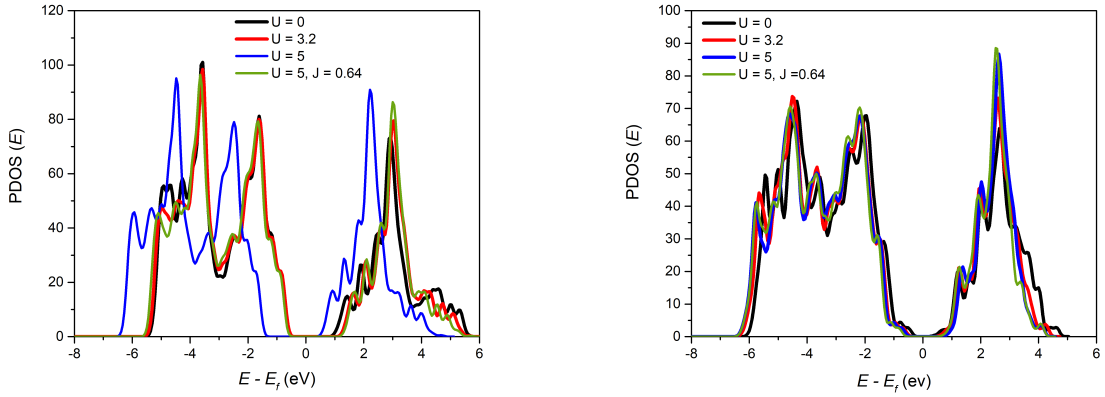

(c)

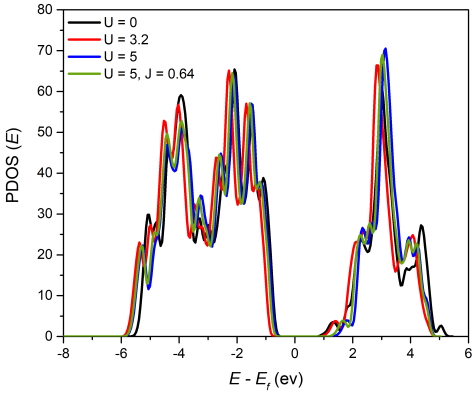

Figure 67 – Density of states of (a) bulk $SrTiO_3$ (60 atoms supercell), slab models (20 Å vacuum size, $[001]$ plane cut) with (b) TiO_2 (60 atoms) and (c) SrO (48 atoms) terminations for different values of U and J in the DFT+U implementation.

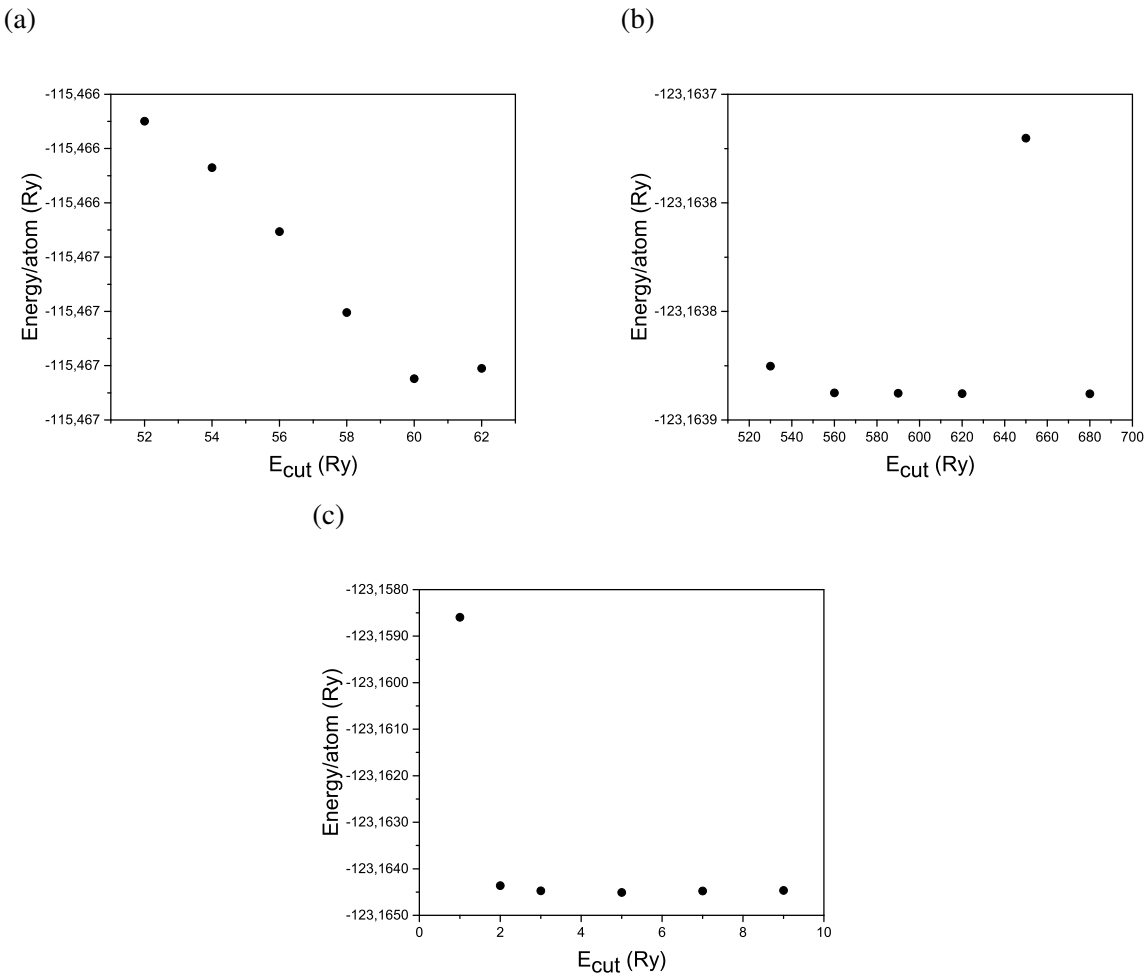

Figure 68 – Convergence tests for TiO_2 terminated $SrTiO_3$ slabs (60 atoms) with a 4 atoms Ni cluster over (a) wavefunction energy cut-off, (b) electron density energy cut-off and (c) [k k 1] reciprocal space sampling.

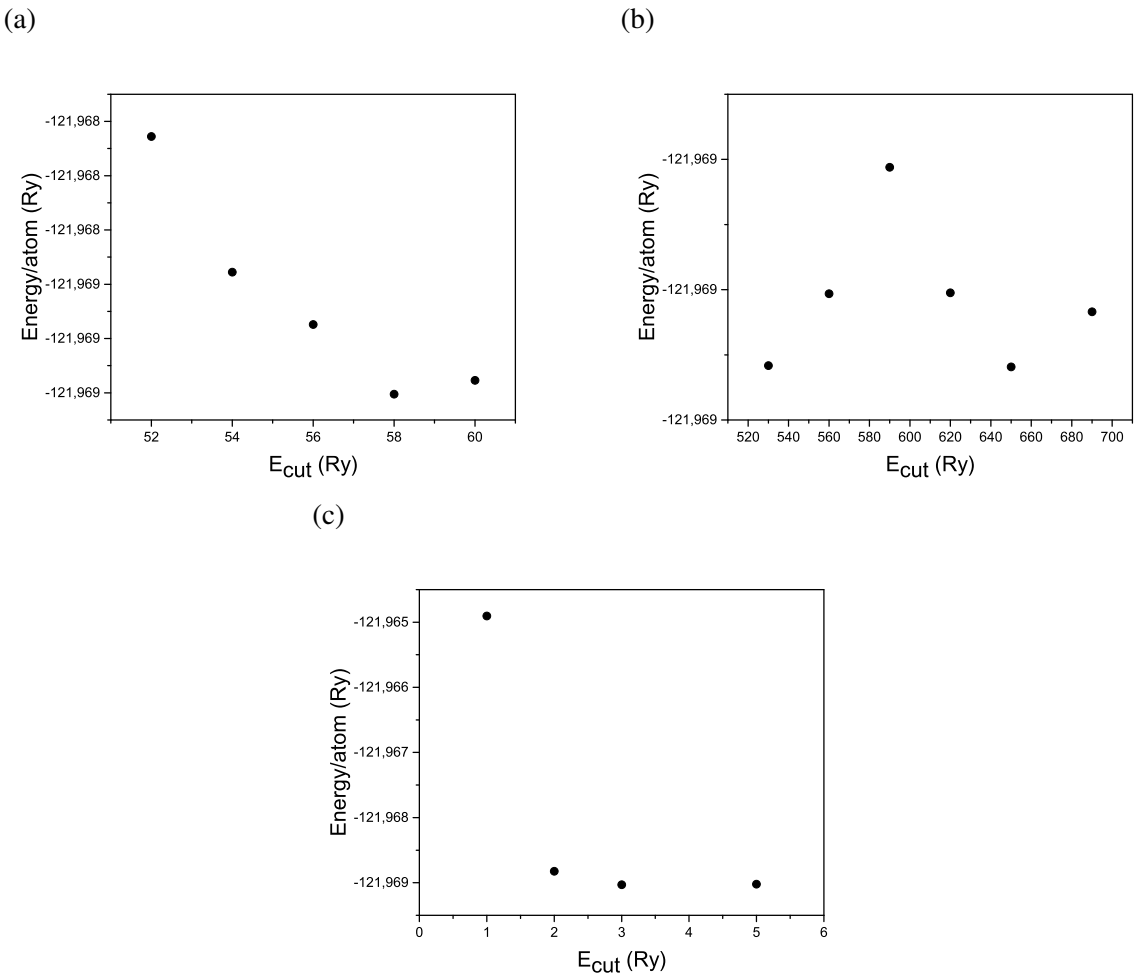

Figure 69 – Convergence tests for SrO terminated $SrTiO_3$ slabs (48 atoms) with a 4 atoms Ni cluster over (a) wavefunction energy cut-off, (b) electron density energy cut-off and (c) [k k 1] reciprocal space sampling.

Bibliography

1 VÖRÖSMARTY, C. J. et al. Global threats to human water security and river biodiversity. **nature**, Nature Publishing Group, v. 467, n. 7315, p. 555–561, 2010.

2 ZOLLINGER, H. **Color chemistry: syntheses, properties, and applications of organic dyes and pigments**. New York: John Wiley & Sons, 2003.

3 CLIFTON, I. J.; LEIKIN, J. B. Methylene blue. **American journal of therapeutics**, LWW, v. 10, n. 4, p. 289–291, 2003.

4 RAMSAY, R.; DUNFORD, C.; GILLMAN, P. Methylene blue and serotonin toxicity: inhibition of monoamine oxidase confirms a theoretical prediction. **British journal of pharmacology**, Wiley Online Library, v. 152, n. 6, p. 946–951, 2007.

5 ALBERT, M.; LESSIN, M. S.; GILCHRIST, B. F. Methylene blue: dangerous dye for neonates. **Journal of pediatric surgery**, Elsevier, v. 38, n. 8, p. 1244–1245, 2003.

6 AFROZ, K. et al. A heterojunction strategy to improve the visible light sensitive water splitting performance of photocatalytic materials. **Journal of Materials Chemistry A**, Royal Society of Chemistry, v. 6, n. 44, p. 21696–21718, 2018.

7 INSTITUTO NACIONAL DE PESQUISAS ESPACIAIS, DIVISÃO DE SATÉLITES E SISTEMAS AMBIENTAIS. **Radiação Solar e Terrestre**. 2020. Available at: <http://satelite.cptec.inpe.br/radiacao/>. Last accessed: 22 dec. 2020.

8 TAN, H. et al. Oxygen vacancy enhanced photocatalytic activity of pervoskite $SrTiO_3$. **ACS applied materials & interfaces**, ACS Publications, v. 6, n. 21, p. 19184–19190, 2014.

9 XIE, K. et al. Self-doped $SrTiO_{3-\delta}$ photocatalyst with enhanced activity for artificial photosynthesis under visible light. **Energy & Environmental Science**, Royal Society of Chemistry, v. 4, n. 10, p. 4211–4219, 2011.

10 CLEVELAND, C. J.; MORRIS, C. G. **Handbook of energy: diagrams, charts, and tables**. Boston: Elsevier, 2013. v. 1.

11 NIEMANTSVERDRIET, J. W. **Spectroscopy in catalysis: an introduction**. Weinheim: John Wiley & Sons, 2007.

12 NØRSKOV, J. K. et al. **Fundamental concepts in heterogeneous catalysis**. Hoboken: John Wiley & Sons, 2014.

13 SOMORJAI, G. A.; LI, Y. **Introduction to surface chemistry and catalysis**. New York: John Wiley & Sons, 2010.

14 ASTRUC, D. **Nanoparticles and catalysis**. Weinheim: John Wiley & Sons, 2008.

15 CREDI, A. **Photoactive Semiconductor Nanocrystal Quantum Dots: Fundamentals and Applications**. New York: Springer, 2017.

16 ANPO, M.; TAKEUCHI, M. The design and development of highly reactive titanium oxide photocatalysts operating under visible light irradiation. **Journal of catalysis**, Elsevier, v. 216, n. 1-2, p. 505–516, 2003.

17 YASEEN, D.; SCHOLZ, M. Textile dye wastewater characteristics and constituents of synthetic effluents: a critical review. **International journal of environmental science and technology**, Springer, v. 16, n. 2, p. 1193–1226, 2019.

18 KUNZ, A. et al. Novas tendências no tratamento de efluentes têxteis. **Química nova**, SciELO Brasil, v. 25, n. 1, p. 78–82, 2002.

19 AI, L. et al. Removal of methylene blue from aqueous solution with magnetite loaded multi-wall carbon nanotube: kinetic, isotherm and mechanism analysis. **Journal of hazardous materials**, Elsevier, v. 198, p. 282–290, 2011.

20 FUJISHIMA, A.; HONDA, K. Electrochemical photolysis of water at a semiconductor electrode. **Nature**, Nature Publishing Group, v. 238, n. 5358, p. 37–38, 1972.

21 KABIR, E. et al. Solar energy: Potential and future prospects. **Renewable and Sustainable Energy Reviews**, Elsevier, v. 82, p. 894–900, 2018.

22 RUEDA-MARQUEZ, J. J. et al. A critical review on application of photocatalysis for toxicity reduction of real wastewaters. **Journal of Cleaner Production**, Elsevier, p. 120694, 2020.

23 AHMED, S. N.; HAIDER, W. Heterogeneous photocatalysis and its potential applications in water and wastewater treatment: a review. **Nanotechnology**, IOP Publishing, v. 29, n. 34, p. 342001, 2018.

24 HERNÁNDEZ-RAMÍREZ, A.; MEDINA-RAMÍREZ, I. **Photocatalytic semiconductors**. New York: Springer, 2016.

25 LU, Q. et al. 2D transition-metal-dichalcogenide-nanosheet-based composites for photocatalytic and electrocatalytic hydrogen evolution reactions. **Advanced Materials**, Wiley Online Library, v. 28, n. 10, p. 1917–1933, 2016.

26 LEE, Y. Y. et al. Visible-light driven photocatalytic degradation of organic dyes over ordered mesoporous $Cd_xZn_{1-x}S$ materials. **The Journal of Physical Chemistry C**, ACS Publications, v. 121, n. 9, p. 5137–5144, 2017.

27 AJMAL, A. et al. Principles and mechanisms of photocatalytic dye degradation on TiO_2 based photocatalysts: a comparative overview. **Rsc Advances**, Royal Society of Chemistry, v. 4, n. 70, p. 37003–37026, 2014.

28 SILVA, L. F. da et al. An understanding of the photocatalytic properties and pollutant degradation mechanism of $SrTiO_3$ nanoparticles. **Photochemistry and photobiology**, v. 92, n. 3, p. 371–378, 2016.

29 LEE, S.-K.; MILLS, A.; LEPRE, A. An intelligence ink for oxygen. **Chemical communications**, Royal Society of Chemistry, n. 17, p. 1912–1913, 2004.

30 HUANG, C.-W. et al. A current perspective for photocatalysis towards the hydrogen production from biomass-derived organic substances and water. **International Journal of Hydrogen Energy**, Elsevier, v. 45, n. 36, p. 18144–18159, 2020.

31 KONG, J.-Z. et al. Photo-degradation of methylene blue using Ta-doped ZnO nanoparticle. **Journal of solid state chemistry**, Elsevier, v. 183, n. 6, p. 1359–1364, 2010.

32 BUBACZ, K. et al. Methylene blue and phenol photocatalytic degradation on nanoparticles of anatase TiO_2. **Polish Journal of Environmental Studies**, v. 19, n. 4, 2010.

33 THILL, A. S. et al. Shifting the band gap from uv to visible region in cerium oxide nanoparticles. **Applied Surface Science**, Elsevier, v. 528, p. 146860, 2020.

34 MURUGESAN, P.; MOSES, J.; ANANDHARAMAKRISHNAN, C. Photocatalytic disinfection efficiency of 2D structure graphitic carbon nitride-based nanocomposites: a review. **Journal of Materials Science**, Springer, p. 1–30, 2019.

35 YAN, T. et al. Fabrication of robust M/Ag_3PO_4 (M= Pt, Pd, Au) schottky-type heterostructures for improved visible-light photocatalysis. **RSC Advances**, Royal Society of Chemistry, v. 4, n. 70, p. 37220–37230, 2014.

36 LOW, J. et al. Heterojunction photocatalysts. **Advanced materials**, Wiley Online Library, v. 29, n. 20, p. 1601694, 2017.

37 WANG, H. et al. Semiconductor heterojunction photocatalysts: design, construction, and photocatalytic performances. **Chemical Society Reviews**, Royal Society of Chemistry, v. 43, n. 15, p. 5234–5244, 2014.

38 AKPAN, U. G.; HAMEED, B. H. Parameters affecting the photocatalytic degradation of dyes using tio2-based photocatalysts: a review. **Journal of hazardous materials**, Elsevier, v. 170, n. 2-3, p. 520–529, 2009.

39 CAO, Y. et al. Surface heterojunction between (001) and (101) facets of ultrafine anatase TiO_2 nanocrystals for highly efficient photoreduction CO_2 to CH_4. **Applied Catalysis B: Environmental**, Elsevier, v. 198, p. 378–388, 2016.

40 PANG, S. C.; CHIN, S. F.; ANDERSON, M. A. Redox equilibria of iron oxides in aqueous-based magnetite dispersions: Effect of ph and redox potential. **Journal of colloid and interface science**, Elsevier, v. 311, n. 1, p. 94–101, 2007.

41 QIAO, Q. et al. Facile in situ construction of mediator-free direct Z-scheme g-C_3N_4/CeO_2 heterojunctions with highly efficient photocatalytic activity. **Journal of Physics D: Applied Physics**, IOP Publishing, v. 51, n. 27, p. 275302, 2018.

42 MARTINS, P. M. et al. TiO_2/graphene and TiO_2/graphene oxide nanocomposites for photocatalytic applications: A computer modeling and experimental study. **Composites Part B: Engineering**, Elsevier, v. 145, p. 39–46, 2018.

43 XU, H. et al. Synthesis, characterization and photocatalytic property of AgBr/$BiPO_4$ heterojunction photocatalyst. **Dalton transactions**, Royal Society of Chemistry, v. 41, n. 12, p. 3387–3394, 2012.

44 LIU, X. et al. Synergy of adsorption and visible-light photocatalytic degradation of methylene blue by a bifunctional Z-scheme heterojunction of WO_3/g-C_3N_4. **Applied Surface Science**, Elsevier, v. 405, p. 359–371, 2017.

45 ZHENG, F. et al. Hydrothermal preparation of WO_3 nanorod array and ZnO nanosheet array composite structures on FTO substrates with enhanced photocatalytic properties. **Journal of Materials Chemistry C**, Royal Society of Chemistry, v. 3, n. 29, p. 7612–7620, 2015.

46 SOLTANI, N. et al. Enhancement of visible light photocatalytic activity of ZnS and CdS nanoparticles based on organic and inorganic coating. **Applied Surface Science**, Elsevier, v. 290, p. 440–447, 2014.

47 LIN, X. et al. Photocatalytic activities of heterojunction semiconductors Bi_2O_3/$BaTiO_3$: a strategy for the design of efficient combined photocatalysts. **The Journal of Physical Chemistry C**, ACS Publications, v. 111, n. 49, p. 18288–18293, 2007.

48 XIAO, Q. et al. Photocatalytic degradation of methylene blue over Co_3O_4/Bi_2WO_6 composite under visible light irradiation. **Catalysis Communications**, Elsevier, v. 9, n. 6, p. 1247–1253, 2008.

49 WANG, W. et al. Enhanced photoelectrochemical activity and photocatalytic water oxidation of NiO nanoparticle-decorated $SrTiO_3$ nanocube heterostructures: Interaction, interfacial charge transfer and enhanced mechanism. **Solar Energy Materials and Solar Cells**, Elsevier, v. 152, p. 1–9, 2016.

50 YANG, S. et al. Tunability of the band energetics of nanostructured $SrTiO_3$ electrodes for dye-sensitized solar cells. **The Journal of Physical Chemistry C**, ACS Publications, v. 114, n. 9, p. 4245–4249, 2010.

51 PHOON, B. L. et al. A review of synthesis and morphology of $SrTiO_3$ for energy and other applications. **International Journal of Energy Research**, Wiley Online Library, v. 43, n. 10, p. 5151–5174, 2019.

52 TOWNSEND, T. K.; BROWNING, N. D.; OSTERLOH, F. E. Nanoscale strontium titanate photocatalysts for overall water splitting. **ACS nano**, ACS Publications, v. 6, n. 8, p. 7420–7426, 2012.

53 JIA, A. et al. Synthesis and characterization of highly-active nickel and lanthanum co-doped $SrTiO_3$. **Solid state sciences**, Elsevier, v. 12, n. 7, p. 1140–1145, 2010.

54 BHALLA, A.; GUO, R.; ROY, R. The perovskite structure—a review of its role in ceramic science and technology. **Materials research innovations**, Taylor & Francis, v. 4, n. 1, p. 3–26, 2000.

55 KOK, D. J. et al. Temperature-dependent optical absorption of $SrTiO_3$. **physica status solidi (a)**, Wiley Online Library, v. 212, n. 9, p. 1880–1887, 2015.

56 MAO, Y.; ZHOU, H.; WONG, S. S. Synthesis, properties, and applications of perovskite-phase metal oxide nanostructures. **Material Matters**, v. 5, n. 2, p. 50, 2010.

57 PISKUNOV, S. et al. Bulk properties and electronic structure of $SrTiO_3$, $BaTiO_3$, $PbTiO_3$ perovskites: an Ab initio HF/DFT study. **Computational Materials Science**, Elsevier, v. 29, n. 2, p. 165–178, 2004.

58 BENTHEM, K. V.; ELSÄSSER, C.; FRENCH, R. Bulk electronic structure of $SrTiO_3$: Experiment and theory. **Journal of applied physics**, American Institute of Physics, v. 90, n. 12, p. 6156–6164, 2001.

59 EGLITIS, R.; VANDERBILT, D. First-principles calculations of atomic and electronic structure of $SrTiO_3$(001) and (011) surfaces. **Physical Review B**, APS, v. 77, n. 19, p. 195408, 2008.

60 SIVADAS, N. et al. Thickness-dependent carrier density at the surface of $SrTiO_3$(111) slabs. **Physical Review B**, APS, v. 89, n. 7, p. 075303, 2014.

61 WANG, L.-Q.; FERRIS, K.; HERMAN, G. Interactions of H_2O with $SrTiO_3$(100) surfaces. **Journal of Vacuum Science & Technology A: Vacuum, Surfaces, and Films**, American Vacuum Society, v. 20, n. 1, p. 239–244, 2002.

62 GARCIA-DIAZ, R. et al. DFT study for OH radical formation on $SrTiO_3$(001) surface and the effect of Bi. **Applied Surface Science**, Elsevier, v. 487, p. 1394–1402, 2019.

63 SHI, W.-J.; XIONG, S.-J. Ab initio study of water adsorption on TiO_2-terminated (100) surface of $SrTiO_3$ with and without Cr doping. **Surface science**, Elsevier, v. 604, n. 21-22, p. 1987–1995, 2010.

64 BROOKES, N.; THORNTON, G.; QUINN, F. $SrTiO_3$ (100) step sites as catalytic centers for H_2O dissociation. **Solid state communications**, Elsevier, v. 64, n. 3, p. 383–386, 1987.

65 WANG, Z. et al. Water adsorption at the tetrahedral titania surface layer of $SrTiO_3$ (110)-(4$\times$ 1). **The Journal of Physical Chemistry C**, ACS Publications, v. 117, n. 49, p. 26060–26069, 2013.

66 HSIEH, P.-L. et al. Shape-tunable $SrTiO_3$ crystals revealing facet-dependent optical and photocatalytic properties. **The Journal of Physical Chemistry C**, ACS Publications, v. 123, n. 22, p. 13664–13671, 2019.

67 CHEN, L. et al. Photocatalytic activity of Zr:$SrTiO_3$ under UV illumination. **Journal of Crystal Growth**, v. 311, n. 3, p. 735–737, 2009.

68 GHAFFARI, M. et al. Synthesis and visible light photocatalytic properties of $SrTi_{1-x}Fe_xO_{3-\delta}$ powder for indoor decontamination. **Powder technology**, v. 225, p. 221–226, 2012.

69 LI, F. et al. Theoretical and experimental study of La/Ni co-doped $SrTiO_3$ photocatalyst. **Materials Science and Engineering: B**, v. 172, n. 2, p. 136–141, 2010.

70 JIA, A. et al. Synthesis and characterization of highly-active nickel and lanthanum co-doped $SrTiO_3$. **Solid State Sciences**, v. 12, n. 7, p. 1140–1145, 2010.

71 OLAGUNJU, M. O. et al. Size-controlled $SrTiO_3$ nanoparticles photodecorated with Pd cocatalysts for photocatalytic organic dye degradation. **ACS Applied Nano Materials**, ACS Publications, v. 3, n. 5, p. 4904–4912, 2020.

72 FERREIRA, M. A. et al. Fabrication of $SrTiO_3$/g-C_3N_4 heterostructures for visible light-induced photocatalysis. **Materials Science in Semiconductor Processing**, Elsevier, v. 108, p. 104887, 2020.

73 BANTAWAL, H.; SHENOY, U. S.; BHAT, D. K. Vanadium-doped $SrTiO_3$ nanocubes: Insight into role of vanadium in improving the photocatalytic activity. **Applied Surface Science**, Elsevier, v. 513, p. 145858, 2020.

74 YANAGIDA, S. et al. Preparation and photocatalytic properties of rutile TiO_2 with a unique morphology and $SrTiO_3$-TiO_2 composites obtained by acid treatment of $SrTiO_3$. **Materials Research Bulletin**, Elsevier, v. 125, p. 110762, 2020.

75 DOMEN, K.; KUDO, A.; ONISHI, T. Mechanism of photocatalytic decomposition of water into H_2 and O_2 over NiO/$SrTiO_3$. **Journal of Catalysis**, Elsevier, v. 102, n. 1, p. 92–98, 1986.

76 GERHOLD, S. et al. Nickel-oxide-modified $SrTiO_3(110)$-(4×1) surfaces and their interaction with water. **The Journal of Physical Chemistry C**, ACS Publications, v. 119, n. 35, p. 20481–20487, 2015.

77 TOWNSEND, T. K.; BROWNING, N. D.; OSTERLOH, F. E. Overall photocatalytic water splitting with NiO_x-$SrTiO_3$ - a revised mechanism. **Energy & Environmental Science**, Royal Society of Chemistry, v. 5, n. 11, p. 9543–9550, 2012.

78 ZHANG, K. H. et al. Electronic structure and band alignment at the NiO and $SrTiO_3$ p-n heterojunctions. **ACS applied materials & interfaces**, ACS Publications, v. 9, n. 31, p. 26549–26555, 2017.

79 WANG, M. et al. Theoretical insights into interfacial and electronic structures of NiO_x/$SrTiO_3$ photocatalyst for overall water splitting. **Journal of energy chemistry**, Elsevier, v. 33, p. 138–148, 2019.

80 FO, Y. et al. Origin of highly efficient photocatalyst NiO/$SrTiO_3$ for overall water splitting: Insights from density functional theory calculations. **Journal of Solid State Chemistry**, Elsevier, v. 292, p. 121683, 2020.

81 LEE, B. et al. Oxygen vacancy clustering and electron localization in oxygen-deficient $SrTiO_3$: LDA+ U study. **Physical review letters**, APS, v. 98, n. 11, p. 115503, 2007.

82 MITRA, C. et al. Electronic structure of oxygen vacancies in $SrTiO_3$ and $LaAlO_3$. **Physical Review B**, APS, v. 86, n. 15, p. 155105, 2012.

83 KUMAR, V. et al. Enhancement in photocatalytic activity of $SrTiO_3$ by tailoring particle size and defects. **physica status solidi (a)**, Wiley Online Library, v. 216, n. 18, p. 1900294, 2019.

84 SUN, T.; LU, M. Modification of $SrTiO_3$ surface by nitrogen ion bombardment for enhanced photocatalysis. **Applied surface science**, Elsevier, v. 274, p. 176–180, 2013.

85 CULLITY, B.; STOCK, S. **Elements of X-Ray Diffraction**. Third. Harlow: Pearson Education Limited, 2014. ISBN 978-1-269-37450-7.

86 HENDEE, W. R.; RITENOUR, E. R. **Medical imaging physics**. New York: John Wiley & Sons, 2003.

87 JAESCHKE, E. J. et al. **Synchrotron Light Sources and Free-Electron Lasers: Accelerator Physics, Instrumentation and Science Applications**. 1. ed. Cham: Springer International Publishing, 2016. ISBN 978-3-319-14393-4.

88 WILLMOTT, P. **An Introduction to Synchrotron Radiation: Techniques and Applications**. 2nd. ed. Hoboken: Wiley, 2019.

89 EBERHARDT, W. Synchrotron radiation: A continuing revolution in X-ray science—diffraction limited storage rings and beyond. **Journal of Electron Spectroscopy and Related Phenomena**, Elsevier, v. 200, p. 31–39, 2015.

90 PRADO, G. et al. Synchrotron radiation in palaeontological investigations: Examples from brazilian fossils and its potential to south american palaeontology. **Journal of South American Earth Sciences**, Elsevier, p. 102973, 2020.

91 GENG, J.; JEFFERSON, D. A.; JOHNSON, B. F. The unusual nanostructure of nickel–boron catalyst. **Chemical communications**, Royal Society of Chemistry, n. 9, p. 969–971, 2007.

92 WILL, G. **Powder diffraction: The Rietveld method and the two stage method to determine and refine crystal structures from powder diffraction data**. Berlin: Springer Science & Business Media, 2006.

93 FINGER, L.; COX, D.; JEPHCOAT, A. A correction for powder diffraction peak asymmetry due to axial divergence. **Journal of applied Crystallography**, International Union of Crystallography, v. 27, n. 6, p. 892–900, 1994.

94 KRATKY, O.; GLATTER, O. Book. **Small angle X-ray scattering**. New York: Academic Press London, 1982.

95 BOLDON, L.; LALIBERTE, F.; LIU, L. Review of the fundamental theories behind small angle X-ray scattering, molecular dynamics simulations, and relevant integrated application. **Nano reviews**, v. 6, n. 1, p. 25661–1–25661–21, 2015.

96 SCHNABLEGGER, H.; SINGH, Y. The SAXS guide: getting acquainted with the principles. **Austria: Anton Paar GmbH**, p. 1–124, 2011.

97 GUINIER, A.; FOURNET, G. **Small-angle scattering of X-rays**. New York: Wiley, 1955.

98 BRESSLER, I.; KOHLBRECHER, J.; THÜNEMANN, A. F. SASfit: a tool for small-angle scattering data analysis using a library of analytical expressions. **Journal of applied crystallography**, v. 48, n. 5, p. 1587–1598, 2015.

99 ZUO, J. M.; SPENCE, J. C. Advanced transmission electron microscopy. **Advanced Transmission Electron Microscopy**, Springer Science+ Business Media, New York, 2017.

100 BRUSLIND, L. General microbiology. Oregon State University, 2020.

101 KUMAR, C. S. **UV-VIS and photoluminescence spectroscopy for nanomaterials characterization**. [S.l.]: Springer, 2013.

102 WATTS, J. F.; WOLSTENHOLME, J. An introduction to surface analysis by XPS and AES. Wiley Online Library, 2003.

103 HAAR, D. ter. **The Old Quantum Theory**. 1st edition. ed. London: Pergamon Press, 1967. ISBN 978-0-08-012102-4.

104 SEAH, M. P.; DENCH, W. Quantitative electron spectroscopy of surfaces: A standard data base for electron inelastic mean free paths in solids. **Surface and interface analysis**, Wiley Online Library, v. 1, n. 1, p. 2–11, 1979.

105 BRUNDLE, C. R.; BAKER, A. D. **Electron spectroscopy: Theory, techniques and applications**. New York: Academic Press, 1977. v. 1.

106 GROOT, F. D.; KOTANI, A. **Core level spectroscopy of solids**. Boca Raton: CRC press, 2008.

107 JENKINS, R. **Quantitative X-ray spectrometry**. New York: CRC Press, 1995.

108 OGLETREE, D. F. et al. A differentially pumped electrostatic lens system for photoemission studies in the millibar range. **Review of Scientific Instruments**, American Institute of Physics, v. 73, n. 11, p. 3872–3877, 2002.

109 CALVIN, S. **XAFS for Everyone**. Boca Raton: CRC press, 2013.

110 BUNKER, G. **Introduction to XAFS: A Practical Guide to X-ray Absorption Fine Structure Spectroscopy**. New York: Cambridge University Press, 2010.

111 ANKUDINOV, A. et al. Real-space multiple-scattering calculation and interpretation of X-ray absorption near-edge structure. **Physical Review B**, APS, v. 58, n. 12, p. 7565, 1998.

112 REHR, J. J. et al. Ab initio theory and calculations of X-ray spectra. **Comptes Rendus Physique**, Elsevier, v. 10, n. 6, p. 548–559, 2009.

113 RAVEL, B. A practical introduction to multiple scattering theory. **Journal of Alloys and compounds**, Elsevier, v. 401, n. 1-2, p. 118–126, 2005.

114 LLOYD, P.; SMITH, P. Multiple scattering theory in condensed materials. **Advances in Physics**, Taylor & Francis, v. 21, n. 89, p. 69–142, 1972.

115 SEBILLEAU, D.; HATADA, K.; EBERT, H. **Multiple Scattering Theory for Spectroscopies**. 1st ed.. ed. Cham: Springer International Publishing, 2018. (Springer Proceedings in Physics 204). ISBN 978-3-319-73810-9.

116 LEE, P.; PENDRY, J. Theory of the extended X-ray absorption fine structure. **Physical Review B**, APS, v. 11, n. 8, p. 2795, 1975.

117 NEWVILLE, M. Fundamentals of XAFS. **Reviews in Mineralogy and Geochemistry**, GeoScienceWorld, v. 78, n. 1, p. 33–74, 2014.

118 HAYES, T.; BOYCE, J. Extended X-ray absorption fine structure spectroscopy. In: **Solid State Physics**. New York: Elsevier, 1983. v. 37, p. 173–351.

119 VILA, F. D. et al. Theoretical X-ray absorption Debye-Waller factors. **Physical Review B**, APS, v. 76, n. 1, p. 014301, 2007.

120 NEWVILLE, M. IFEFFIT: interactive XAFS analysis and feff fitting. **Journal of synchrotron radiation**, International Union of Crystallography, v. 8, n. 2, p. 322–324, 2001.

121 ZIEGLER, J.; MANOYAN, J. The stopping of ions in compounds. **Nuclear Instruments and Methods in Physics Research Section B: Beam Interactions with Materials and Atoms**, Elsevier, v. 35, n. 3-4, p. 215–228, 1988.

122 SIGMUND, P. **Stopping of heavy ions: a theoretical approach**. Berlin: Springer Science & Business Media, 2004. v. 204.

123 ZIEGLER, J. F.; ZIEGLER, M. D.; BIERSACK, J. P. SRIM–The Stopping and Range of Ions in Matter (2010). **Nuclear Instruments and Methods in Physics Research Section B: Beam Interactions with Materials and Atoms**, Elsevier, v. 268, n. 11-12, p. 1818–1823, 2010.

124 PARR ROBERT G.;WEITAO, R. G. Y. **Density-Functional Theory of Atoms and Molecules**. New York: Oxford University Press, 1995. ISBN 0-19-509276-7.

125 KOCH, W.; HOLTHAUSEN, M. C. **A Chemist's Guide to Density Functional Theory**. 2. ed. Weinheim: Wiley-VCH, 2001. ISBN 9783527303724.

126 SANTEN, R. A. V.; SAUTET, P. **Computational methods in catalysis and materials science: an introduction for scientists and engineers**. Weinheim: John Wiley & Sons, 2015.

127 HOHENBERG, P.; KOHN, W. Inhomogeneous electron gas. **Physical review**, APS, v. 136, n. 3B, p. B864, 1964.

128 SHOLL, D.; STECKEL, J. A. **Density functional theory: a practical introduction**. New Jersey: John Wiley & Sons, 2011.

129 KOHN, W.; SHAM, L. J. Self-consistent equations including exchange and correlation effects. **Physical review**, APS, v. 140, n. 4A, p. A1133, 1965.

130 GÖS, W. **Hole Trapping and the Negative Bias Temperature Instability**. Dissertation — Technischen Universität Wien Fakultät für Elektrotechnik und Informationstechnik, Österreich, 2011.

131 MATTE, L. P. et al. Influence of the CeO_2 support on the reduction properties of Cu/CeO_2 and Ni/CeO_2 nanoparticles. **The Journal of Physical Chemistry C**, v. 119, n. 47, p. 26459–26470, 2015.

132 RODRÍGUEZ-CARVAJAL, J. Fullprof. **CEA/Saclay, France**, 2001.

133 DAVID, G.; PÉREZ, J. Combined sampler robot and high-performance liquid chromatography: a fully automated system for biological small-angle X-ray scattering experiments at the synchrotron soleil swing beamline. **Journal of applied crystallography**, International Union of Crystallography, v. 42, n. 5, p. 892–900, 2009.

134 SCHNEIDER, C. A.; RASBAND, W. S.; ELICEIRI, K. W. NIH Image to ImageJ: 25 years of image analysis. **Nature methods**, Nature Publishing Group, v. 9, n. 7, p. 671–675, 2012.

135 FIGUEROA, S. et al. Upgrades to the XAFS2 beamline control system and to the endstation at the LNLS. v. 712, n. 1, p. 012022, 2016.

136 CEZAR, J. C. et al. Energy-dispersive X-ray absorption spectroscopy at LNLS: investigation on strongly correlated metal oxides. **Journal of synchrotron radiation**, International Union of Crystallography, v. 17, n. 1, p. 93–102, 2010.

137 RAVEL, B.; NEWVILLE, M. Athena, artemis, hephaestus: data analysis for X-ray absorption spectroscopy using ifeffit. **Journal of synchrotron radiation**, International Union of Crystallography, v. 12, n. 4, p. 537–541, 2005.

138 KONINGSBERGER, D.; PRINS, R. **X-ray absorption: principles, applications, techniques of EXAFS, SEXAFS, and XANES**. New York: John Wiley & Sons, 1988.

139 GIROTTO, G. Z.; BERNARDI, F. **Aplicação de nanopartículas de Ni/$SrTiO_3$ na reação de fotodegradação do azul de metileno**. 2019. Monograph (B. Sc. in Physics), UFRGS (Universidade Federal do Rio Grande do Sul), Porto Alegre, Brazil.

140 ABBATE, M. et al. The soft X-ray spectroscopy beamline at the LNLS: technical description and commissioning results. **Journal of Synchrotron Radiation**, International Union of Crystallography, v. 6, n. 5, p. 964–972, 1999.

141 GIANNOZZI, P. et al. Quantum ESPRESSO: a modular and open-source software project for quantum simulations of materials. **Journal of physics: Condensed matter**, IOP Publishing, v. 21, n. 39, p. 395502, 2009.

142 CORSO, A. D. Pseudopotentials periodic table: From H to Pu. **Computational Materials Science**, Elsevier, v. 95, p. 337–350, 2014.

143 KINACI, A.; SEVIK, C.; ÇAĞIN, T. Electronic transport properties of $SrTiO_3$ and its alloys: $Sr_{1-x}La_xTiO_3$ and $SrTi_{1-x}M_xO_3$ (M= Nb, Ta). **Physical Review B**, APS, v. 82, n. 15, p. 155114, 2010.

144 MAGLIA, F.; SPINOLO, G.; ANSELMI-TAMBURINI, U. Mechanism of low temperature decomposition of NiO single crystals. **Solid state sciences**, Elsevier, v. 11, n. 9, p. 1686–1691, 2009.

145 SINGHAL, G.; RABINOWITCH, E. Changes in the absorption spectrum of methylene blue with pH. **The journal of physical chemistry**, ACS Publications, v. 71, n. 10, p. 3347–3349, 1967.

146 HAN, K. et al. Transient behavior of Ni@NiO_x functionalized $SrTiO_3$ in overall water splitting. **ACS catalysis**, ACS Publications, v. 7, n. 3, p. 1610–1614, 2017.

147 BIESINGER, M. C. et al. X-ray photoelectron spectroscopic chemical state quantification of mixed nickel metal, oxide and hydroxide systems. **Surface and Interface Analysis**, Wiley Online Library, v. 41, n. 4, p. 324–332, 2009.

148 MANSOUR, A. Characterization of NiO by XPS. **Surface Science Spectra**, American Vacuum Society, v. 3, n. 3, p. 231–238, 1994.

149 MANSOUR, A.; MELENDRES, C. Characterization of α-Ni(OH) $_2$ by XPS. **Surface Science Spectra**, American Vacuum Society, v. 3, n. 3, p. 255–262, 1994.

150 MANSOUR, A.; MELENDRES, C. Characterization of slightly hydrated $Ni(OH)_2$ by XPS. **Surface Science Spectra**, American Vacuum Society, v. 3, n. 3, p. 247–254, 1994.

151 TOLMAN, C. et al. Electron spectroscopy for chemical analysis of nickel compounds. **Inorganic Chemistry**, ACS Publications, v. 12, n. 12, p. 2770–2778, 1973.

152 MILLER, A.; SIMMONS, G. Nickel by XPS. **Surface Science Spectra**, American Vacuum Society, v. 1, n. 3, p. 312–317, 1992.

153 HERNANDEZ, N. et al. Surface behavior of nickel powders in aqueous suspensions. **The Journal of Physical Chemistry B**, ACS Publications, v. 109, n. 10, p. 4470–4474, 2005.

154 MANSOUR, A.; MELENDRES, C. Characterization of electrochemically prepared γ-NiOOH by XPS. **Surface Science Spectra**, American Vacuum Society, v. 3, n. 3, p. 271–278, 1994.

155 CAI, Q. et al. A high-performance silicon photoanode enabled by oxygen vacancy modulation on NiOOH electrocatalyst for water oxidation. **Nanoscale**, Royal Society of Chemistry, v. 12, n. 14, p. 7550–7556, 2020.

156 HUANG, L.-F. et al. Improved electrochemical phase diagrams from theory and experiment: the Ni–water system and its complex compounds. **The Journal of Physical Chemistry C**, ACS Publications, v. 121, n. 18, p. 9782–9789, 2017.

157 VASQUEZ, R. X-ray photoelectron spectroscopy study of Sr and Ba compounds. **Journal of Electron Spectroscopy and Related Phenomena**, Elsevier, v. 56, n. 3, p. 217–240, 1991.

158 VASQUEZ, R. P. $SrTiO_3$ by XPS. **Surface Science Spectra**, American Vacuum Society, v. 1, n. 1, p. 129–135, 1992.

159 DUPIN, J.-C. et al. Systematic XPS studies of metal oxides, hydroxides and peroxides. **Physical Chemistry Chemical Physics**, Royal Society of Chemistry, v. 2, n. 6, p. 1319–1324, 2000.

160 L'VOV, B. V. Mechanism and kinetics of thermal decomposition of carbonates. **Thermochimica acta**, Elsevier, v. 386, n. 1, p. 1–16, 2002.

161 FOO, G. S.; HOOD, Z. D.; WU, Z. Shape effect undermined by surface reconstruction: ethanol dehydrogenation over shape-controlled $SrTiO_3$ nanocrystals. **ACS Catalysis**, ACS Publications, v. 8, n. 1, p. 555–565, 2018.

162 POLO-GARZON, F. et al. Controlling reaction selectivity through the surface termination of perovskite catalysts. **Angewandte Chemie**, Wiley Online Library, v. 129, n. 33, p. 9952–9956, 2017.

163 CONNELL, J. et al. Preparation of atomically flat $SrTiO_3$ surfaces using a deionized-water leaching and thermal annealing procedure. **Applied Physics Letters**, American Institute of Physics, v. 101, n. 25, p. 251607, 2012.

164 HEIDE, P. Van der et al. X-ray photoelectron spectroscopic and ion scattering study of the $SrTiO_3$(001) surface. **Surface science**, Elsevier, v. 473, n. 1-2, p. 59–70, 2001.

165 OKU, M.; WAGATSUMA, K.; KOHIKI, S. Ti 2p and Ti 3p X-ray photoelectron spectra for TiO_2, $SrTiO_3$ and $BaTiO_3$. **Physical Chemistry Chemical Physics**, The Royal Society of Chemistry, v. 1, n. 23, p. 5327–5331, 1999.

166 CHASHECHNIKOVA, I. et al. Strong metal-carrier interaction in cobalt-and nickel-titanium dioxide co-hydrogenation catalysts. **Theoretical and Experimental Chemistry**, Springer, v. 28, n. 3, p. 176–178, 1993.

167 COOK, S. et al. The vacancy-induced electronic structure of the $SrTiO_{3-\delta}$ surface. **Advanced Electronic Materials**, Wiley Online Library, v. 5, n. 1, p. 1800460, 2019.

168 CHUNG, M. J. et al. Quantitative analysis of the incorporation behaviors of Sr and Ti atoms during the atomic layer deposition of $SrTiO_3$ thin films. **ACS applied materials & interfaces**, ACS Publications, v. 10, n. 10, p. 8836–8844, 2018.

169 GONZÁLEZ-ELIPE, A. et al. Compositional changes induced by 3.5 keV Ar^+ ion bombardment in Ni-Ti oxide systems: A comparative study. **Surface Science**, Elsevier, v. 220, n. 2-3, p. 368–380, 1989.

170 LUO, C. et al. Photocatalytic CO_2 reduction over $SrTiO_3$: Correlation between surface structure and activity. **Applied Surface Science**, Elsevier, v. 447, p. 627–635, 2018.

171 AAS, N.; PRINGLE, T. J.; BOWKER, M. Adsorption and decomposition of methanol on TiO_2, $SrTiO_3$ and SrO. **Journal of the Chemical Society, Faraday Transactions**, The Royal Society of Chemistry, v. 90, n. 7, p. 1015–1022, 1994.

172 MEA, G. B. D. et al. Tuning the oxygen vacancy population of cerium oxide (CeO_{2-x}, 0< x< 0.5) nanoparticles. **Applied Surface Science**, Elsevier, v. 422, p. 1102–1112, 2017.

173 LI, C.-Q. et al. Oxygen vacancy engineered $SrTiO_3$ nanofibers for enhanced photocatalytic H_2 production. **Journal of Materials Chemistry A**, Royal Society of Chemistry, v. 7, n. 30, p. 17974–17980, 2019.

174 PENG, S. et al. Low temperature and controllable formation of oxygen vacancy $SrTiO_{3-x}$ by loading Pt for enhanced photocatalytic hydrogen evolution. **Energy Technology**, Wiley Online Library, v. 6, n. 11, p. 2166–2171, 2018.

175 ZHANG, Y.; SAVARA, A.; MULLINS, D. R. Ambient-pressure XPS studies of reactions of alcohols on $SrTiO_3$(100). **The Journal of Physical Chemistry C**, ACS Publications, v. 121, n. 42, p. 23436–23445, 2017.

176 GAO, H.; YANG, H.; WANG, S. Hydrothermal synthesis, growth mechanism, optical properties and photocatalytic activity of cubic $SrTiO_3$ particles for the degradation of cationic and anionic dyes. **Optik**, Elsevier, v. 175, p. 237–249, 2018.

177 PERDEW, J. P.; BURKE, K.; ERNZERHOF, M. Generalized gradient approximation made simple. **Physical review letters**, APS, v. 77, n. 18, p. 3865, 1996.

178 ANISIMOV, V. I.; ZAANEN, J.; ANDERSEN, O. K. Band theory and mott insulators: Hubbard U instead of Stoner I. **Physical Review B**, APS, v. 44, n. 3, p. 943, 1991.

179 ANISIMOV, V.; GUNNARSSON, O. Density-functional calculation of effective coulomb interactions in metals. **Physical Review B**, APS, v. 43, n. 10, p. 7570, 1991.

180 DUDAREV, S. et al. Electron-energy-loss spectra and the structural stability of nickel oxide: An LSDA+U study. **Physical Review B**, APS, v. 57, n. 3, p. 1505, 1998.